ISSN 2949-561X (Online)

APPLIED PHYSICS

5` 25

Applied Physics
2025, No. 5

The journal was founded in 1994

The scientific and technical peer-reviewed journal is intended for the publication of articles on the latest achievements in the field of physics with prospects for advancements (technical and scientific) applications.

The periodicity is 6 issues per year.

Founder and publisher

Research, Development and Production Center ORION, Joint-Stock Company – Russian Federation State Science Center
(RD&P Center ORION, JSC)
9, Kosinskaya st., Moscow, 111538 Russia

The journal is included into the List of peer-reviewed science press of the State Commission for Academic Degrees and Titles of Russian Federation. The Journal is included in Scientific Electronic Library eLIBRARY.RU, SCOPUS, Chemical Abstracts (CA), Russian Science Citation Index (RSCI), Directory of Open Access Journals (DOAJ), Directory of Open Access Scholarly Resources (ROAD), Google Scholar.

Editor-in-Chief

Editorial office address

9, Kosinskaya st., Moscow, 111538, Russia,
RD&P Center ORION, JSC.
Phone: 8(499) 374-82-40
E-mail: advance@orion-ir.ru
Internet: applphys.orion-ir.ru

The registration PI No. FS 77-73641
was issued in September 21, 2018
by the Federal Service for Supervision
of Communications, Information Technology, and Mass Media of Russia

Editorial Board

APPLIED PHYSICS [in Russian]

THE SCIENTIFIC AND TECHNICAL JOURNAL

2025, No. 5 | Founded in 1994 | Moscow

C O N T E N T S

GENERAL PHYSICS

PHOTOELECTRONICS

PLASMA PHYSICS AND PLASMA METHODS

PHYSICAL SCIENCE OF MATERIALS

PHYSICAL EQUIPMENT AND ITS ELEMENTS

PERSONALI

INFORMATION

GENERAL PHYSICS

UDC 614.485; 614.487 PACS: 87.50; 92.60.Sz
EDN: FUXTBY

Application of UV radiation 222 nm of excimer KrCl lamps for disinfection

L. M. Vasilyak[1,*], N. N. Kudryavtsev[2], S. V. Kostyuchenko[3], D. O. Sivin[3] and I. S. Timofeev[3]

[1] *Joint Institute for High Temperatures of Russian Academy of Sciences, Moscow, 125412 Russia*
[*] *E-mail: vasilyak@ihed.ras.ru*
[2] *Moscow Institute of Physics and Technology, Moscow Region, Dolgoprudny, 141701 Russia*
[3] *NPO "LIT", Moscow Region, Dolgoprudny, 141701, Russia*

Received 16.06.2025; revised 15.08.2025; accepted 20.10.2025

The prospects of using UV radiation from 222 nm excimer KrCl lamps for disinfection of air and surfaces are analyzed. The alleged main advantages of 222 nm radiation, which include the ability to disinfect in the presence of humans, and a higher bactericidal efficacy compared to the wavelength of 254 nm, are being tested experimentally. Studies show conflicting results about the safety of such radiation for the skin and for the eyes of mammals. It has been established that there is an effect on tissues, but it has not yet been proven that it is safe with prolonged multiple exposures. Inactivation of viruses and simple bacteriological strains by UV radiation of 222 nm and 254 nm is achieved at similar UV doses, however, UV radiation of 254 nm has a significant advantage for larger objects (endospores, fungi, fungal hyphae). The efficiency of 222 nm UV radiation generation in industrial KrCl lamps is 3–5 %, which is significantly less than for low-pressure mercury and amalgam lamps 30–35 %.

Keywords: air; disinfection; UV radiation; 222 nm.

DOI: 10.51368/2949-561X-2025-5-5-10

Introduction

The COVID-19 pandemic showed that indoor air and surface disinfection is still a critical issue and has prompted renewed investigation of proven germicidal UV disinfection, which effectively lowers airborne pathogen transmission [1]. Low-pressure mercury and amalgam lamps are the primary sources of germicidal UV radiation at 254 nm (UV-254 nm), which affects the DNA and RNA of microorganisms. As an alternative, it is proposed to use UV light between 200 and 235 nm, in particular the 222 nm output of an excimer lamp based on krypton and chlorine (KrCl) with a wavelength of 222 nm (UV-222 nm). It has been reported that for certain microorganisms, UV disinfection at 222 nm is more effective than at 254 nm, and it has been suggested that disinfection could be performed in the presence of people because the penetration depth of 222 nm radiation in human skin is only a few micrometers, being fully absorbed by the stratum corneum of dead cells and unable to reach the viable cells of the epidermis [1–5]. In this regard, we reviewed studies on the effectiveness of 222 nm UV produced by KrCl excimer lamps for disinfection and assess the safety of using them in the presence of people.

KrCl excimer lamp

Currently, the krypton–chloride (KrCl) excimer lamp, with a primary emission peak at 222 nm, is the most promising source of far germicidal UV radiation [5–10]. The common design of an excimer lamp is a cylindrical, coaxial quartz bulb with inner and outer walls,

filled with krypton plus a trace of chlorine, and fitted with two electrodes: a solid metal tube as the inner electrode and a metal wire cloth as the outer electrode. The barrier discharge in the lamp is created by high-voltage pulses with 4–10 kV amplitude.

The figure shows the spectral emission frequency of a KrCl excimer lamp.

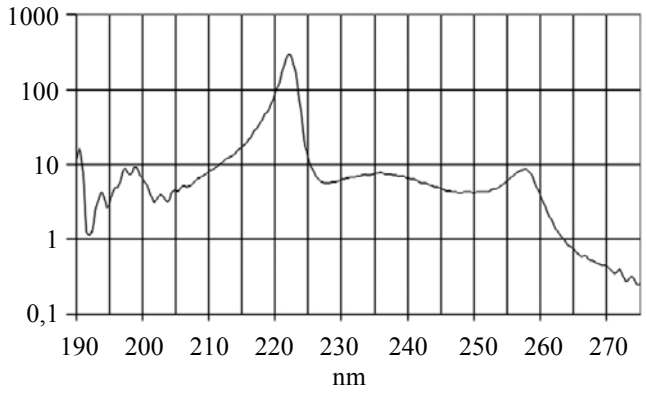

Fig. Distribution of spectral emissive power of KrCl lamp radiation

The majority of the UV radiation power is concentrated around the 222 nm line, showing only minor emissions in the regions below 210 nm and above 230 nm. Some manufacturers add filters that transmit the primary 222 nm line while attenuating other wavelengths. Excimer lamps can reach peak linear electrical powers up to 1 W/cm^2 at high voltage pulse repetition rates (100 kHz), exceeding those of low-pressure mercury vapor lamps but less for amalgam lamps. Power supplies for excimer lamps are more expensive than those for amalgam lamps of comparable power. An undeniable benefit of excimer lamps in specialized environments is the absence of mercury. Although the stated lifespan for KrCl lamps is typically 4.000–5.000 hours, manufacturers generally omit data regarding the degradation of UV radiation output as the lamps approach the end of their service life. For comparison, the service life of low pressure amalgam and mercury lamps is 8.000–16,000 hours, during which UV radiation is guaranteed to decrease by no more than 15 %. The electrical power of series-produced KrCl lamps ranges from 2 W to 800 W, with bulb lengths of 6 to 100 cm [10]. Laboratory devices can reach up to 15 % efficiency for generating 222 nm UV, while industrial lamps typically achieve only 3–5 %, which is less magnitude than the efficiency of producing 254 nm UV with low pressure mercury and amalgam lamps. High power excimer lamps demand supplementary cooling of the bulb to sustain the manufacturer specified UV radiation and longevity, making reliable operation a complex technical task in real-time use.

Bacteriological action of UV studies with 222 nm wavelength

The primary stated benefit of UV-222 nm radiation disinfection is its ability to effectively inactivate microorganisms and viruses while being safe for the skin and eyes of mammals [2–4, 11–22]. UV-222 nm radiation is significantly absorbed by proteins (by the peptide bonds within them), as well as other biomolecules [13]. Its penetration depth is limited to a few micrometers in the outer layers of dead skin, which is less than that of 254 nm radiation [11, 14]. Given that US regulations specify a maximum daily dose (fluence) of 25 mJ/cm^2 for UV-222 nm is four times greater than the 6 mJ/cm^2 limit for 254 nm, this creates an added incentive for further research. Another concept was that the efficacy of UV-222 nm would surpass that of 254 nm, resulting in lower required doses (fluences) to inactivate microorganisms. However, the inactivation efficiency for various types of bacteria and spores was found to be both greater and lesser compared to that of 254 nm radiation [3, 8, 9, 17, 18]. For the inactivation of the viruses examined, the doses of UV radiation in the range of 200–230 nm were less than those required for UV-254 nm. As the wavelength shortens, the absorption of radiation by proteins rises [8, 9, 11], and the damage to proteins also starts to contribute to the eradication [8, 9, 16].

UV radiation at 222 nm is equally effective as 254 nm in inactivating *Staphylococcus aureus* on model human skin when administered at 254 nm [3, 8, 9]. References [17, 18] demonstrated that both 222 nm and 254 nm UV radiation were equally effective in inactivating a range of bacteria. However, when treating endospores of *Bacillus cereus* and *Clostridium sporogenes*, as well as strains of fungi such as *Aspergillus niger* and *Trichophyton rubrum*, the effectiveness of 254 nm UV radiation was significantly greater than that of 222 nm. For

example, in order to inactivate *Aspergillus niger* spores using 222 nm radiation, a dose of 500 mJ/cm^2 is required, whereas only half that dose is needed for 254 nm radiation. Fungal growth and hyphae development in *Aspergillus niger* were significantly inhibited at a UV-254 nm dose of 250 mJ/cm^2, while 222 nm radiation demonstrated only a slight impact on hyphae growth, even at a dose of 1000 mJ/cm^2 [17, 18].

Variations in the sensitivity of microorganisms to radiation may be influenced by factors such as their size and genome size. Additionally, for viruses, characteristics like a viral envelope (whether they are enveloped or non-enveloped), the thickness of that envelope, and the proteins contained within it may also play a significant role. For example, pigmentation of microorganisms (for some types of fungi) may also be the cause of decreased sensitivity to UV radiation.

Viruses are inactivated by UV radiation in the 200-230 nm range at lower doses compared to UV-254 nm [8, 9, 17, 18]. For example, human coronavirus analogues from the alpha (HCoV-229E) and beta (HCoV-OC43) subgroups were inactivated with an efficiency of 99.9 % at 1.7 and 1.2 mJ/cm^2 irradiation doses, respectively [5]. These doses are considerably lower than those required for inactivating the SARS-CoV-2 coronavirus at 254 nm. Reference [5] states that 222 nm radiation is effective against viruses and microorganisms smaller than 5 μm. However, it is also indicated that the effectiveness of this radiation on larger objects has not been thoroughly studied. In references [8, 9], comparative data is provided on the inactivation of bacteria and viruses using various UV radiation wavelengths emitted by different excimer lamps. These studies found that while 222 nm and 254 nm UV radiation wavelengths were similarly effective at inactivating bacteria, UV-222 nm was significantly more effective against viruses. Several factors may contribute to the increased sensitivity of bacteriophages to radiation in the 200–240 nm range compared to UV-254 nm [8, 9]. One suggestion is that short-wave UV radiation damages both the viral nucleic acid (DNA or RNA) and the proteins comprising the capsid (viral envelope). These proteins are crucial because they protect the viral nucleic acid and also enable the virus to adsorb (attach) to host cells, meaning their damage leads to a loss of infectability.

Due to increased absorption and scattering by proteins at shorter wavelengths, the penetration depth into biological tissue decreases [11, 13, 14]. This reduction may, depending on exposure conditions, lead to less effective microorganism inactivation. A study [19] demonstrated that media such as sweat, albumin, and wound effluent significantly reduced the inactivating effect of 222 nm radiation more so than that of 254 nm radiation when irradiating microorganisms. Since airborne microorganisms are typically found in protein-layered aerosols, 222 nm radiation is absorbed strongly than 254 nm. This means that the actual disinfection doses for UV-222 nm in practical applications will be significantly higher than those obtained in ideal laboratory conditions. It is important to note that the bactericidal efficacy of UV-222 nm has only been measured for a limited range of microorganisms. Substantial research is therefore required for a wider range of pathogens, as well as studies on how environmental conditions affect its disinfection efficacy.

Safety of UV radiation with 222 nm wavelength

The safety of UV-222 nm irradiation for human presence has primarily been assessed by evaluating DNA damage in eukaryotic cell cells through in vitro and in vivo models [2, 3, 15]. A study [16] demonstrated that irradiation of human and animal cells induced a small number of DNA dimers (cancer markers), which disappeared within 24 hours. UV radiation at 222 nm produced no erythema, cell death, or inflammatory response, even at the highest exposure levels [16]. However, a study [4] demonstrated that a 40 mJ/cm^2 dose led to the formation of radical compounds in reconstructed human skin.

Studies [20, 21] revealed a risk of cancer development from exposure to the full spectrum of radiation from a KrCl lamp if an optical bandpass filter is not used to cut off wavelengths shorter and longer than 222 nm. Lamps with filters did not induce elevated levels of DNA dimers (cancer markers) at a daily dose of

23 mJ/cm². The use of such filters will reduce the source's overall radiation intensity and increase equipment costs. Furthermore, the stability of such filters over several thousand hours of operation has not yet been studied

A study [22] demonstrated that UV-254 nm exposure resulted in significantly greater formation of reactive oxygen species and inflammatory responses compared to UV-222 nm. Reactive oxygen species are formed even at doses of 25 mJ/cm^2, which is a level permitted by US health standards, and can consequently slow skin regeneration for 48 hours. Studies [22] involving long-term (up to 40 days) indirect exposure to 222 nm radiation, at the maximum permissible dose of 25 mJ/cm^2, revealed minor skin damage. However, these observed damages and morphological skin changes persist, posing a serious long-term risk with periodic exposure, including premature skin aging. The authors of [22] conclude that alterations in skin regeneration mechanisms raise concerns regarding the direct effects of UV-222 nm.

Regarding eyes safety, rat experiments [23] showed that 222 nm UV radiation is absorbed by the outer layers of the corneal epithelium, preventing it from reaching the retina and lens (with slight thinning observed at very high doses). This suggests that serious consequences for humans are unlikely to happen. Research into the effects of far-UV radiation on the eyes is ongoing, and its safety has not yet been definitively established.

Before UV-222 nm can be used in public places with people present, chronic exposure studies must be conducted, specifically including exposure to the eyes and skin. Furthermore, potentially vulnerable groups such as children, the elderly, and individuals with skin or eye diseases, as well as the effects of deep UV radiation on those taking photosensitizing drugs, must also be considered. While studies [24, 25] address this topic, they are not yet conclusive regarding the safety of 222 nm radiation for humans.

Ozone generation by an KrCl excimer lamp

While the KrCl lamp's spectrum (see figure) contains a small amount of radiation below 200 nm that can generate ozone, the main 222 nm wavelength will contribute insignificantly to the generation. With the use of additional bandpass optical filters, overall ozone generation will be negligible. Pulsed microdischarges, occurring in gaps of approximately 100 μm or more between a metal wire cloth exterior electrode and the surface of a quartz flask, can also be a source of ozone. The amount of ozone generated will depend on the size and number of gaps, voltage amplitude, and lamp power [8, 9, 26]. Some manufacturers have overcome this problem by using a complex and expensive technology: directly printing electrodes onto the quartz to eliminate gaps.

Studies [8, 9, 26] provided estimates for the indoor ozone generation from commercial pulsed KrCl excimer lamps operating at 222 nm. Ozone generation is 0.012 mg/h for a low-power device with a 12 W Ushio Care 222 B1 module. The module contains four KrCl excimer lamps, each equipped with a quartz window and a bandpass filter that emits only UV-222 nm. Even after 24 hours of continuous operation in a 30 m^2 room, the module's ozone concentration reached only 0.009 mg/m^3. This level is undetectable by human senses and significantly lower than the maximum permissible ozone concentration of 0.03 mg/m^3 for atmospheric air in populated areas. However, a 70 W KrCl lamp with a wire cloth exterior produced ozone at a rate of 12 mg/h. This would lead to an ozone concentration of 0.36 mg/m^3 in a 30 m^3 room within one hour, significantly exceeding maximum permissible concentrations. The main reason for the high ozone generation rate is the design of the wire cloth exterior. Consequently, KrCl lamps can generate dangerous ozone concentrations in rooms without ventilation.

Conclusion

Currently, the primary claimed advantage of UV-222 nm from KrCl excimer lamps, its ability to disinfect air and surfaces in the presence of people, is undergoing active testing, but final conclusions are yet to be reached. Studies present conflicting results regarding the safety of such radiation for mammalian skin and eyes. While an effect on tissue has been established, its safety has not yet been proven. Little research has been

conducted on the safety issues associated with chronic exposure. The effects of 222 nm UV radiation on vulnerable groups, such as healthcare workers, children, the elderly, and individuals with skin or eye diseases, have not been addressed.

The bacteriological efficacy of 222 nm UV radiation has no advantage over 254 nm UV radiation from mercury and amalgam lamps. While both types of ultraviolet light achieve similar inactivation rates for airborne viruses and simple bacteria at comparable doses, 254 nm UV offers a significant advantage when disinfecting larger entities (like endospores, fungi, and fungal hyphae). 222 nm radiation is absorbed far more strongly by these proteins than 254 nm radiation because airborne microorganisms are often encased in protein-rich aerosols or have protein layers. This significantly reduces 222 nm UV's inactivating effect, necessitating practical doses several times higher than laboratory ones, thus negating any advantage compared to UV-254 nm.

Low-pressure mercury and amalgam lamp systems substantially outperform KrCl excimer lamps in terms of energy consumption, efficiency, service life, and cost.

KrCl lamps can produce negative significant concentrations of ozone in the air depending on their design, power, and operating time.

KrCl lamps can only be used for disinfection in special conditions that require the complete absence of people.

REFERENCES

1. Vasilyak L. M., Plasma Phys Rep. **47**, 318 (2021).
2. Barnard I. R. M., Eadie E. and Wood K., Photodermatology, Photoimmunology & Photomedicine **36** (6), 476–477 (2020). doi: 10.1111/phpp.12580
3. Buonanno M., Ponnaiya B., Welch D., Stanislauskas M., Randers-Pehrson G., Smilenov L. and Brenner D. J., Radiation Research **187** (4), 493–501 (2017). doi: 10.1667/rr0010cc.1
4. Yamano N., Kunisada M., Kaidzu S., Sugihara K., Nishiaki-Sawada A., Ohashi H. and Nishigori C., Photochemistry and Photobiology **96** (4), 853–862 (2020). doi: 10.1111/php.13269
5. Buonanno M., Welch D., Shuryak I. and Brenner D. J., Sci. Rep. **10** (1), 10285 (2020). doi: 10.1038/s41598-020-67211-2
6. Sosnin E. and Tarasenko V., Photonics, No. 1/49/, 60–69 (2015).
7. Lomaev M. I., Skakun V. S., Sosnin E. A., Tarasenko V. F., Shitts D. V. and Erofeev M. V., Phys. Usp. **46**, 193–209 (2003).
8. Sosnin E. A., Skakun V. S., Panarin V. A., Avdeev S. M. and Sorokin D. A., Journal of Optical Technology **88** (10), 587–592 (2021).
9. Sosnin E. A. and Zhdanova O. S., Quantum Electronics **50** (10), 984–988 (2020).
10. https://uv-can.com/collections/far-uv-222nm-disinfection-components/products/helios-far-uv-222nm-excimer-lamp (accessed July 05, 2025).
11. Blatchley III E. R., Brenner D. J., Claus H., Cowan T. E., Linden K. G., Liu Y., Ted Mao, Sung-Jin Park, Piper P. J., Simons R. M. and Sliney D. H., Critical Reviews in Environmental Science and Technology **53** (6), 733–753 (2022). doi: 10.1080/10643389.2022.2084315
12. Welch D., Buonanno M., Grilj V., Shuryak I., Crickmore C., Bigelow A. W., Randers-Pehrson G., Johnson G. W. and Brenner D. J., Scientific Reports **8** (1), 2752 (2018). doi: 10.1038/s41598-018-21058-w
13. Setlow J. The molecular basis of biological effects of ultraviolet radiation and photoreactivation. In Current topics in radiation research, M, E.; A, H., Eds. North Holland Publishing Company: Amsterdam, 1966. Vol. II. P. 195–248.
14. Buonanno M., Stanislauskas M., Ponnaiya B., Bigelow A. W., Randers-Pehrson G., Xu Y. and Brenner D. J., PLoS ONE **11** (6), e0138418 (2016). doi: 10.1371/journal
15. Narita K., Asano K., Morimoto Y., Igarashi T. and Nakane A., PLoS ONE **13** (7), e0201259 (2018). doi: 10.1371/journal.pone.0201259.
16. Hessling M., Haag R., Sieber N. and Vatter P., GMS Hyg Infect Control **16**, Doc07 (2021). doi: 10.3205/dgkh000378
17. Narita K., Asano K., Naito K., Ohashi H., Sasaki M., Morimoto Y., Igarashi T. and Nakane A., J. Hosp Infect. **105** (3), 459–467 (2020). doi: 10.1016/j.jhin.2020.03.030
18. Ohashi H., Koi T. and Igarashi T., Journal of Science and Technology in Lighting **44**, 9–11 (2020). doi: 10.2150/jstl.IEIJ20A000006

19. Zwicker P., Schleusener J., Lohan S. B., Busch L., Sicher C., Einfeldt S., Kneissl M., Kuhl A. A., Keck C. M., Witzel C., Kramer A. and Meinke M. C., Sci Rep. **12** (1), 2587 (2022). doi: 10.1038/s41598-022-06397-z
20. Buonanno M., Welch D. and Brenner D. J., Photochemistry and Photobiology **97** (3), 517–523 (2021). doi: 10.1111/php.13383
21. Woods J. A., Evans A., Forbes P. D., Coates P. J., Gardner J., Valentine R. M. and Moseley H., Photodermatology, Photoimmunology & Photomedicine **31** (3), 159–166 (2015). doi: 10.1111/phpp.12156
22. Tavares R. S. N., Adamoski D., Girasole A. et al., J. Photochem Photobiol B. **243**, 112713 (2023). doi:10.1016/j.jphotobiol.2023.112713
23. Kaidzu S., Sugihara K., Sasaki M., Nishiaki A., Ohashi H., Igarashi T. and Tanito M., Photochemistry and Photobiology **97** (3), 505–516 (2021). doi: 10.1111/php.13419
24. Sugihara K., Kaidzu S., Sasaki M. et al., Photochem Photobiol. **99** (3), 967–974 (2023). doi: 10.1111/php.13710
25. Kousha O., O'Mahoney P., Hammond R., Wood K. and Eadie E., Photochem Photobiol. **100**, 137–145 (2024). doi: 10.1111/php.1380
26. Claus H., Photochemistry and Photobiology **97** (3), 471–476 (2021). doi: 10.1111/php.13391

About authors

Vasilyak Leonid Mikhailovich, Doctor of Physical and Mathematical Sciences, Senior Research Assistant, Joint Institute for High Temperatures of Russian Academy of Sciences (125412, Russia, Moscow, 13, Izhorskaya st., bldg. 2). E-mail: vasilyak@ihed.ras.ru SPIN code: 5623-5167, AuthorID: 19599, ORCID 0000-0001-6982-3038, Scopus 7004886755

Kudryavtsev Nikolay Nikolaevich, president, academician, Moscow Institute of Physics and Technology, (141701, Russia, Moscow region, Dolgoprudny, 9, Institutsky lane). AuthorID: 19586, Scopus 7006127196

Kostyuchenko Sergey Vladimirovich, Candidate of Physical and Mathematical Sciences, Deputy Director for Science, NPO "LIT", (141701, Russia, Moscow region, Dolgoprudny, 25, Likhachevsky driveway). E-mail: lit@lit-uv.ru AuthorID: 19597, ORCID 0009-0005-7450-8741

Sivin Denis Olegovich, Candidate of Technical Sciences, Head of the Laboratory NPO "LIT", (141701, Russia, Moscow region, Dolgoprudny, 25, Likhachevsky driveway). E-mail: light@lit-uv.ru AuthorID: 139704, ORCID 0000-0002-6341-6180, Scopus 8351574400

Timofeev Ivan Sergeevich, Candidate of Physical and Mathematical Sciences, Technical Director of the Equipment Engineering Department, NPO "LIT", (141701, Russia, Moscow region, Dolgoprudny, 25, Likhachevsky driveway). E-mail: timofeev@lit-uv.ru SPIN code: 6932-1594, AuthorID: 839789

PHOTOELECTRONICS

UDC 621.315.592
EDN: GUEYLP

PACS: 73.40QV, 73.21AS, 85.60GZ, 73.61GA

Study of surface leakage currents in LWIR *n*B*n* HgCdTe photosensitive structure with superlattice barrier

A. V. Voitsekhovskii[1,*], S. M. Dzyadukh[1], D. I. Gorn[1], S. A. Dvoretskii[1,2], N. N. Mikhailov[1,2], G. Yu. Sidorov[2] and M. V. Yakushev[2]

[1] *National Research Tomsk State University, Tomsk, 634050 Russia*
[*] *E-mail: vav43@mail.tsu.ru*
[2] *A. V. Rzhanov Institute of Semiconductor Physics SB RAS, Novosibirsk, 630090 Russia*

Received 18.07.2025; revised 4.08.2025; accepted 20.10.2025

The studies of n-B(SL)-n and MI-n-B(SL)-n structures formed on the basis of epitaxial films grown by the MBE method from HgCdTe with a superlattice in the barrier region are carried out. The composition in the absorbing layer of the structures is designed for operation in the LWIR range and was 0.22. Two different superlattice architectures were fabricated and studied. The study of dark currents of n-B(SL)-n structures showed that for both types of samples an anomalous dependence of the current density on temperature is observed with a minimum of the current density at temperatures of 100–120 K. The dominance of the surface leakage current components was revealed for both structures. Based on the study of the admittance of MI-n-B(SL)-n structures, it is shown that the characteristics of the studied structures have a form similar to the characteristics of MIS structures fabricated on the basis of homogeneous $Hg_{0.78}Cd_{0.22}Te$.

Keywords: HgCdTe; molecular beam epitaxy; barrier structure; nBn; superlattice; surface current.

DOI: 10.51368/2949-561X-2025-5-11-18

Introduction

HgCdTe-based unipolar barrier *n*B*n* structures are considered promising for development of infrared (IR) photodetectors for the long-wave infrared (LWIR, 8–14 μm) spectrum that operate at higher cooling temperatures than conventional HgCdTe photodiodes [1]. Among the architectures for barrier photosensitive structures having the high potential there are *n*-type HgCdTe-based *n*B*n* structures grown by molecular beam epitaxy (MBE) [2]. Currently, the most promising configuration is considered to be a structure with a barrier formed as a superlattice (SL) – *n*-B(SL)-*n* structures. Modifying the SL parameters (layer compositions and thicknesses) allows for controlling the positions of energy band edges in the barrier layer of the *n*B*n* structure and minimizing discontinuities of energy bands at the absorption layer / barrier / contact layer heterointerfaces [3].

The today's world academic literature offers very few studies devoted to the fabrication and experimental study of HgCdTe-based *n*B*n* structures with a SL barrier [4–7]. Most works on HgCdTe-based *n*B*n* structures are theoretical and describe the simulation of various heterostructure configurations aimed at reducing dark currents and increasing sensitivity. In particular, there are no works devoted to the study of HgCdTe-based *n*-B(SL)-*n* structures tailored to the LWIR range.

Practical implementation of HgCdTe-based *n*-B(SL)-*n* structures is hindered not only by fundamental issues (such as non-zero valence-band discontinuity [8]) but also by fabrication challenges. Being designed using theoretical

models structures of this type often exhibit characteristics that do not match theoretical predictions during experimental study. This applies equally to the SL barrier layer parameters determined by experimental data and the experimentally measured dark current values. In particular, the dark current-voltage characteristics (CVC) observed during an experiment are known to be often different from theoretical ones due to the prevalence of surface leakage currents. This mechanism of dark current generation occurs due to the specific features of the fabrication technology for experimental samples, primarily of the technology for depositing a passivation layer on the sample surface. Furthermore, currently there is no satisfactory example of modeling and subsequent experimental verification of an effective superlattice barrier layer for a photosensitive HgCdTe-based *n*B*n* structure. One reason for this is the limited number of studies of the development, practical implementation, and experimental study of *n*-B(SL)-*n* HgCdTe structures, due to which the sufficient theoretical and experimental data have not been provided so far.

This paper offers two configurations of photosensitive *n*-HgCdTe-based *n*-B(SL)-*n* structures with a superlattice in the barrier region for the LWIR range. Parameters of the superlattice barrier layers were selected based on theoretical assessments to achieve the maximum possible barrier height for majority charge carriers in the conduction band and the minimum barrier size for minority charge carriers.

This work is dedicated to analyzing the current generation mechanisms in two different LWIR *n*B*n* HgCdTe structures with a superlattice in the barrier region.

Experimental Samples and Methods

Two types of HgCdTe epitaxial films were grown on GaAs (013) substrates. The films were grown at the Institute of Semiconductor Physics, Siberian Branch of the Russian Academy of Sciences, using "Ob-M" molecular beam epitaxy system. To align the structure's epitaxial layers with the substrate, buffer layers of ZnTe (~0.3 μm thick) and CdTe (≥5.5 μm thick) were first grown on substrate surface. This was followed by the sequential growth of the HgCdTe graded-gap base with its composition changing from 0.28 at the interface with CdTe to ~0.22, which corresponded to the composition of the absorbing layer, which was ~5.5 μm thick.

After that a superlattice that acted as a barrier layer was grown, with a contact layer with a composition of ~0.22 of ~0.5 μm in thickness formed on its surface. The films differed in the parameters of their superlattice layers. The superlattice of structure No. 1 consisted of 15 wells, each 12 nm wide, and 16 barriers, each 8 nm wide. The superlattice of structure No. 2 consisted of 15 wells, each 4 nm wide, and 16 barriers, each 8 nm wide. The grown HgCdTe film was intentionally not doped. After being growth, the epitaxial film was etched through a special mask to a depth corresponding to the interface position between the absorbing and barrier layers. As a result, standalone *n*B*n* structures (mesastructures) with diameters ranging from 0.50 mm to 0.02 mm were formed on the film surface.

To study the current characteristics and admittance, two types of experimental samples were fabricated based on the grown epitaxial films: a version with indium electrodes deposited directly on the contact layer (*n*-B(SL)-*n* structure) and a metal-insulator-semiconductor (MIS) version where the electrodes were separated from the contact layer by a functional dielectric layer (MI-*n*-B(SL)-*n* structure). Both structure types featured passivation of the entire non-metallized surface of the epitaxial film with Al_2O_3 dielectric deposited by the plasma-enhanced atomic layer deposition (PE ALD) procedure.

The studies were conducted using an automated heterostructure admittance spectroscopy system which included Keithley 6487 picoammeter, a cryogenic temperature control system, and a vacuum system. This system is capable of maintaining a stable temperature of the sample stage within the range of 11 K to 475 K for extended periods, with a temperature control accuracy not worse than 0.2 K.

Results and their discussion

Figure 1a shows the current density vs. bias voltage dependencies for mesastructures of various diameters at the temperature of 80 K derived for Structure No. 1. As can be seen in the figure the current density at a fixed bias voltage

increases as the mesastructure diameter decreases. To determine the bulk and surface current components, curves of the current density vs. the ratio of mesastructure's perimeter P to mesastructure's area A at the bias voltage of +0.2 These curves are shown in Figure 1*b*. As can be seen in the figure this type of structure features high surface leakage current densities.

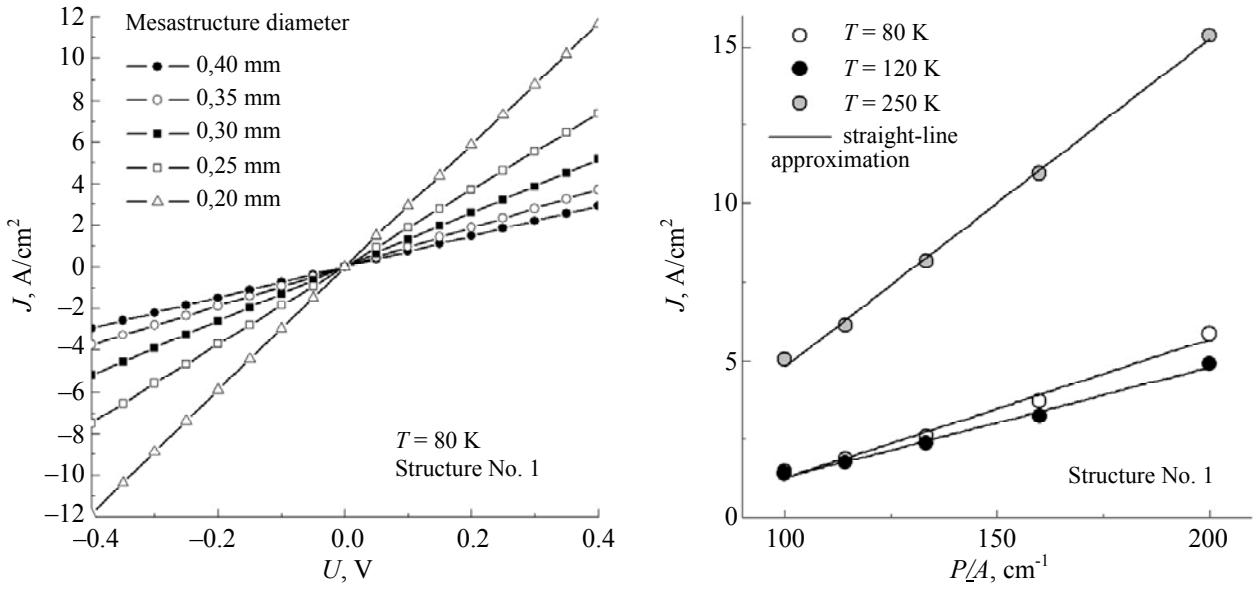

a) *b*)

Fig. 1. Current density J vs. bias voltage U for mesastructures of various diameters at the temperature of 80 K (a), and current density vs. P/A ratio at various temperatures at U = +0.2 V (b) for Structure No. 1

Figure 12a shows current densities vs. voltage dependencies for structures of various diameters at the temperature of 80 K derived for Structure No. 2. This structure can be seen to be also prone to significant increase of current density as the mesastructure diameter decreases at the fixed bias voltage, which indicates a surface leakage current component of considerable magnitude. The plotted curves of current density vs. the ratio of the structure's perimeter to the structure's area at the bias voltage of +0.2 V for Structure No. 2 are shown in Figure 2*b*.

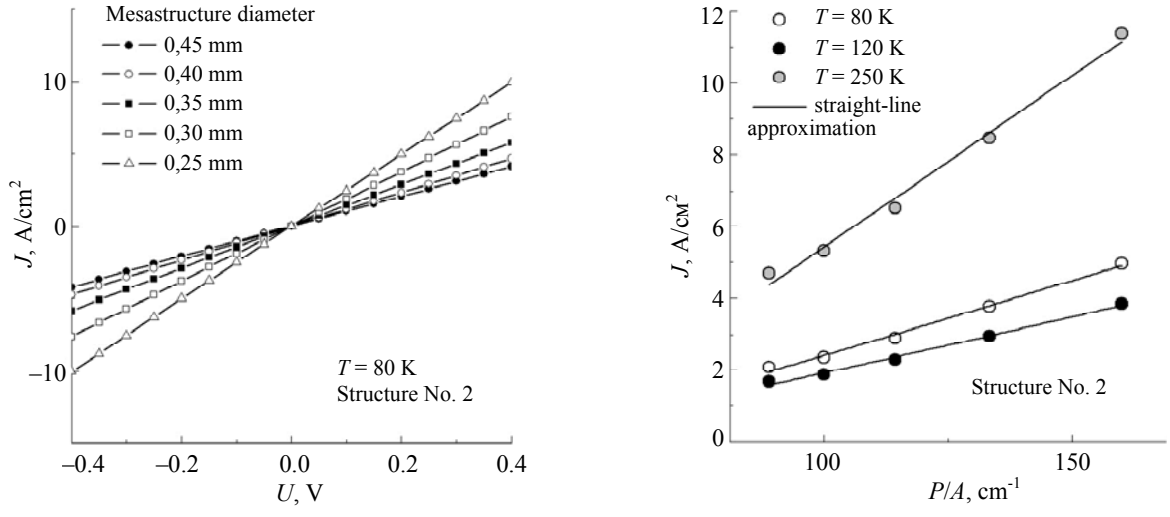

a) *b*)

Fig. 2. Current density J vs. bias voltage U for mesastructures of various diameters at the temperature of 80 K (a), and current density vs. P/A ratio at various temperatures at U = +0.2 V (b) for Structure No. 2

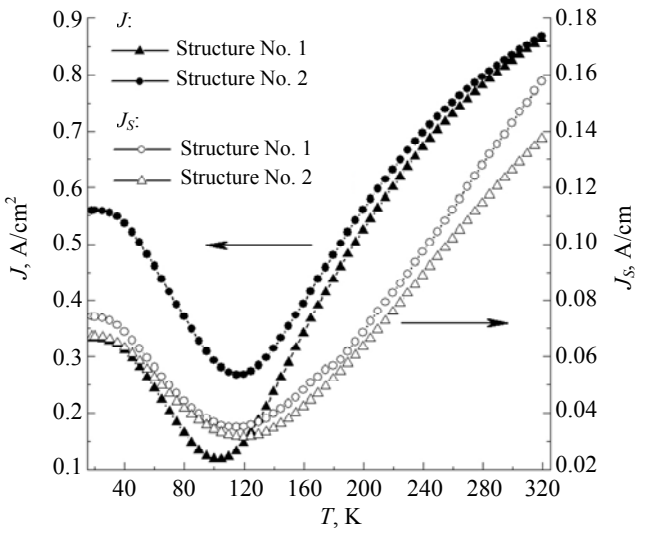

Fig. 3. Total current density J (for a mesastructure with a diameter of 0.4 mm) and surface leakage current density J_S vs. temperature T at the bias voltage of +0.2 V for Structures No. 1 and No. 2

Figure 3 shows the curves of total current density (mesastructure diameter of 0.4 mm) and surface leakage current density vs. sample temperature derived from the slopes of the curves of current density vs. the ratio of structure's perimeter P to structure's area A at various temperatures for Structures No. 1 and No. 2. An anomalous temperature dependence of current density can be seen in the figure for this sample type. These curves show the minimum current density at temperatures of 100–120 K. For mesastructures of various diameters made of the same epitaxial film, positions of the minima coincide. However, the minima occur at various temperatures for structures made of film No. 1 and film No. 2. The curves of surface leakage current density vs. sample temperature also show a minimum, but in this case the minima for Structures No. 1 and No. 2 practically coincide. The values of surface leakage current components at similar temperatures obtained for the studied samples approach each other. The maximum difference in current density values across the entire temperature range studied does not exceed 15 %. This allows concluding that the structure passivation technology exhibits good stability. It is not feasible to determine the bulk current component due to the prevailing surface leakage current component, which makes further direct current studies uninformative.

In such a situation, the admittance spectroscopy method [9] is well suited for analyzing the fabricated structures. The equivalent circuits method was used to process the admittance measurements. The equivalent circuits and formulas for determining the series resistance can be found in reference [10]. Figure 4 shows the curves for the reciprocal of series resistance R_S of the epitaxial film volume, extracted from the admittance measurements using the equivalent circuits method, vs. temperature for Structures No. 1 and No. 2, with mesastructure diameters being 0.35 mm. The data were obtained at the frequency of 1 MHz in the enhancement mode. The figure shows that the temperature curves of $1/R_S$ for samples No. 1 and No. 2 are qualitatively similar to those of the surface leakage current components.

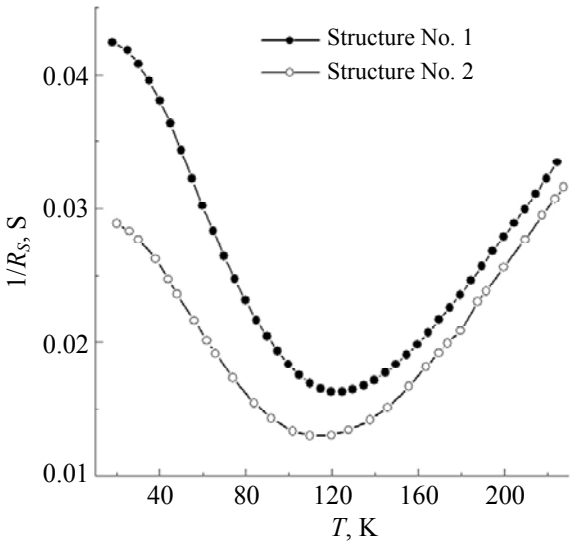

Fig. 4. $1/R_S$ value vs. temperature for Structures No. 1 and No. 2 with mesastructure diameters of 0.35 mm at the frequency of 1 MHz

Figures 5*a* and 5*b* show capacitance-voltage (C-V) curves of Structures No. 1 and No. 2 with a mesastructure diameter of 0.5 mm as measured at the temperature of 15 K. Here, C is the electrical capacitance. Measurements were made at identical bias voltage sweep rates and directions. The series resistance of the epitaxial film volume has been excluded from the measurement results. As can be seen in the figures, the flat-band voltage for the first structure has a value approaching the zero bias voltage. This means that these structures do not have any significant fixed charge in the dielectric coating. However, the flat-band voltage for sample No. 2 has a positive value and is greater in magnitude than that for sample No. 1.

Concentration of majority charge carriers for sample No. 1 as determined from the slope of the squared capacitance reciprocal in the depletion mode at the frequency of 1 MHz, was $1{,}24\times10^{21}$ m^{-3}. In the temperature range from 15 K to 150 K, this yields the maximum width of the space-charge region (SCR) of 3.80×10^{-7} m to 2.18×10^{-7} m. Since the contact layer thickness of 5.0×10^{-7} m, it means that the space-charge region does not reach the barrier layer with the superlattice. In terms of the equivalent circuits model, this means the barrier layer impacts only the series resistance of the epitaxial film volume. Concentration of majority charge carriers for sample No. 2 as determined under the same conditions was 7.65×10^{20} m^{-3}. In the temperature range from 15 K to 120 K, this yields a maximum SCR width of 4.80×10^{-7} m to 2.28×10^{-7} m. This indicates that SCR for this sample does not reach the superlattice barrier layer either, but only approaches its boundary at the temperature of 15 K.

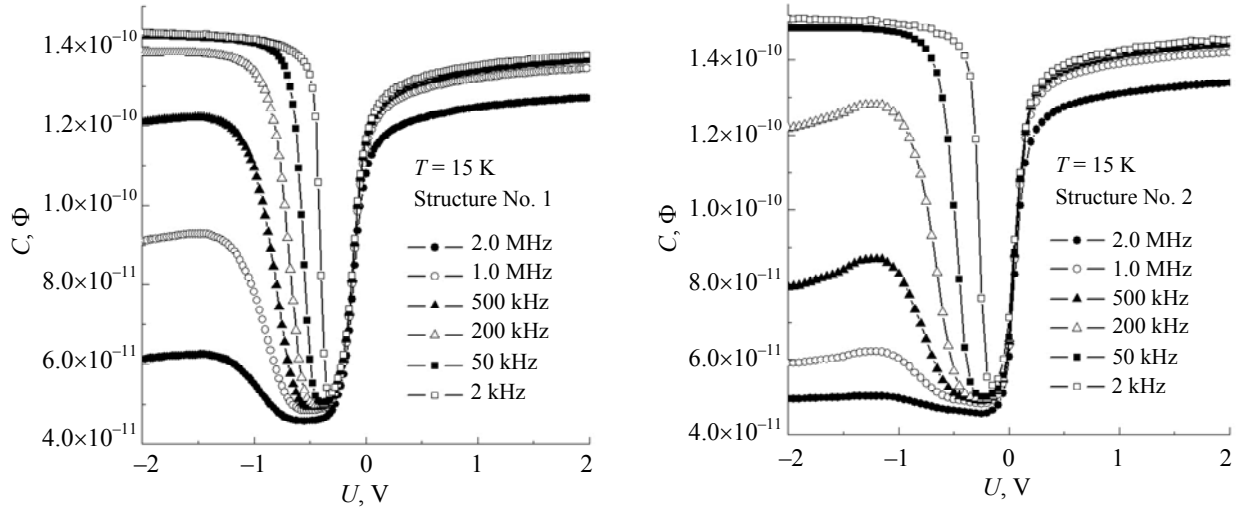

Fig. 5. C-V curve for Structure No. 1 (a) and Structure No. 2 (b) at the temperature of 15 K as measured with forward voltage sweep

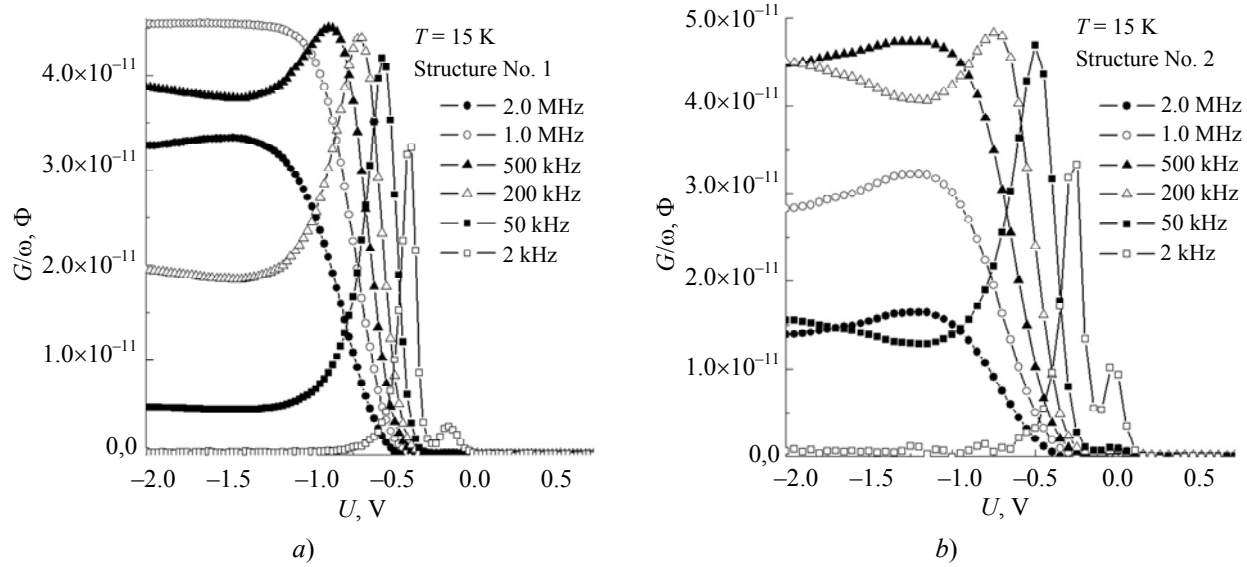

Fig. 6. Differential conductance for Structure No. 1 (a) and Structure No. 2 (b) vs. the bias voltage at the temperature of 15 K as measured with forward voltage sweep

Figure 6 shows the curves of differential conductance for Structures No. 1 and No. 2 as measured at the temperature of 15 K. The series resistance of the epitaxial film volume has also been excluded from the measurement results in the figures shown. The curves of differential

conductance vs. the bias voltage for Structures No. 1 and No. 2 exhibit a peak in the bias voltage region corresponding to the depletion mode, which is associated with the occurrence of the density typical of fast surface states. Their occurrence is due to the absence of a near-surface graded-gap base.

The study of the C-V curves as measured in forward and reverse directions of bias voltage sweep showed that the curves of both structures exhibit minor hysteresis. This indicates a low density of slow surface states; however, the density of surface states for Structure No. 2 is still somewhat higher than for Structure No. 1. Another common feature for both structures is that the hysteresis does not show significant change in the capacitance level at the minimum of the C-V curve, which is typical of structures without a near-surface graded-gap base.

Figure 7 shows the curves of R_DA vs. reciprocal temperature obtained in strong inversion mode (at the bias voltage of -2 V) at the frequency of 1 MHz for samples No. 1 and No. 2. As can be seen in the figure, the SCR resistance of the structures at low temperatures is limited by interband tunneling, while at higher temperatures, R_DA is limited by diffusion of minority charge carriers from the quasi-neutral region. R_DA values for Structure No. 2 are higher than for Structure No. 1, reaching the value of approximately 12.4 Ω·cm^2 at the maximum. The higher values of R_DA in major inversion mode for Structure No. 2 are also confirmed by C-V curve measurements, which exhibit higher frequencies relative to the inversion layer formation time under the same conditions for Structure No. 2.

According to the equivalent circuits method, the series resistance of the epitaxial film volume bears the information about the part of the semiconductor film in the MIS structure which is not included in SCR. Derived from the slope of the curve of the volume resistance reciprocal logarithm vs. $q/(k_B \times T)$ at various frequencies of the alternating test signal were the values of charge carrier activation energy for samples No. 1 and No. 2 provided that they are generated in interband conditions. The curve of the activation energy, which is determined from the temperature vs. series resistance curve, vs. frequency of the alternating test signal is shown in Figure 8. As the frequency increases, the determined activation energy grows linearly in the frequency range from 500 kHz to 2 MHz. It is difficult to interpret such results at this stage and further research is required. However, it should be noted that the activation energy value obtained for sample No. 1 at the 1 MHz frequency is 72 meV, which is more than two times as low as the bandgap energy for HgCdTe with composition $x = 0.22$ in this temperature range ($E_g \approx 0.158$ meV). The activation energy value obtained under the same conditions for sample No. 2 is 147 meV, which is quite close to the bandgap energy for HgCdTe with composition $x = 0.22$. The results presented allow concluding that sample No. 1, unlike sample No. 2, features the energy level within the bandgap. This energy level is derived at high temperatures using the series resistance vs. temperature curve and accounts for the lower differential resistance.

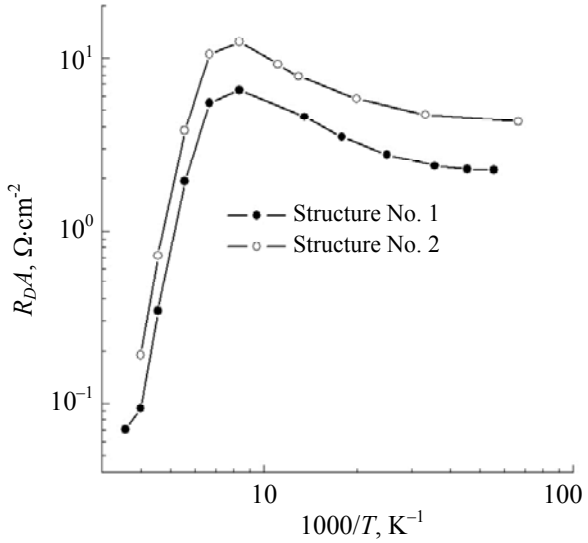

Fig. 7. Curves of R_DA vs. reciprocal temperature obtained in strong inversion at the frequency of 1 MHz for samples No. 1 and No. 2

The presence of mesastructures with various cross-sectional areas on the experimental samples allows for plotting the curve of the reciprocal series resistance of the epitaxial film volume R_S vs. the ratio of mesastructure perimeter R_S to mesastructure area A. Figure 9 shows these curves plotted at different frequencies for sample No. 2. As can be seen in the figure, the curve behavior is compliant with the idea that as the P/A ratio increases, the conductance grows due to the mechanisms associated with current flow over the surface.

Straight-line approximation of these curves allows estimating the conductance component associated with surface leakage based on the curve slope.

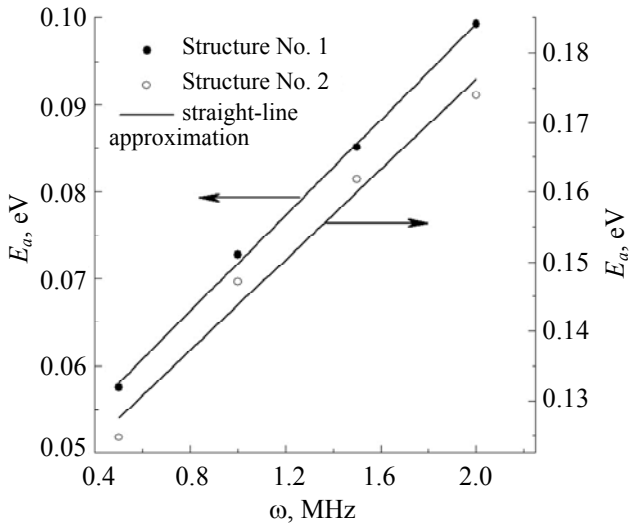

Fig. 8. Determined activation energy E_a vs. alternating test signal frequency ω for samples No. 1 and No. 2

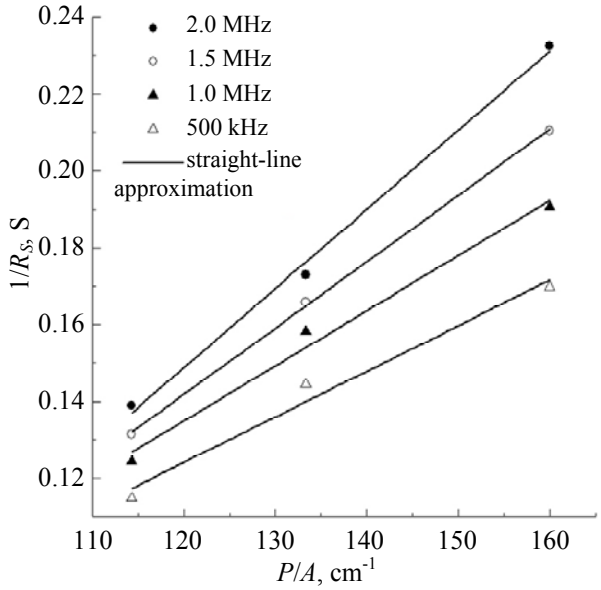

Fig. 9. $1/R_S$ vs. the P/A ratio at various frequencies of the alternating test signal

Figure 10 shows the curves of the conductance component associated with surface current flow processes vs. alternating test signal frequency which are plotted using the slope of the straight-line approximated curves of $1/R_S(P/A)$. As can be seen in the figure, the surface conductance values for sample No. 1 are frequently in excess of the conductance values for sample No. 2 across the entire frequency range studied. This observation correlates to the data shown in Figure 7 and links lower R_DA value of sample No. 1, in part, to its higher surface leakage current.

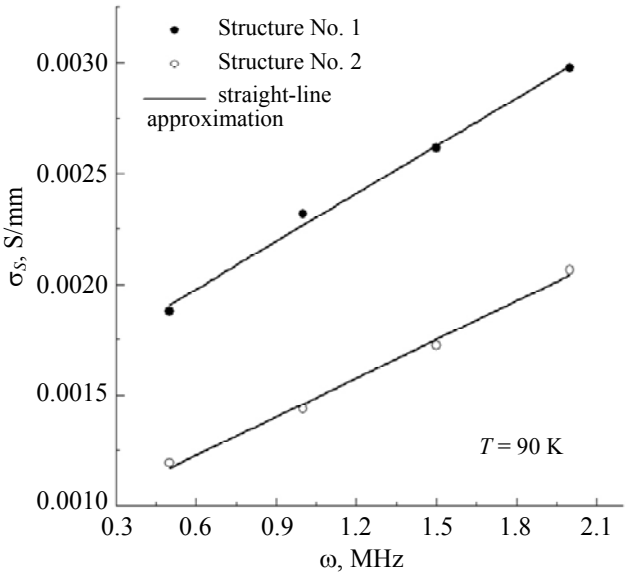

Fig. 10. Surface conductance σ_S vs. alternating test signal frequency ω at the temperature of 90 K

Conclusion

This paper presents the findings of the study of *n*-B(SL)-*n* and MI-*n*-B(SL)-*n* structures formed from epitaxial films grown by the MBE method from the three-component semiconductor HgCdTe with a superlattice in the barrier region. The composition of the structures' absorbing layer is designed for operation in the LWIR range and was 0.22.

The study of dark currents of the *n*-B(SL)-*n* structures revealed that both sample types exhibit an anomalous temperature vs. current density curves, with the current density minimum at temperatures of 100–120 K. The curves of temperature vs. surface leakage current components, as well as the total dark current density, also exhibit minima. Additionally, the study showed that Structure No. 1 features a larger surface leakage current component across the entire temperature range studied.

The admittance spectroscopy studies performed allow concluding that characteristics of the analyzed structures generally resemble those of MIS structures made of homogeneous $Hg_{0.78}Cd_{0.22}Te$. A low density of slow surface states is typical of these structures, which is well illustrated by the plotted C-V curves of the

structures studied. The R_DA vs. temperature curves show the interband tunneling occurring at low temperatures, which is also typical of MIS structures based on homogeneous HgCdTe with a composition of 0.2 and without a graded-gap base. Lower R_DA values for sample No. 1 compared to sample No. 2 are likely due, in part, to its higher surface leakage current values. The fact that the activation energy of sample No. 1 derived from the curve of temperature vs. epitaxial film series resistance is approximately twice as low as the band gap width indicates the presence of generation centers for free charge carriers within the band gap. The activation energy value for sample No. 2 is quite close to the band gap value for HgCdTe with composition $x = 0.22$. The curves of surface leakage current densities and reciprocal series resistance of the epitaxial film volume vs. temperature are qualitatively similar. The reasons for the strong dependence of the samples' activation energy vs. frequency cannot be interpreted at this stage of the study and require further studying.

The study was supported by a grant from the Russian Science Foundation No. 23-62-10021, https://rscf.ru/project/23-62-10021/.

REFERENCES

1. Shi Q., Zhang S.-K., Wang J.-L. and Chu J.-H., J. Infrared Millim. Waves. **41** (1), 139–150 (2022).
2. Voitsekhovskii A. V., Nesmelov S. N., Dzyadukh S. M., Gorn D. I., Dvoretsky S. A., Mikhailov N. N., Sidorov G. Y. Ch. 6, II-VI Semiconductor-Based Unipolar Barrier Structures for Infrared Photodetector Arrays in Handbook of II-VI Semiconductor-Based Sensors and Radiation Detectors. Cham. Springer, 2023. P. 135–154.
3. Kopytko M., Wrobel J., Jozwikowska K., Rogalski A., Antoszewski J., Akhavan N. D., Umana-Membreno G. A., Faraone L. and Becker C. R., Journal of Electronic Materials **44** (1), 158–166 (2015).
4. Benyahia D., Martyniuk P., Kopytko M., Antoszewski J., Gawron W., Madejczyk P., Rutkowski J., Gu R. and Faraone L., Opt Quant Electron. **48**, 215 (2016).
5. Izhnin I. I., Kurbanov K. R., Voitsekhovskii A. V., Nesmelov S. N., Dzyadukh S. M., Dvoretsky S. A., Mikhailov N. N., Sidorov G. Y. and Yakushev M. V., Applied Nanoscience. No. 10, 4571–4576 (2020).
6. Voitsekhovskii A. V., Dzyadukh S. M., Gorn D. I., Dvoretskii S. A., Mikhailov N. N., Sidorov G. Yu. and Yakushev M. V., Journal of Communications Technology and Electronics **68** (2), S132–S137 (2023).
7. Sellers R., Man P., Khalidi Z. El., Ahmad Z., Zangeneh D., Grein C., Krishnamurthy S., Hahn S.-R., Mlynarski T. and Sivananthan S., J. Appl. Phys. **137**, 084502 (2025).
8. Voitsekhovskii A. V., Dzyadukh S. M., Gorn D. I., Mikhailov N. N., Dvoretsky S. A., Sidorov G. Yu. and Yakushev M. V., Journal of Optical Technology **91** (2), 67–76 (2024).
9. Zubkov V. I., Yakovlev I. N., Litvinov V. G., Ermachihin A. V., Kucherova O. V. and Cherkasova V. N., Semiconductors **48**, 917–923 (2014).
10. Voitsekhovskii A. V., Nesmelov S. N. and Dzyadukh S. M., Russian Physics Journal **48** (6), 584–591 (2005).

About authors

Voytsekhovskii Alexander Vasilyevich, Dr. Sci. (Phys.-Math.), Chief Research Scientist, National Research Tomsk State University (634050, Russia, Tomsk, 36 Prospekt Lenina). E-mail: vav43@mail.tsu.ru SPIN code: 2257-4512, AuthorID: 4641

Dzyadukh Stanislav Mikhailovich, Cand. Sci. (Phys.-Math.), Research Scientist, National Research Tomsk State University (634050, Russia, Tomsk, 36 Prospekt Lenina). E-mail: bonespirit@mail2000.ru SPIN code: 5292-6000, AuthorID: 571424

Gorn Dmitry Igorevich, Cand. Sci. (Phys.-Math.), Head of Laboratory, National Research Tomsk State University (634050, Russia, Tomsk, 36 Prospekt Lenina). E-mail: gorn.di@gmail.com SPIN code: 4514-3163, AuthorID: 724442

Dvoretsky Sergey Alekseyevich, Cand. Sci. (Phys.-Math.), Senior Research Scientist, National Research Tomsk State University (634050, Russia, Tomsk, 36 Prospekt Lenina). Rzhanov Institute of Semiconductor Physics, Siberian Branch of the Russian Academy of Sciences (630090, Russia, Novosibirsk, 13 Prospekt Academician Lavrentiev). E-mail: dvor@isp.nsc.ru SPIN code: 8129-7857, AuthorID: 20787

Mikhailov Nikolay Nikolayevich, Cand. Sci. (Phys.-Math.), Senior Research Scientist, National Research Tomsk State University (634050, Russia, Tomsk, 36 Prospekt Lenina). Rzhanov Institute of Semiconductor Physics, Siberian Branch of the Russian Academy of Sciences (630090, Russia, Novosibirsk, 13 Prospekt Academician Lavrentiev). E-mail: mikhailov@isp.nsc.ru SPIN code: 3449-3155, AuthorID: 107682

Sidorov Georgy Yuryevich, Cand. Sci. (Phys.-Math.), Deputy Director, A. V. Rzhanov Institute of Semiconductor Physics SB RAS (630090, Russia, Novosibirsk, 13 Prospekt Academician Lavrentiev). E-mail: george@isp.nsc.ru SPIN code: 2965-0930, AuthorID: 551326

Yakushev Maxim Vitalyevich, Dr. Sci. (Phys.-Math.), Deputy Director, A. V. Rzhanov Institute of Semiconductor Physics SB RAS (630090, Russia, Novosibirsk, 13 Prospekt Academician Lavrentiev). E-mail: yakushev@isp.nsc.ru SPIN code: 2025-2315, AuthorID: 33282

PHOTOELECTRONICS

UDC 53
EDN: GXTOCC
PACS: 07.07.Df, 07.57.-c, 81.05.Ea, 81.65.Rv

Testing array patterns for research dependence performance InSb FPA large-format from pixel topology

A. A. Lopukhin[1,*], E. V. Permikina[1], K. V. Barysheva[1] and V. V. Lopatin[2]

[1] *RD&P Center ORION, JSC, Moscow, 111538 Russia*
[*] *E-mail: alexmatr0@mail.ru*
[2] *Foundation for Advanced Research, Moscow, 121059 Russia*

Received 3.09.2025, revised 15.09.2025; accepted 20.10.2025

The topology of squares mesa and rounded mesa of testing array patterns with 10, 12, 15 and 20 μm pitch based on InSb intended for hybridization with 12 μm pitch 1280×1024 ROIC for research of basic photo-electric characteristics in single FPA large-format are developed. The structure of a complete set of photomasks with distribution over the area of testing array patterns for realization wedge-like thinning is presented in order to obtain ultra-thin structures with a controlled thickness over the area with to increase strength and minimize the crosstalk. Possibilities of realization of the offered testing array patterns are analysed.

Keywords: Focal Plane Array (FPA); indium antimonide; crosstalk; the scanning mask; topology; testing array patterns.

DOI: 10.51368/2949-561X-2025-5-19-26

Introduction

Modern medium-wave infrared array photodetectors with high resolution and wide field of view use photodiode arrays made of InSb for detection of thermal objects [1]. Optical radiation incident on the antireflective surface of the photosensor array generates the photocurrent within array photosensors. Some photocarriers with long diffusion length can be collected in adjacent elements, thus increasing the photoelectric interconnection. As the element pitch decreases, photoelectric interconnection becomes a critical parameter. Additionally, the perimeter-to-area ratio grows inevitably, and the impact of surface leakage currents on the characteristics intensifies. To handle the interconnection issue, structures with thin photosensitive regions are used, which requires stronger array photosensors [2, 3, 4] and finding a compromise between interconnection magnitude and photodetector's response. The homogeneity of photoelectric characteristics of array's elements (particularly of the large-size array) is directly determined by the complexity of array fabrication process.

On the other hand, modern megapixel array photodetectors are based on a hybrid architecture, where the most complex and expensive component is the readout large-scale integrated (LSI) circuit, which requires lengthy development, design, testing, and debugging.

For this reason, it is proposed to use test array structures of array photosensors featuring various topologies and hybridized with a large-scale integrated circuit sized 1280×1024 with a 12 μm pitch to derive the most valid data on dependence of photoelectric characteristics of array photosensors (interconnection, detectivity, photoresponse, etc.) on the elements pitch, photosensitive structure thickness, topology of the photosensitive area (mesa, planar, mesa-planar), and shape of the photosensitive areas (square, circle). To minimize the impact of the wide process spread caused by material inhomogeneities across the wafer area, the test structures are located within a single array, and photoelectric characteristics between

geometrically adjacent elements that differ in topology and pitch are compared (Fig. 1). Comparing photoelectric characteristics within a single array enables a more precise identification of "subtle" differences between the elements.

Studying the photoelectric characteristics of an array photosensor hybridized with a megapixel readout LSI circuit also allows identifying specific functional features of the integrated circuit and, if necessary, adjusting the developed readout LSI.

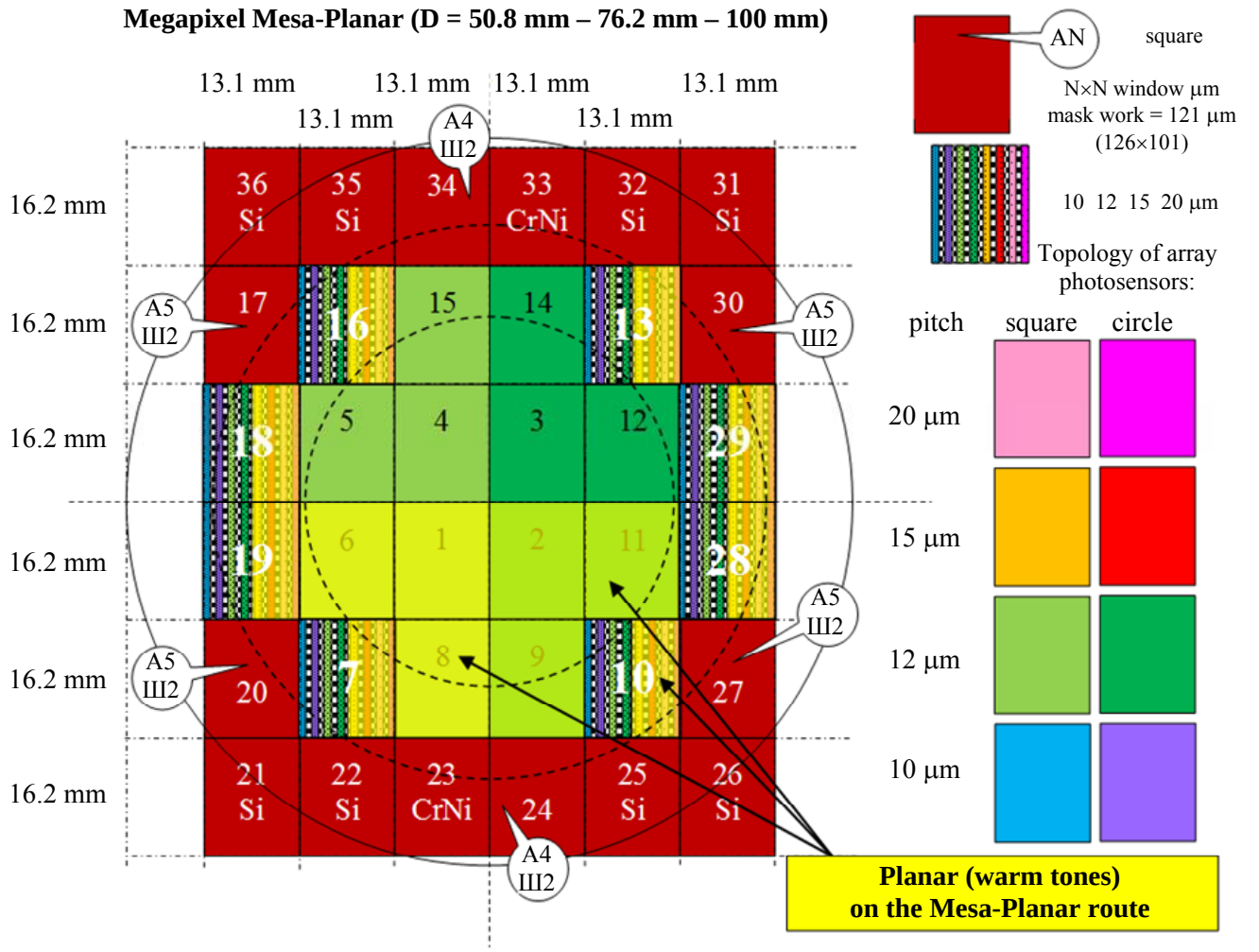

Fig. 1. Layout of test structures on the array photosensor wafer made of InSb (mesa-planar version)

Topoogy of test structures

Figure 1 shows eight test array structures (Nos. 7, 10, 13, 16, 18, 19, 28, 29) featuring square and circular photosensitive area shapes with element pitches of 10, 12, 15, and 20 µm within a single array. Within the mesa-planar process route, it is possible to implement element ranges as strips along the array's longer side (Fig. 2) for architectures that allow combining such versions and comparing their "subtle" features (Fig. 1, 2). Yellow and warm tones show planar versions of photosensitive elements, while light blue tones (Fig. 2, left) – structural variable-area photodiode arrays for assessing the passivation quality of the photosensor arrays [5, 6].

The test array structures can be implemented along with fabrication of array photosensors sized 1280×1024 and having 12 µm pitch on indium antimonide wafers and epitaxial structures with diameters of 76.2 mm and 100 mm. However, corner elements of test arrays can also be made using wafers of 50.8 mm in diameter, followed by hybridization of these corner elements onto a single readout LSI and thinning of the assembly. Thus, test structures do not limit the maximum production of suitable array photosensors within these diameters of wafers.

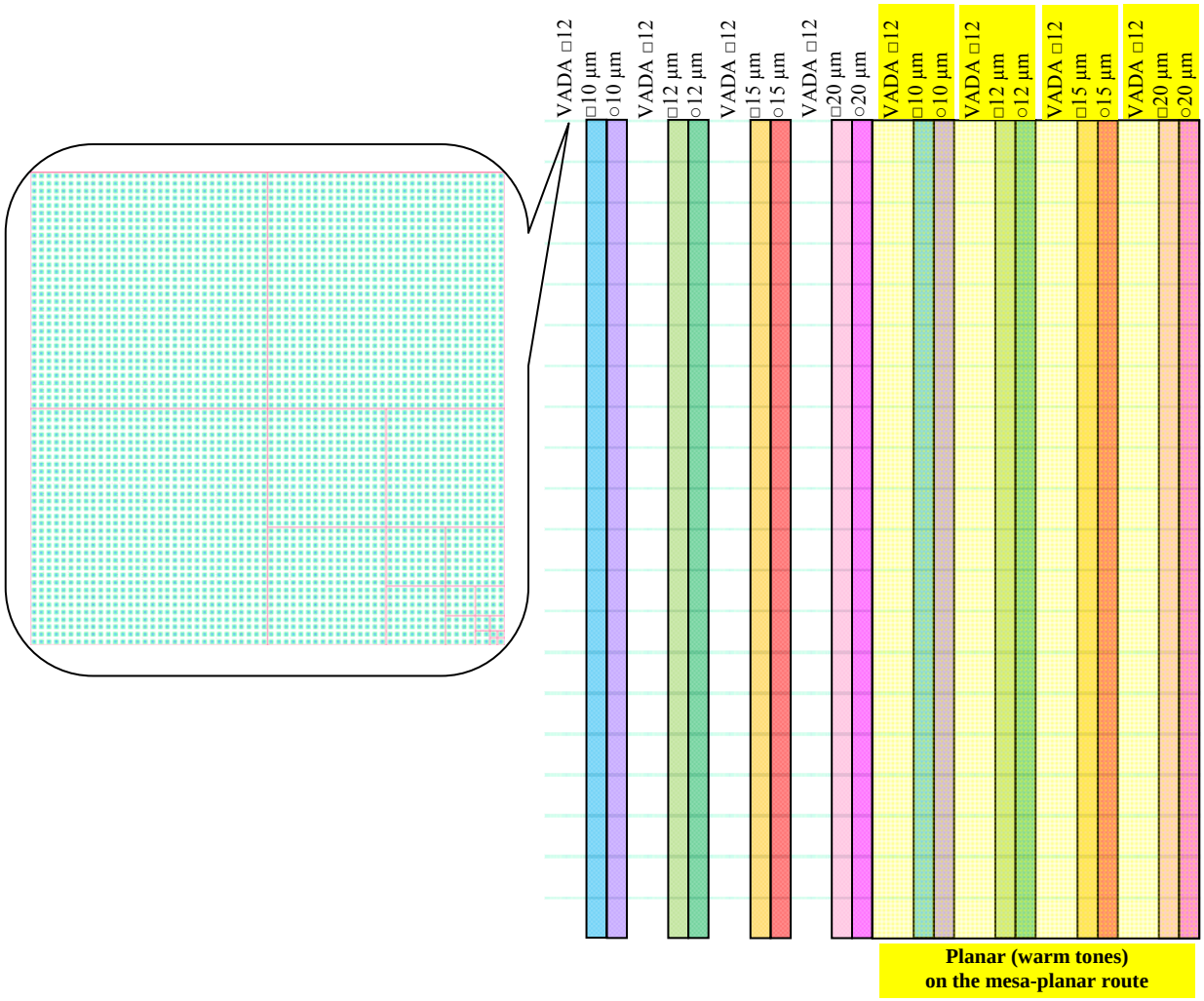

Fig. 2. Test structure versions of array photosensors within a single array: 1/2 of the array to the left – mesa (cold tones); 1/2 of the array to the right – planar (warm tones)

Six main mask works are required for fabrication of array photosensors. The table contains minimum sizes provided by each mask work, considering the photosensor pitch. It is recommended to use the mask work for generation of windows simultaneously for creating scanning masks and chromium-nickel mirrors on the periphery of 100 mm diameter silicon wafers (Window+Si mask work). Scanning masks can be used to study the sensitivity distribution across the pixel area of the array photodetector [7, 8], while chromium-nickel mirrors can be utilized for dark current measurements to determine the passivation efficiency of large-size array photosensors [5, 6]. These test structures are marked in dark red in Figure 1.

Table

Minimum sizes	pitch = 20 μm	pitch = 15 μm	pitch = 12 μm	pitch = 10 μm
1. Mesa mask work	1 μm	1 μm	1 μm	1 μm
2. Planar mask work	2 μm	2 μm	2 μm	2 μm
3. Window+Si mask work	4 μm	4 μm	4 μm	3 μm
4. CrNi mask work	7 μm	7 μm	7 μm	6 μm
5. In mask work	7 μm	7 μm	7 μm	6 μm
6. Groove mask work	5 μm	5 μm	5 μm	5 μm

The main topological feature of array photosensors is square or circular shape of elements (Fig. 3). When good sensitivity and maximum photoresponse are to be achieved, both square and circular photosensitive area shapes have their advantages due to the element pitch in the array structure. As the pitch decreases, the circular shape becomes more optimal due to the growing influence of the perimeter, especially in the planar version where the lateral part of the *p–n* junction leads to the higher dark current compared to the mesa version. On the other hand, since elements are packed densely in the array, the circular shape gives rise to a significant area requiring surface passivation to reduce the surface recombination rate and increase the photoresponse. The selected series of pitches (10, 12, 15, and 20 μm) will allow identifying major trends in photoelectric parameters of array photosensors.

Figure 3 shows corner fragments of combined top-layer topologies of readout LSI circuits sized 1280×1024 and featuring the 12 μm pitch, including 4 rows of common contacts and at least two unscanned rows serving as "guard rings" to suppress edge effects caused by lateral diffusion of minority charge carriers and topologies of array photosensors for pitches of 10 μm (*a*), 12 μm (*b*), 15 μm (*c*), and 20 μm (*d*) with square and circular shapes of photosensitive elements. It can be seen that periods consisting of 6, 5, 4, and 3 array photosensors correspond to the pitches of 10, 12, 15, and 20 μm and are equal to the period of 5 LSI circuit elements with the 12 μm pitch. Figure 3a shows the most optimal combination for square and circular areas of In micro-contacts sized 5×5 elements, within which the primary photoelectric parameters of array photodetectors for the 10 μm pitch can be obtained. Here, every sixth array photodetector shall be fabricated without In micro-contacts and be connected via CrNi traces to the common contact on the periphery, thus forming a grid of closed *p–n* junctions to prevent edge effects caused by lateral diffusion of minority charge carriers. To ensure the most optimal contact and avoid closing for the 15 μm pitch of array photosensors (Fig. 3*c*), a 1 μm offset from the mesa center diagonally towards the center of each element in the group of 4×4 array photosensors has been defined. Similarly, for the 20 μm pitch of array photosensors (Fig. 3*d*), a 2 μm offset from the mesa center away from the center of each edge element in the group of 3×3 array photosensors has been defined.

The variable topological parameters of elements (square, circle, pitch) within a single array were implemented as strips along longer sides of chips to enable wedge-type thinning along these strips after hybridization with the readout LSI circuit for measuring the dependencies of photoelectric characteristics on thickness. These dependencies allow deriving such parameters as the volume diffusion length, identifying dark current generation mechanisms, and gaining the information about recombination at the interface of the epitaxial growth/substrate, etc. To ensure precise thickness measurement via interference in each element, element-based measurement of spectral characteristics is proposed [9].

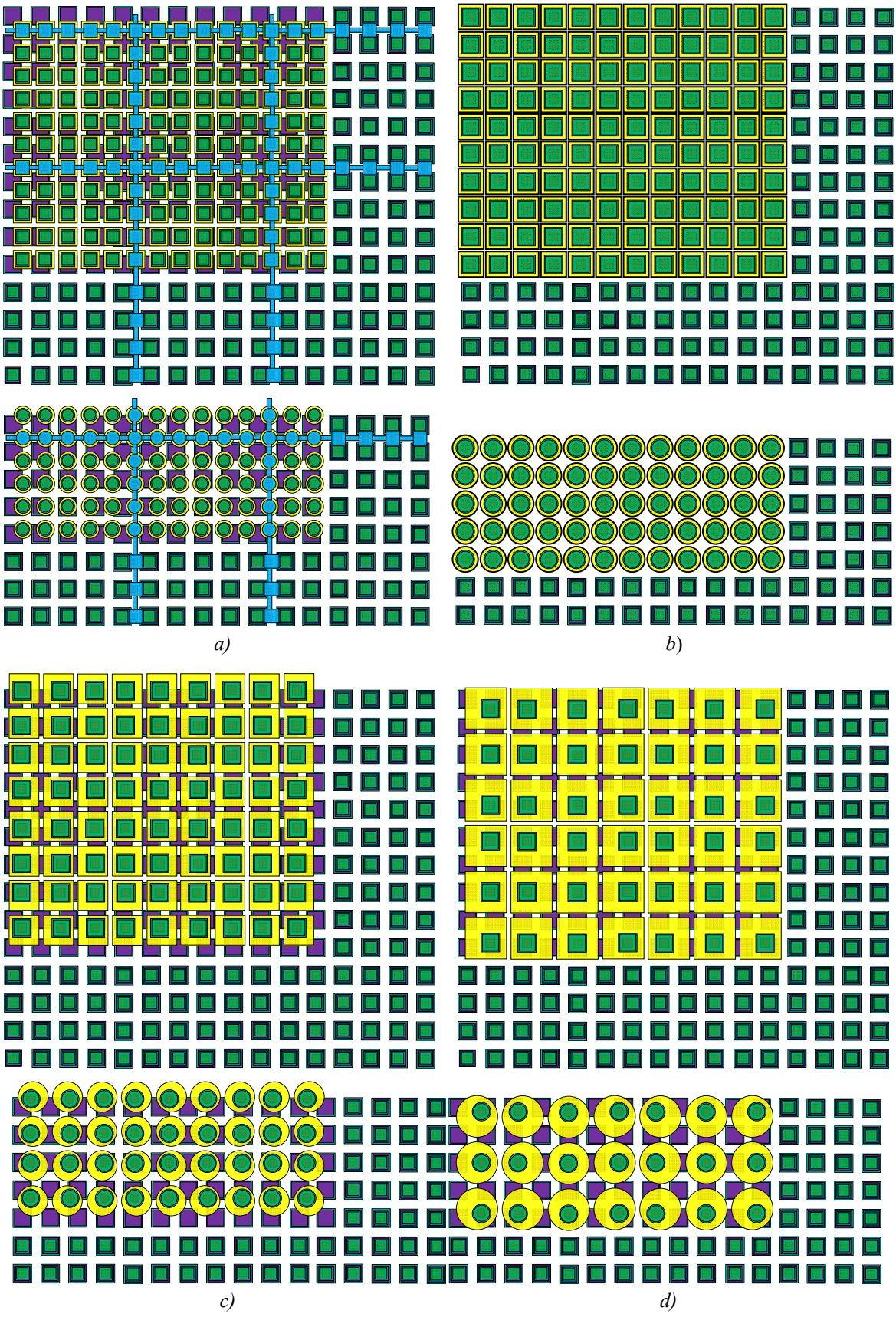

Fig. 3. Images of angular fragments of combined top-layer topologies of the readout LSI circuit sized 1280×1024 elements and featuring the 12 μm pitch (CrNi – □, In – ■) and topologies of array photosensors sized 1536×1228 elements and featuring the 10 μm pitch (a), 1280×1024 elements and 12 μm pitch (b), 1024×819 elements and 15 μm pitch (c), and 768×614 elements and 20 μm pitch (d) for square (top) and circular (bottom) topologies

Wedge Test

Study of the interconnection between photoelectric elements and detector photoresponse as a function of photosensitive region thickness is of particular significance. The photoelectric interconnection between elements is known to decrease as the photosensitive region thickness is reduced, but the reduction in photocarrier numbers leads to lower photoresponse and, consequently, reduced sensitivity of the photodetector. It is possible determine the optimal ration between thickness and interconnection of the elements by studying distribution of photosensors' sensitivity across arrays thinned in the wedge-like manner using silicon scanning masks [7, 8]. The front side of the photosensor array featuring variable thickness and not provided without antireflection coating shall be pre-treated with argon ions to eliminate surface recombination [3, 4]. Figure 4 shows example images of an output signal of an epitaxial pattern with a 4-μm thick absorbing layer grown on a heavily doped indium antimonide substrate with orientation (100), with implanted *p–n* junctions sized 640×512 and featuring the 15 μm pitch, before and after left-to-right thinning in wedge-like manner from ~0 to ~14 μm, without antireflection coating and after being treated with Ar^+ ions.

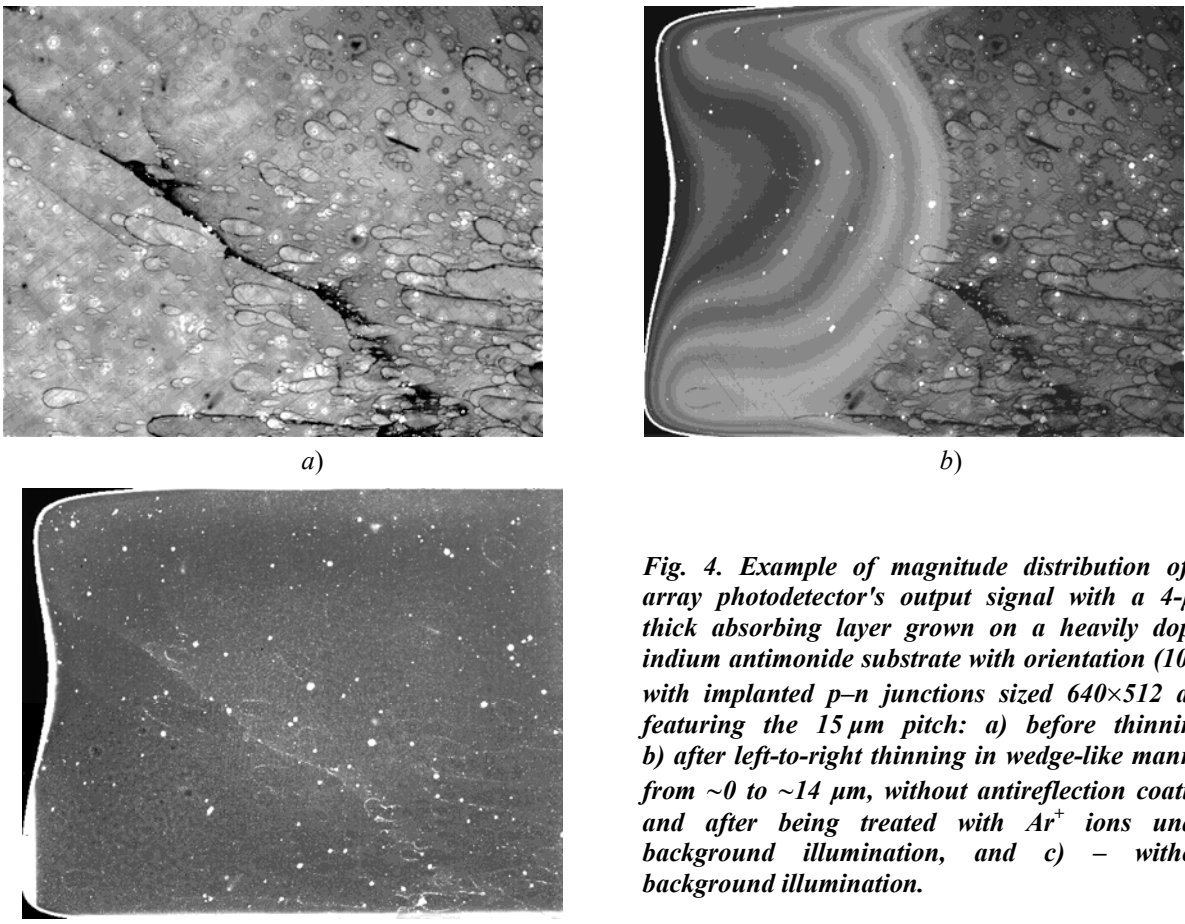

a) *b*)

c)

Fig. 4. Example of magnitude distribution of a array photodetector's output signal with a 4-μm thick absorbing layer grown on a heavily doped indium antimonide substrate with orientation (100), with implanted p–n junctions sized 640×512 and featuring the 15 μm pitch: a) before thinning; b) after left-to-right thinning in wedge-like manner from ~0 to ~14 μm, without antireflection coating and after being treated with Ar^+ ions under background illumination, and c) – without background illumination.

Figure 4a shows magnitude distribution of an output signal of the epitaxial pattern before thinning under background illumination. Bright areas correspond to *p–n* junction leakage, while dark areas correspond to recombination in the *n*-region. After thinning in the wedge-like manner from the substrate side, the epitaxial growth interface can be clearly seen in the photoelectric image obtained in background mode (Fig. 4*b*), with thickness resolution of ~20 nm limited by the 15 μm array pitch and the wedge angle. Four interference bands can be distinctly seen in the left part of the image, these bands corresponding to the wedge-shaped epitaxial layer thickness

from 0 to 4 μm after thinning after at the array photodetector's absorption wavelength of 3.6÷5 μm and complete removal of the substrate. Dark areas remain in the right part of the image and correspond primarily to recombination at the substrate/epitaxial layer interface. Thus, we can observe a sharp substrate/epitaxial layer interface. Interestingly, some recombination areas extend through the epitaxial layer growth depth down to ~1 μm. At the same time, most recombination areas cannot be observed in the grown epitaxial layer, that is defective areas occurring at the growth interface are "healed". On the contrary, in the dark current image (Fig. 4*b*), not only the growth interface cannot be seen, but also the dark current does not depend on the epitaxial layer thickness. This indicates the predominance of the generation-recombination mechanism of dark current formation in the space charge area directly within the *p–n* junction over the diffusion mechanism of dark current generation in the epitaxial structure [10].

Conclusions

InSb-based test array structures based have been developed for hybridization with readout LSI circuit sized 1280×1024 and featuring the 12 μm pitch in order to study the topology of array photosensors of the array photodetector's primary photoelectric characteristics within a single large-size array.

Some versions of test structures for array photosensors and topologies for silicon scanning masks with a universal pitch exceeding the diffusion length of minority charge carriers in InSb have been proposed for the purpose of measuring the interconnection.

A structure for a mask work set has been developed that features the area distribution of array test structures to enable wedge-like thinning in order to produce ultra-thin structures with controlled thickness across the area for better strength and minimum interconnection. The feasibility of implementing the proposed test structures has been analyzed.

The change in the output signal distribution characteristics was studied in the image after wedge-like thinning of an epitaxial sample grown on a heavily doped indium antimonide substrate (sized 640×512, 15 μm pitch):

– defective areas (with enhanced recombination) formed at the growth interface were proved to be "healing" experimentally;

– the penetration depth of defective areas into the epitaxial layer was approximately 1 μm.

REFERENCES

1. Gershon G., Albo A., Eylon M., Cohen O., Calahorra Z., Brumer M., Nitzani M., Avnon E., Aghion Y., Kogan I., Ilan E., Tuito A., Ben Ezra M. and Shkedy L., SemiConductor Devices (SCD), Israel. «Large Format InSb Infrared Detector with 10 μm Pixels», OPTRO-2014-2931891.

2. Lopukhin A. A., Boltar K. O., Grishina A. N. and Shishigin S. E., Usp. Prikl. Fiz. (Advances in Applied Physics) **10** (1), 14–22 (2022) [in Russian].

3. Lopukhin A. A., Permikina E. V., Boltar K. O. and Grishina A. N., Usp. Prikl. Fiz. (Advances in Applied Physics) **11** (5), 421–432 (2023) [in Russian].

4. Lopukhin A. A., Vlasov P. V., Grishina A. N., Permikina E. V. and Shishigin S. E. Method for manufacturing thinned multi-element photodetector based on indium antimonide with improved uniformity and increased mechanical strength. Patent No. RU 2811379 C1 (RF). 2024.

5. Lopukhin A. A., Permikina E. V., Taubes E. V., Shishigin S. E., Mirofyanchenko A. E. and Mirofyanchenko E. V., Usp. Prikl. Fiz. (Advances in Applied Physics) **13** (1), 21–29 (2025) [in Russian].

6. Lopukhin A. A., Permikina E. V., Lavrentev N. A., Taubes E. V., Shishigin S. E., Mirofyanchenko A. E. and Mirofyanchenko E. V. Method of measuring dark current on test matrix structures with variable topology for determining passivation efficiency of large-format matrix photodetectors with small pitch. Patent No. RU 2841177 C1 (RF). 2025.

7. Lopukhin A. A., Boltar K. O., Akimov V. M. and Arbuzov M. A., Applied Physics, No. 5, 44–52 (2021) [in Russian].

8. Boltar K. O., Akimov V. M., Arbuzov M. A. and Lopukhin A. A. Method for obtaining the sensitivity distribution over the matrix photodetector pixel area. Patent No. RU 2783220 C1 (RF). 2022.

9. Davletshin R. V., Lazarev P. S., Nikonov A. V. and Korneeva M. D., Applied Physics, No. 4, 63–66 (2016) [in Russian].

10. Chishko V. F., Kasatkin I. L., Burlakov I. D., Lopukhin A. A., Ponomarenko V. P., Filachev A. M., Borodin D. V., Osipov Yu. V., Karpov V. V. and Kroshin A. M., Applied Physics, No. 2, 64–68 (2007) [in Russian].

About authors

Lopukhin Alexey Alekseyevich, Cand. Sci. (Eng.), Head of Laboratory, RD&P Center ORION, JSC (111538, Russia, Moscow, 9 Kosinskaya st.). E-mail: alexmatr0@mail.ru SPIN code: 7352-7713, AuthorID: 221931

Permikina Elena Vyacheslavovna, Lead Engineer, RD&P Center ORION, JSC (111538, Russia, Moscow, 9 Kosinskaya st.). SPIN code: 4231-5554, AuthorID: 780646

Barysheva Ksenia Vladimirovna, Engineer 1st Category, RD&P Center ORION, JSC (111538, Russia, Moscow, 9 Kosinskaya st.).

Lopatin Vadim Vladimirovich, Dr. Sci. (Eng.), Project Manager Foundation for Advanced Research (121059, Russia, Moscow, 22/3 Berezhkovskaya Emb.). AuthorID: 370192

PHOTOELECTRONICS

UDC 538.915 PACS: 85.60.-q
EDN: JVZIUO

Radiation resistance of light-emitting structures with Ge/Si nanoislands on SOI substrate

Yu. A. Kabalnov* and M. M. Ivanova

FSUE "RFNC-VNIIEF", Nizhny Novgorod Region, Sarov, 607188 Russia
** E-mail: Kabalnov@niiis.nnov.ru*

Received 22.07.2025; revised 18.08.2025; accepted 20.10.2025

Theoretical and experimental research results are presented to demonstrate the impact of γ-neutron radiation on the parameters of light-emitting structures with an array of Ge(Si) nanoislands grown by methods of molecular beam epitaxy on SOI substrates. These structures showed a high level of resistance to the impact of γ-neutron radiation comparable with resistance level of structures with Ge(Si) nanoislands on Si(001) substrates. Reduction of luminescence intensity of these structures coincides with theoretical estimate of radiation defects influence level. Simulation results and experimental data show that the Ge(Si) nanoislands array structures affect the radiation resistance of LEDs to the greatest extent.

Keywords: light-emitting structures; Ge(Si) nanoislands arrays; SOI structures; radiation resistance; γ-neutron radiation.

DOI: 10.51368/2949-561X-2025-5-27-35

Introduction

Silicon-on-insulator (SOI) structures, along with Silicon-on-sapphire (SOS) structures, are widely used as base materials for creating radiation-hardened microelectronic hardware components. A buried dielectric layer acts as a barrier that reduced the impact of radiation-induced defects of a substrate on the active regions of semiconductor devices and integrated circuits. SOI structures also have special properties that are of interest for developing optoelectronic devices [1, 2]. The difference in refractive indices between Si and SiO_2 (3.5 and 1.45, respectively) simplifies the task of creating waveguide couplings between planar geometry elements made on SOI structures. The light wave field concentrated between the buried dielectric and the heterostructure surface develops maximum intensity within the silicon layer. Heterostructures exhibit intensity-enhancing effects due to vertical Fabry-Perot type resonances caused by interference of waves reflected from the surface-Si and Si-SiO_2 interfaces [3]. In the future, SOI structures can be considered as a basis for nanostructured integrated optics with devices for generation, amplification, and detection of optical signals, with waveguides and couplers as passive elements, while still being compatible with standard silicon technology.

The use of heteroepitaxial structures with Ge(Si) nanoislands (quantum dots) allows expanding spectral characteristics of silicon-based optical elements into the near- and mid-infrared ranges and overlapping the communication wavelength band of 1.3–1.55 μm, which corresponds to the optical fiber transparency window. Spatial confinement of charge carriers in all three dimensions reduces the sensitivity of radiative properties of nanoisland structures to radiation-induced defects as compared to structures with lower degrees of confinement, such as bulk silicon and structures incorporating quantum wells [4]. Although Ge(Si) nanoisland structures feature

photoluminescence (PL) and electroluminescence (EL) signals up to the room temperature, the low radiative recombination efficiency of charge carriers hinders their commercialization. According to the research results [5], one of the most promising methods to enhance the radiation intensity of Ge(Si) nanoisland structures is to integrate an active radiating medium into various types of optical resonators. The possibility of integrating Ge(Si) nanoisland structures into resonator structures is enabled by the use of SOI substrates. A positive effect of increased emission intensity is observed when using resonators such as microdisks, photonic crystals, plasmonic, and dielectric microresonators [3, 5, 6]. Radiative recombination efficiency can also be increased by using waveguide structures made on SOI substrates and having optimized parameters and design. In this case, the process of forming Ge(Si) nanoislands according to the Stranski-Krastanow mechanism is integrated into the waveguide structure fabrication route. The application of these methods for enhancing the photoresponse enables a realistic way to develop effective photon sources based on Ge(Si) nanoisland structures.

Since the use of SOI structures for integrated optics devices has great potential, ensuring the radiation hardness of light-emitting structures grown on SOI substrates is a relevant research issue. The studies performed to research the impact of ionizing radiation on the photoluminescence and electroluminescence of heteroepitaxial structures with Ge(Si) nanoislands grown by molecular beam epitaxy on bulk silicon substrates – Si(001) [4, 7] have proved their potentially high radiation hardness. Self-generation processes of Ge(Si) nanoislands are stimulated by accumulation of elastic stress in the epitaxial layers due to the significant mismatch of lattice parameters between the substrate and the film. When the growing layer thickness exceeds critical values, the elastic stress relaxes due to nanoislands growing according to the Stranski-Krastanow mechanism. The elastic stress field of the buried dielectric layer in SOI structures, along with the standard thickness of the submicron silicon epitaxial film for integrated circuits, can have a potential influence on self-generation processes of Ge(Si) nanoislands, thus increasing the concentration of structural defects and reducing the radiation hardness of devices. This paper presents the findings of studying the impact of pulsed γ-neutron radiation on parameters of light-emitting structures with Ge(Si) nanoisland arrays grown on SOI substrates. These findings are given in comparison with the findings for radiation of similar structures on bulk silicon substrates.

Experiment procedure

LED samples were grown by molecular beam epitaxy (MBE) using Balzers UMS-500 system. Silicon-on-insulator (SOI) structures with (001) orientation fabricated by the bonding method were used as substrates. The thickness of the surface silicon layer was 200 nm, and the buried dielectric layer was 1 μm. On the substrate surface, at the temperature of 600 °C a lower contact layer Si of p^+- conductivity type of 30 nm thickness, boron-doped, with concentration of $\sim 5\times10^{18}$ cm^{-3} was deposited. The thickness of the lower silicon contact layer was increased compared to the bulk silicon structures to maintain low resistance of contacts. After that a 50 nm thick layer of undoped Si was grown. Ge(Si) nanoisland arrays were formed on the substrate surface at the temperature of 600 °C. The LED active region contained up to 20 layers of nanoislands separated by silicon barriers with thicknesses ranging from 15 to 20 nm, which ensured their vertical ordering. Islands formed during deposition of the Ge layer with a thickness of 6.5–8.5 monolayers (ML) (1 ML ~ 0.136 nm). Si and Ge layers were deposited from two electron-beam evaporators at growth rates of 0.1 nm/s and 0.02 nm/s, respectively. During growth the elastic stress fields of underlying layers influenced the sizes of nanoislands in the next layers. For better size uniformity of the islands, the Ge amount deposited was decreased by approximately ~0.1 ML for each next layer. Formation of LED structures was completed by depositing a 50 nm thick layer of undoped Si and a 200 nm thick n^+-type Si contact layer doped with antimony at the concentration of ~ 10^{19} cm^{-3}.

One of the significant challenges in the epitaxial growth of multilayer nanoisland structures on SOI substrates is monitoring the wafer surface temperature. The substrate temperature is a critical parameter that determines

the structure and properties of the nanoisland array. According to the MBE method, wafers are heated by a radiation source from the substrate side. Temperature is monitored from the substrate side too. A difference in the surface temperature between SOI structures and standard Si(001) substrates was observed at the same power supplied to the heater and identical thermocouple readings. The reason for this is a relatively thick (~ 1 μm) buried dielectric layer found in the SOI structures being studied. During formation of the structures the epitaxial growth conditions were calibrated to estimate the actual surface temperature of the SOI substrates as a function of the power supplied to the heater. This calibration was based on experimental data of the temperature dependence of Ge(Si) nanoisland parameters on bulk silicon substrates – Si(001) – and on SOI structures.

The morphology of the grown structures was studied using the atomic force microscopy (AFM) method under the atmospheric conditions with NT-MDT "Silver Pro" microscope (Russia). The crystal structure of epitaxial layers was studied by high-resolution transmission electron microscopy TEM) using JEOL JEM 2100F microscope. The film thickness during transition from the two-dimensional to the three-dimensional formation of nanoislands was determined by the reflected high-energy electron diffraction (RHEED). Photoluminescence (PL) spectra were measured using DA3-36 Fourier transform spectrometer. PL signal was excited by Nd:YAG laser with the wavelength of $\lambda = 532$ nm. Electroluminescence (EL) and PL spectra were recorded using cooled Ge and InSb photodetectors. The samples under study were exposed to the pulsed γ-neutron irradiation. A pulsed reactor with a characteristic neutron energy of ~1 MeV and a fluence of up to 10^{15} n/cm^2 was used as a neutron source. The exposure dose of γ-radiation was ~ 400 kR.

Experimental results and their discussion

Conditions to ensure the radiation hardness, namely the localization of charge carriers, are determined by the system of Ge(Si) nanoislands formed in the light-emitting structures. Island characteristics (size, shape, composition, elastic stress) depend on the growth conditions [8]. Self-generation processes are influenced by such parameters as substrate temperature, deposition rate, surface morphology, rates of surface and bulk diffusion of components, etc. During epitaxial growth, the shape of the Ge(Si) nanoislands is observed to be transforming. After the layer-by-layer growth changes over to the three-dimensional growth, a system of Ge(Si) nanoislands with a rectangular base (hut islands) and pyramidal islands forms, which then transforms into a system of uniform dome-shaped islands (dome islands) ordered in the substrate plane [9]. This changeover is favorable in terms of energy because the elastic strain energy for dome-shaped islands is lower than for islands of other shapes. Dome-shaped Ge(Si) islands faceted by (105) and (113) planes do not have a highly developed surface. Reflecting boundaries of the nanoislands along with the low surface recombination contribute to the charge carrier localization. Dome islands exhibit the deepest potential well for holes. Spatially ordered arrays of Ge(Si) dome islands form with high density, occupy the maximum substrate area, and provide the highest efficiency for parameters of light-emitting structures due to high localization of charges in the potential wells.

Ge(Si) nanoisland arrays were grown under optimal conditions to achieve efficient parameters of light-emitting structures. The substrate temperature was one of the most critical parameters during formation of the Ge(Si) nanoisland system. It was established that when heated in the temperature range from 550 °C to 650 °C, the surface temperature of SOI structures was 40 °C higher than that of bulk silicon wafers. The optimal wafer surface temperature for the characteristic array of dome islands to form is 600 °C. Figure 1*a* shows an AFM image of an SOI structure with the formed array of Ge(Si) nanoislands. The morphology of Ge(Si) nanoislands grown on SOI structures at the optimal substrate surface temperature of ~ 600 °C is similar to the morphology of nanoislands grown on bulk Si(001). The obtained typical morphological parameter values exhibit a small spread in sizes of dome islands. The surface density $N \sim 5{,}0\times10^9$ cm^{-2}, average island height h ~ 15 nm, average lateral dimensions D less than 100 nm with the spread of ~15 % (determined at

the 0.1h level from the Ge wetting layer surface), and the average germanium fraction in Ge_xSi_{1-x} ($x = 0.54$) are close to the parameter values of nanoislands grown on Si(001). The similarity in morphologies of nanoislands grown on SOI and Si(001) structures facilitates the comparative analysis of radiation effects under exposure to γ-neutron radiation.

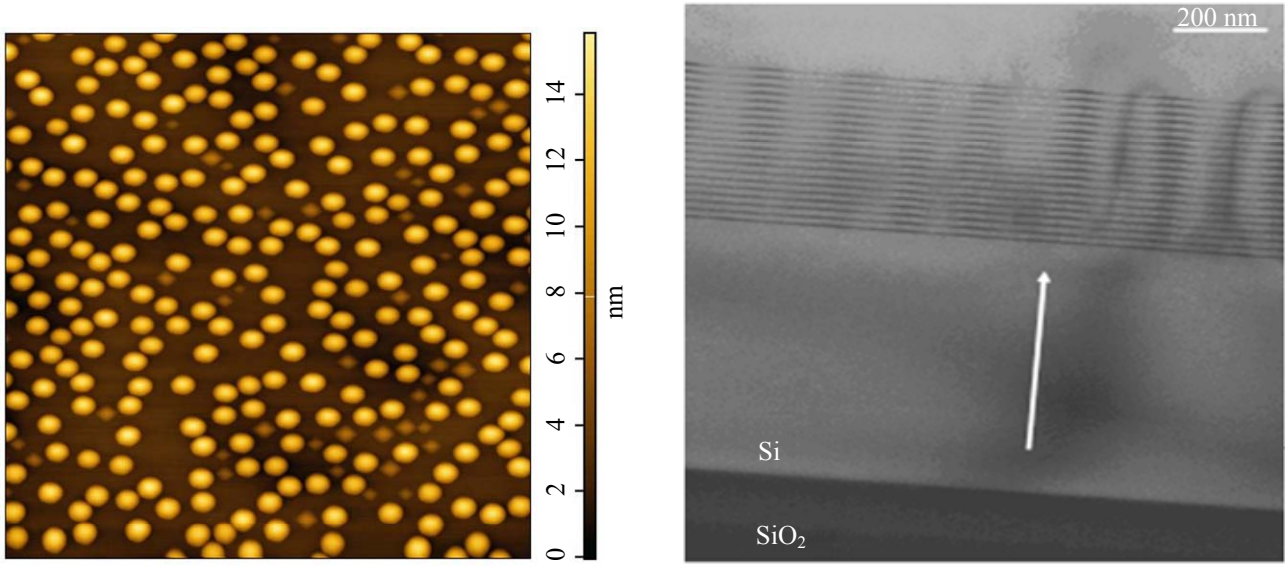

a) *b*)

Fig. 1. AFM image of the SOI structure surface with the self-generated array of dome-shaped Ge(Si) nanoislands (a) and TEM image of the multilayer structure with Ge(Si) nanoislands grown on the SOI substrate (b)

The TEM image (Fig. 1*b*) shows the multilayer structure of Ge(Si) nanoislands in the active region of the light-emitting *p–i–n* diode formed on the SOI substrate. The vertical arrangement of the layer structure is caused by the influence of the elastic strain field from the underlying Ge(Si) nanoislands. The layer-by-layer correlation of the island array depends on the parameters of the Si spacer layers. The optimal thickness of these spacer layers ranges from 15 to 20 nm. Studies of multilayer structures with silicon spacer layer thicknesses between 15 and 20 nm have also shown a significantly lower concentration of defective regions compared to structures with Si layer thicknesses greater than 25 nm. When the spacer layer thickness is comparable to the size of the Ge(Si) nanoislands in the growth direction, the silicon deformation takes the form of tension between adjacent islands, which results in formation of a deep (up to 100 meV) potential well for electrons at the Ge/Si interface. The formation of this potential well causes charge carriers to concentrate near the nanoislands and contributes to the increased electroluminescence intensity of the structures. Since a visible interface between the initial silicon layer of the SOI structure and the MBE-grown Si buffer layer cannot be seen in the image, it proves the wafer surface preparation methods used prior to epitaxy to be effective.

To measure parameters of light-emitting *p–i–n* diodes with a Ge(Si) nanoisland array in the active region, mesastructures sized 1×1 mm and 1×0.5 mm were formed using plasma chemical etching. The upper contact to the n^+-Si layer was made as a metallization grid to increase the free surface area to enable light emission. The lower contact to the p^+-silicon region surrounded the mesastructure along its perimeter. Gold with a Ti sublayer was used for metallization. Figure 2*a* compares the photoluminescence spectra of multilayer structures grown on Si(001) and SOI substrates and similar Ge(Si) nanoisland arrays.

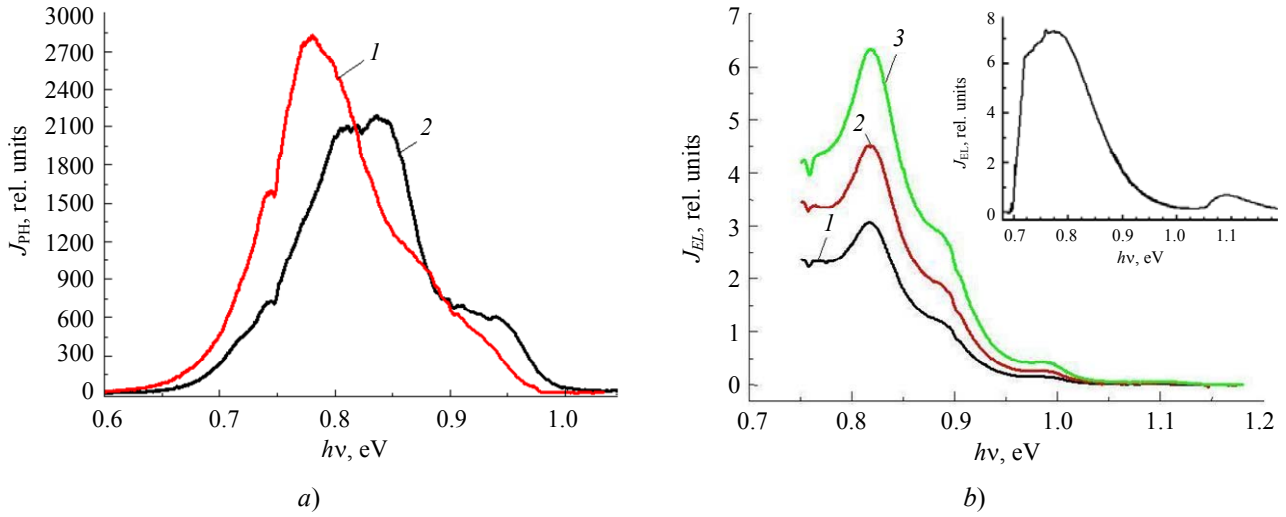

Fig. 2. PL spectra of structures formed on Si(001) (1) and SOI (2) substrates with Ge(Si) nanoisland arrays (a), and EL spectra of structures with Ge(Si) nanoisland arrays on SOI substrates at different pump currents (1 – 150 mA, 2 – 200 mA, 3 – 250 mA) (b); the inset shows the EL spectrum of structures with Ge(Si) arrays on Si(001) substrates. Spectra were measured at temperatures of 77 K (a) and 300 K (b)

The PL intensity J_{PL} is given in terms of relative units. Both the Si(001) and SOI structures exhibit broad PL peaks (Fig. 2*a*) associated with the radiative recombination of charge carriers localized in the Ge(Si) nanoisland regions. A slight shift of intensity maxima is observed within the quantum energy range of $h\nu \sim 0.7–1.0$ eV ($\lambda \sim 1.3–1.7$ μm). The intensity of luminescent responses in both spectra is comparable, suggesting similar morphology of the Ge(Si) nanoislands. The buried dielectric seems not to have significant effect on the nanoisland morphology and, consequently, the radiative properties of the diodes, while the crystalline quality of the active regions in SOI wafers made by the bonding method is not inferior to that of bulk silicon. However, the spectral characteristics differ in nature. The spectra of light-emitting structures formed on SOI substrates contain at least two maxima. Specific features of structures on SOI substrates result in Fabry-Perot vertical resonances caused by interference of waves reflected from the Si-surface and Si-buried SiO_2 interfaces.

Figure 2*b* shows the electroluminescence spectra of multilayer LED structures grown on SOI substrates at different pump currents. The spectra were measured at the room temperature. The EL intensity J_{EL} is given in relative units. The EL signal was detected from the surface of the LED structures. The sample surface was fixed perpendicular to the optical axis of the measurement system during measurements. As can be seen in the figure, the luminescence intensity changes depending on the pump current value, but the spectral shape remains unchanged. The intensity maxima can still be observed on the curve. The main emission peak corresponds to the wavelength of ~1.50 μm ($h\nu$ ~0.83 eV). The figure shows that the ratio of magnitudes and positions of the intensity maxima do not depend on the pump current. Therefore, these intensity maxima are not associated with various radiation processes within the structure being studied but are determined by wave interference phenomena.

The studies of the EL intensity of diodes on SOI substrates vs. the observation angle showed that the nature of radiation spectra does not change with the angle varying. As the angle relative to the normal of the structure surface was changed (range from 0 to 90°), the peak radiation wavelength changed within the range of $\lambda \sim 1.45–1.60$ μm, while the EL intensity magnitude remained practically unchanged. The studies of the angular dependence of the EL signal allow attributing the observed spectral maxima to wave interference within the active region of the structure. The EL signal maxima usually appear at the wavelengths, the optical paths of which contain an integer number of half-waves. Another distinctive feature of spectra of diodes on SOI structures is the absence of a signal associated with interband recombination of charge carrier in Si in the quantum energy region of 1.12 eV (inset, Fig. 2*b*). The signal from silicon for structures grown on Si(001) is largely

the result of radiative recombination of holes and non-equilibrium electrons within the substrate volume. In LED structures grown on SOI, the buried oxide prevents non-equilibrium carriers from diffusing into the substrate, which results in a reduced luminescent response from silicon.

The impact of a neutron flux on the semiconductor structure is accompanied by generation of primary radiation defects, such as Frenkel pairs. Array atoms are believed to be always displaced when they acquire energy greater than a certain threshold displacement energy. Although a large amount of energy is unlikely to be transferred to the displaced substrate atom, this event is probable practically in every collision cascade during radiation of silicon by neutrons. Consequently, radiation defects in the collision cascades of the radiated region are distributed non-uniformly, thus forming local disordered regions (DR) [10]. These DRs of radiation defects act as centers for non-radiative recombination and cause a reduction in luminescence intensity.

When considering the effects of γ-neutron radiation, the complex multilayer structure of LEDs with heterogeneous interfaces between different materials shall be taken into account. Using the "TRIM" program, the structure of radiation defects in SOI and SOS substrates was calculated under conditions of radiation with a fast neutron flux featuring the fluence of 5×10^{14} n/cm^2 and average energy of ~1 MeV. The calculation was performed for the condition of isotropic radiation. The calculations analyzed the silicon interfaces with the buried dielectric layer for SOI and SOS structures, as well as the metallization-silicon interfaces. Figure 3*a* shows the calculated the defect concentration (N) in the silicon layer for "SiO_2-Si", "Al_2O_3-Si", "Al-Si", "Au-Si", and "air-Si" structures as expressed in relative units versus the distance from the interface X. The calculations accounted for the fact that DRs in silicon can be formed by Al, Au, and O atoms, which are injected from the material adjacent to silicon upon interaction with neutrons. Since the interaction cross-section of fast neutrons with Au atoms is larger than with Si or Al atoms, their interaction with neutrons is much more efficient. The defect concentration at the Au-Si heterointerface in the near-surface silicon layer (~50 nm thick) is significantly higher than that in bulk silicon. The interface with sapphire is also effectively modified: the DR concentration is ~ 10^{15} cm^{-3} in the silicon layer adjacent to the interface, which is up to 150 nm thick. In SOI structures the interaction with oxygen does not lead to the increased concentration of radiation defects at the buried SiO_2-Si heterointerface as compared to bulk silicon.

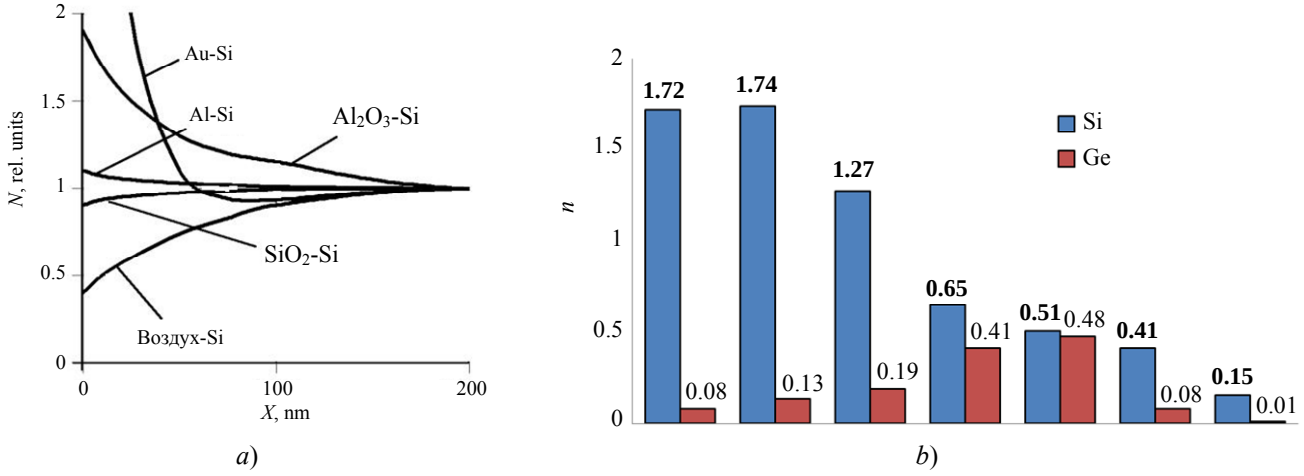

a) *b*)

Fig. 3. Defect concentration in the silicon layer N vs. the distance to the interface X in the heterostructures "l_2O_3-Si", "Al-Si", "Au-Si", "SiO_2-Si", and "air-Si" under exposure to the fast neutron flux (defect concentration in bulk silicon corresponds to 1) (a). Average number of subclusters in atomic displacement cascades n for Si and Ge atoms vs. subcluster size L (b)

Atomic displacement cascades initiated by primarily knocked-on Si and Ge atoms during radiation of the LED structure with the fast neutron flux (fluence 5×10^{14} n/cm^{2,} average energy ~1 MeV) were simulated using the Monte Carlo method based on the TRIM algorithm. The formation of DRs for the light-emitting structures with the Ge(Si) nanoisland array was calculated without accounting for disturbances at the buried SiO_2-Si interface, which are of local nature according to calculations (Fig. 3*a*). The displacement energy from crystal lattice sites for Si and Ge atoms was set to 20 eV. For the nanoisland array, the quantities of Si and Ge in the Ge_xSi_{1-x} solid solution ($x = 0.54$) were taken into account. The density of silicon was 2.33 g/cm^3, and the density of the Ge_xSi_{1-x} ~ 3.80 g/cm^3 solid solution was ~3.80 g/cm³. Primarily knocked-on Si and Ge atoms form atomic displacement cascades in the form of local defect clusters - subclusters. Figure 3*b* shows the results of simulating atomic displacement cascades for Si and Ge atoms. The average number of subclusters in atomic displacement cascades, n, as a function of subcluster size L is shown. DRs for primarily knocked-on Si and Ge atoms have different geometric sizes. Si atoms typically exhibit the formation of a large number of small subclusters (less than 10 nm) in the active region of the LEDs is characteristic, whereas Ge atoms - the formation of a small number of large subclusters (~40 nm). In the depletion region of *p–i–n* diodes, provided that Si spacer and buffer layers are present, the fraction of Ge atoms is much smaller than the fraction of silicon atoms. According to the calculation results, Ge atoms have a significantly smaller impact on the degradation of optoelectronic properties of heterostructures with Ge(Si) nanoislands as compared to Si atoms.

A theoretical assessment of DR influence on properties of light-emitting structures with Ge(Si) nanoislands grown on Si(001) substrates under γ-neutron radiation was conducted in reference [11]. The electric field of the DR space charge area reduces the concentration of carriers localized in the Ge(Si) nanoislands and, combined with non-radiative recombination processes at radiation defects, causes the luminescence intensity to decrease. The calculated fraction of nanoislands falling within the influence zone of the DR electric field for LED structures on Si(001) substrates was 40%. This calculation of the DR field was performed without accounting for primarily knocked-on Ge atoms. Considering the local nature of disturbances at the buried dielectric-silicon heterointerface (SiO_2-Si) (Fig. 3*a*) and the predominant influence of Si on the formation of atomic displacement cascades (Fig. 3*b*), the fraction of nanoislands within the influence zone of the DR field for heterostructures grown on Si(001) substrates shall be comparable to the fraction for structures on SOI substrates. This conclusion is supported by the experimental data. Figure 4 shows the PL spectra of structures with Ge(Si) nanoisland arrays grown on SOI substrates before and after γ-neutron radiation. The PL intensity J_{PL} is shown in terms of relative units.

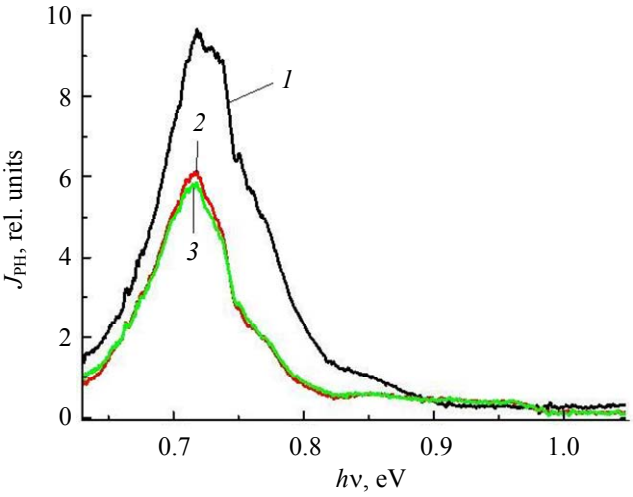

Fig. 4. PL spectra of structures with Ge(Si) nanoislands grown on SOI substrates before (1), after single (2), and after double (3) γ-neutron radiation with fluences of 2×10^{14} n/cm^2. Spectra were measured at the temperature of 77 K

The PL peaks of both radiated and non-radiated structures lie within the wavelength range of λ ~1.4–1.8 μm (quantum energy $h\nu$ ~0.65–0.85 eV). The wavelength of the maximum intensity of PL spectrum does not change after radiation. No decrease in luminescence intensity is observed after double radiation as compared to single irradiation, which is apparently due to the formation of stable clusters that act as sinks for radiation defects. The spectra shown in Fig. 4 indicate the 35 % reduction in PL signal intensity after exposure to fast neutrons, which is consistent with the

theoretical assessment of the DR influence on properties of structures incorporating Ge(Si) nanoislands and with the experimental data proving the reduction of luminescence intensity for structures grown on Si(001) substrates [11]. [11]. The simulation results and experimental data on the impact of γ-neutron irradiation demonstrate that the level of LED radiation hardness is primarily determined by the structure of the Ge(Si) nanoisland array. The use of SOI substrates does not degrade the radiation hardness of the structures.

Conclusion

The characteristics of light-emitting structures incorporating Ge(Si) nanoisland arrays and grown by MBE on SOI substrates were studied. Morphological parameters of Ge(Si) nanoislands on SOI structures (surface density, average height, lateral dimensions) were shown to approach the parameter values of nanoislands grown under similar conditions on Si(001) substrates. The PL spectra of light-emitting structures on SOI and Si(001) substrates are comparable in terms of luminescence response intensity but differ in their nature. The derived dependence of the EL intensity of light-emitting structures on SOI substrates on the pump current magnitude does not affect the spectra nature. Since the intensity maxima positions in the spectra do not depend on the pump current, their occurrence is not associated with various radiation processes within the structure being studied. The intensity maxima in the spectra of structures on SOI substrates are determined by Fabry-Perot type vertical resonances caused by the interference of waves reflected from the silicon interfaces with the surface and the buried dielectric layer.

The findings of the study of the impact of γ-neutron radiation on parameters of light-emitting structures are presented. When the impact of radiation on depletion regions of LEDs incorporating Ge(Si) nanoisland arrays grown on SOI substrates was studied, their complex multilayer structure with heterogeneous interfaces between different materials was considered. The structure of radiation defects in SOI substrates was calculated using the "TRIM" program. The interaction of neutrons with the oxygen in the buried dielectric layer was shown not to cause the defect level at the Si-SiO_2 heterointerface to exceed the defect level of the Si layer. Atomic displacement cascades initiated by primarily knocked-on Si and Ge atoms were simulated in the LED structures by the Monte Carlo method using the "TRIM" program. Si atoms were shown to have a significantly greater impact on the degradation of optoelectronic properties of heterostructures with Ge(Si) nanoislands as compared to Ge atoms. Considering the local nature of disturbances at the buried SiO_2-Si heterointerface, the fraction of nanoislands within the influence zone of radiation defects for structures grown on SOI substrates corresponds to the fraction of nanoislands on Si(001) substrates. The PL signal intensity for structures on SOI substrates is 35% lower after exposure to neutrons, which corresponds to the intensity reduction for structures on Si(001) substrates and aligns with the theoretical assessment of the influence of induced defects. The simulation results and experimental data demonstrate that the structure of the Ge(Si) nanoisland array has the greatest influence on the level of LED radiation hardness.

REFERENCES

1. Boucaud P., Li X., El Kurdi M. et al., Optical Materials, No. 27, 792–798 (2005).
2. Smagina Zh. V., Zinovyev V. A., Stepikhova M. V. et al., Physics and Semiconductor Technology **55** (12), 1210–1215 (2021).
3. Yakimov A. I., Kirienko V. V., Bloshkin A. A. et al., Physics and Semiconductor Technology **58** (7), 386–392 (2024).
4. Novikov A. V., Yablosnkiy A. N., Platonov V. V. et al., Physics and Semiconductor Technology **44** (3), 346–351 (2010).
5. Smagina Zh. V., Novikov A. V., Stepikhova M. V. et al., Physics and Semiconductor Technology **54** (8), 708–715 (2020).
6. Zinovyev V. A., Smagina Zh. V., Zinovyev A. F. et al., Physics and Semiconductor Technology **58** (5), 238–241 (2024).

7. Krasilnikov Z. F., Kudryavtsev K. E., Kachemtsev A. N. et al., Physics and Semiconductor Technology **45** (2), 230–234 (2011).
8. Pchelyakov O. P., Bolkhovityanov Yu. B., Dvurechenskiy A. V. et al., Physics and Semiconductor Technology **34** (11), 1281–1299 (2000).
9. Vostokov N. V., Gusev S. A., Dolgov I. V. et al., Physics and Semiconductor Technology **34** (1), 8–12 (2000).
10. Kabalnov Yu. A., Kachemtsev A. N. and Obolenskiy S. V., Problems of atomic science and technology, No. 3, 12–18 (2019).
11. Ivanova M. M., Kabalnov Yu. A., Kachemtsev A. N. and Skupov A. V., Usp. Prikl. Fiz. (Advances in Applied Physics) **13** (3), 201–208 (2025) [in Russian].

About authors

Kabalnov Yuri Arkadyevich, Cand. Sci. (Eng.), Leading Research Scientist, FSUE "RFNC-VNIIEF" (607188, Russia, Sarov, Nizhny Novgorod Region, 37 Prospect Mira). E-mail: Kabalnov@niiis.nnov.ru E-mail: Kabalnov@niiis.nnov.ru

Ivanova Maria Mikhailovna, Lead Engineer, FSUE "RFNC-VNIIEF" (607188, Russia, Sarov, Nizhny Novgorod Region, 37 Prospect Mira). SPIN code: 8630-2864, AuthorID: 1210282

PHOTOELECTRONICS

UDC 621.315.592 PACS: 81.15.Hi
EDN: MVRVRN

The calculation of free charge carrier intrinsic concentration values in indium antimonide

A. G. Belov[1], R. Yu. Kozlov[1,2], E. O. Zhuravlev[1,2,*], E. V. Molodtsova[1], N. G. Khikheev[1], N. A. Sarkisov[3], M. A. Pankov[3] and V. B. Kulikov[4]

[1] *Giredmet, JSC, Moscow, 111524 Russia*
[*] *E-mail: EOZhuravlev@yandex.ru*
[2] *National University of Science and Technology MISiS, Moscow, 119049 Russia*
[3] *RD&P Center ORION, JSC, Moscow, 111538 Russia*
[4] *Joint Stock Company "Central Scientific-Research Institute "Cyclone", Moscow, 107497 Russia*

Received 30.09.2025; revised 16.10.2025; accepted 20.10.2025

The calculations of free charge carrier intrinsic concentration values, n_i, in indium antimonide for T = 295 K and T = 77 K have been made, taking into account the nonparabolisity of conduction band. It was shown, that $n_{i_{295}} = (2.14 \pm 0.01)\times10^{16}$ cm^{-3} and $n_{i_{77}} = (2.47 \pm 0.01)\times10^{9}$ cm^{-3}. The comparison of $n\times p_h$ product and n_i^2-values has been made, and they were shown to differ from each other. It has been suggested, that these differences are due to conduction band nonparabolisity. Literary data have been analyzed (the results of experiments to determine n_i-values in wide temperature range). The results of calculation are shown to be in satisfactory agreement with experimental data. It is suggested that results obtained will be used in the future for optimization of technological processes of InSb single crystal growth and doping.

Keywords: indium antimonide; intrinsic free charge carrier concentration.

DOI: 10.51368/2949-561X-2025-5-36-42

Introduction

The intrinsic free charge carrier concentration (IFCCC) is a fundamental characteristic of any semiconductor material and one of the key parameters used in calculating distributions of electrons and holes. It is impossible to correctly determine dopant masses and growth conditions for semiconductor materials without information on IFCCC.

As for indium antimonide, the literature provides the IFCCC values pertaining to the temperature range of $T \geq 150$ K, while information on the IFCCC values at the temperatures close to the boiling point of liquid nitrogen is hardly available.

We have attempted to fill this gap. The aim of this paper is to calculate the IFCCC values for indium antimonide at $T = 295$ K and $T = 77$ K, as well as to analyze literature data concerning methods for determining IFCCC values. The results obtained are expected to be used to optimize processes for producing and doping InSb single crystals.

Theoretical calculations

The band structure of indium antimonide is shown in Fig. 1 [1].

According to the formula (see summary [1]) for calculating the band gap width vs. the temperature in the temperature range of $(0 < T < 300$ K):

$$E_g = 0.24 - 6\times10^{-4}\times T^2/(T + 500), \text{ eV}; \quad (1)$$

we get $(E_g)_{295} = 0.17$ eV; $(E_g)_{77} = 0.23$ eV.

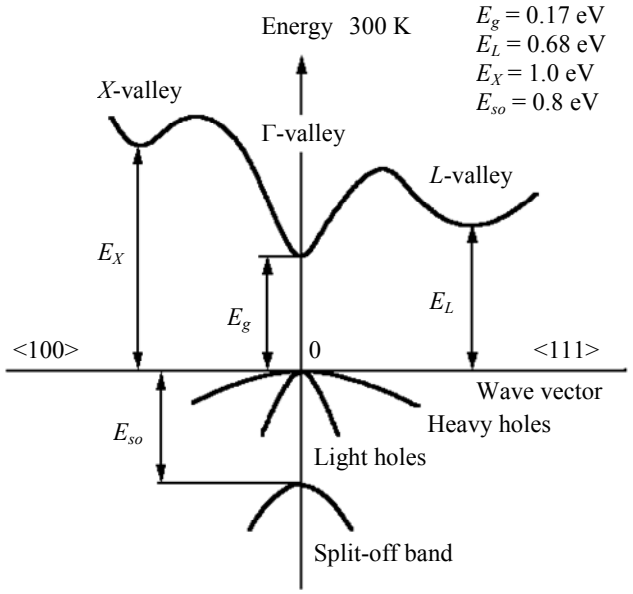

Fig. 1. Band structure of InSb

The following relations [2] are applicable to the concentrations of electrons (n), light (p_{L}) and heavy (p_{H}) holes:

$$n = \frac{\sqrt{3}}{2\sqrt{2}\pi^2} \times \frac{\left(kTE_g\right)^{\frac{3}{2}}}{P_{cv}^3} \times {}^0L_0{}^{\frac{3}{2}}(\eta,\beta); \qquad (2)$$

$$p_{\text{L}} = \frac{\sqrt{3}}{2\sqrt{2}\pi^2} \times \frac{\left(kTE_g\right)^{\frac{3}{2}}}{P_{cv}^3} \times {}^0L_0{}^{\frac{3}{2}}\left[\left(-\frac{1}{\beta}-\eta\right),\beta\right]; \qquad (3)$$

$$p_{\text{H}} = \frac{8\pi}{3h^3} \times \left(2m_{p_{\text{H}}}kT\right)^{\frac{3}{2}} \times F_{\frac{3}{2}}\left(-\frac{1}{\beta}-\eta\right), \qquad (4)$$

where $\eta = \dfrac{E_p}{kt}$ is reduced Fermi energy level; $\beta = \dfrac{kT}{E_g}$ is nonparabolicity parameter of the conduction band and light holes in Kane model [3]:

Here, E_g is the semiconductor band gap width; $k = 1.38\times10^{-16}$ erg/K is Boltzmann's constant; $\hbar = \dfrac{h}{2\pi}$, where $h = 6,.62\times10^{-27}$ erg·s is Planck's constant; $m_{p_{\text{H}}} = 0.43\ m_0$ [1] is the effective mass of heavy holes ($m_0 = 9.11\times10^{-28}$ g is the free electron mass); $P_{cv} = 8.7\times10^{-8}$ eV·cm [4] is the array element for the interaction between the light-hole valence band and conduction band (considered to be independent of the temperature and identical for all A_3B_5 compounds).

The bottom of the conduction band is taken as the zero energy reference; the positive direction is upward; our concern is values of $\eta \le 0$.

Formulas (2) and (3) use two-parameter Fermi integrals:

$${}^mL_k^n(\eta,\beta) = \int_0^\infty \left(-\frac{\partial f_0}{\partial x}\right) \frac{x^m\left(x+\beta x^2\right)^n}{\left(1+2\beta x\right)^k} dx \qquad (5)$$

The two-parameter integral ${}^0L_0^{\frac{3}{2}}(\eta,\beta)$ transforms into the one-parameter integral $F_{\frac{3}{2}}(\eta)$ (4) when $\beta \to 0$, that is, when the nonparabolicity of the band can be neglected.

$$F_{\frac{3}{2}}(\eta) = \int_0^\infty \left(-\frac{\partial f_0}{\partial x}\right) x^{\frac{3}{2}} dx, \qquad (6)$$

where

$$f_0(x,\eta) = \left[1+\exp\left(x-\eta\right)\right]^{-1} \qquad (7)$$

The algorithm for determining IFCCC is as follows.

1. A specific value of parameter η is selected, and concentrations of electrons, light holes, and heavy holes are calculated using formulas (2), (3), and (4).

2. A different value of the mentioned parameter is selected, and the calculation procedure is repeated (and so on).

3. Dependencies of free charge carrier concentrations vs. reduced Fermi level are plotted on the logarithmic scale.

4. The intersection point of these dependencies is found, along with the corresponding free charge carrier concentration values. This will be the IFCCC value sought.

All calculations were performed for temperatures $T = 295$ K and $T = 77$ K. Let us consider both cases in more detail.

$$T = 295\text{ K};\ E_g = 0.17\ ;\ kT = 25.4\times10^{-3}\text{ eV};$$
$$\beta = 0.149;\ \frac{1}{\beta} = 6.69.$$

Formulas (2), (3), (4) will look as follows:

$$n = 2,676\times10^{16}\times {}^{0}L_{0}^{\frac{3}{2}}\left(\eta;\ 0{,}149\right) \qquad (8)$$

$$p_{\mathrm{L}} = 2.676\times10^{16}\times {}^{0}L_{0}^{\frac{3}{2}}\left(-6.69-\eta;\ 0.149\right) \qquad (9)$$

$$p_{\mathrm{H}} = 5.185\times10^{18}\times F_{\frac{3}{2}}\left(-6.69-\eta\right) \qquad (10)$$

Within the range of the reduced Fermi level that interests us ($-6.69 \le \eta \le 0$), the Fermi integrals in formulas (9) and (10) differ only slightly from each other, whereas their coefficients are approximately 190 times different. In other words, $\frac{p_{\mathrm{L}}}{p_{\mathrm{H}}} \simeq \frac{1}{190}$, the concentration of heavy holes is more than two orders of magnitude greater than the concentration of light holes. Therefore, the contribution of the latter to the IFCCC value can be neglected, and the n_i value can be calculated based on the relation:

$$n = p_{\mathrm{H}}. \qquad (11)$$

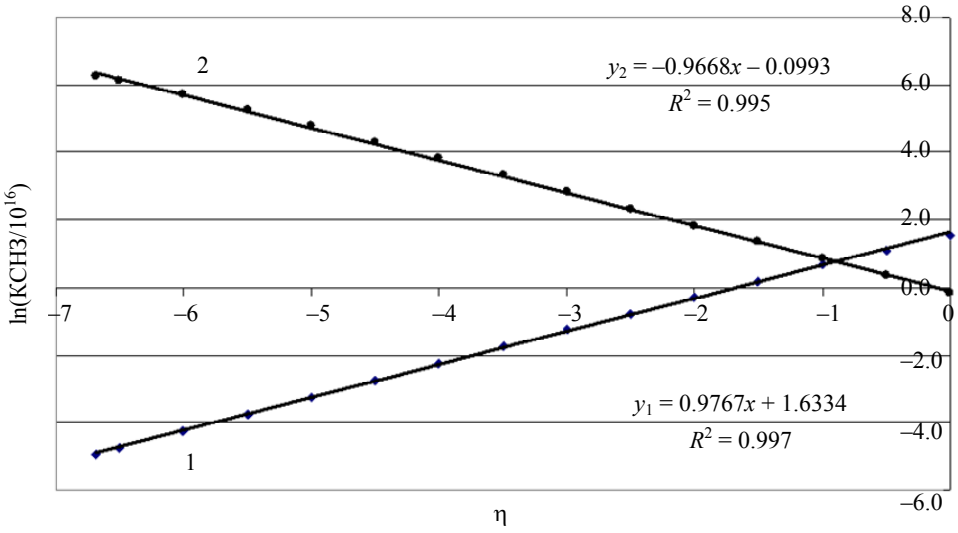

Fig. 2. ($n/10^{16}$) and ($p_H/10^{16}$) vs. reduced Fermi level on the logarithmic scale for T = 295 K: 1 – electrons; 2 – heavy holes

Figure 2 shows the calculated dependencies of IFCCC vs. reduced Fermi level on the logarithmic scale for $T = 295$ K. Both dependencies are seen to be well described by linear functions. The intersection point has the coordinates: $\eta_i = -0.8915$, $\ln(n/10^{16}) = 0.7627$, which corresponds to an intrinsic carrier concentration $n_i = (2.14 \pm 0.01)\times10^{16}$ cm^{-3}.

Now let's consider the case of low temperatures.

$$T = 77\ \mathrm{K};\ E_g = 0.23\ \mathrm{eV};\ kT = 6.62\times10^{-3}\ \mathrm{eV};$$
$$\beta = 0.0288;\ \frac{1}{\beta} = 34.7.$$

Let's assume that the effective mass of heavy holes does not depend on the temperature and is equal to 0.43 m_0.

Relations (2)–(4) for $T = 77$ K will look as follows:

$$n = 5.620\times10^{15}\times {}^{0}L_{0}^{\frac{3}{2}}\left(\eta;\ 0.0288\right) \qquad (12)$$

$$p_{\mathrm{L}} = 5.620\times10^{15}\times {}^{0}L_{0}^{\frac{3}{2}}\left(-34.7-\eta;\ 0.0288\right) \qquad (13)$$

$$p_{\mathrm{H}} = 6.914\times10^{17}\times F_{\frac{3}{2}}\left(-34.7-\eta\right) \qquad (14)$$

Given that Fermi integrals in formulas (13) are (14) are scarcely different from each other, we will get that $\frac{p_{\mathrm{L}}}{p_{\mathrm{H}}} \approx \frac{1}{120}$.

The dependencies for $T = 77$ K similar to those listed above are shown in Fig. 3. Like in the previous example, both dependencies are well described with straight lines intersecting at the point with the coordinates: $\eta_i = -14.94$, $\ln(n/10^{15}) = -12.91$, which corresponds to an intrinsic carrier concentration $n_i = (2.47 \pm 0.01)\times10^{9}$ cm^{-3}.

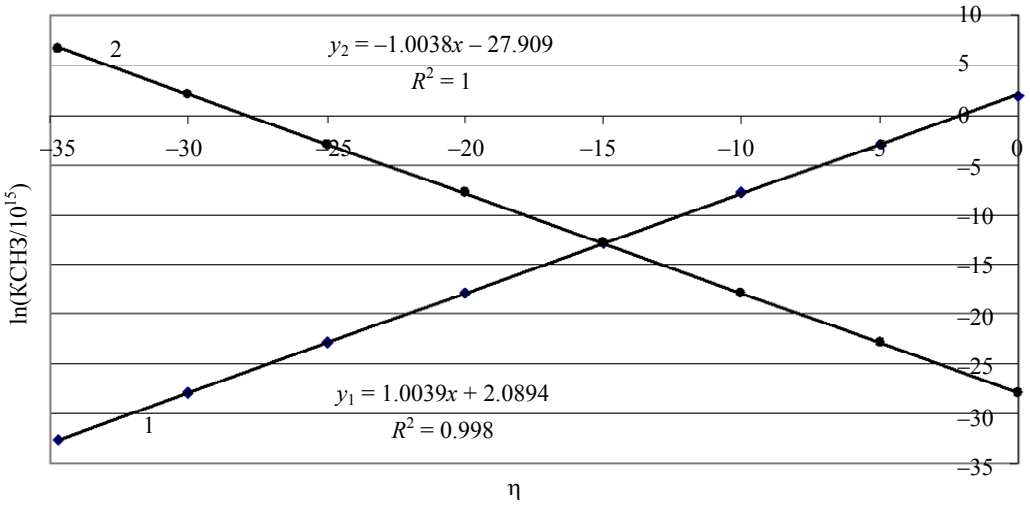

Fig. 3. ($n/10^{15}$) and ($p_H/10^{15}$) vs. reduced Fermi level on the logarithmic scale for $T = 77$ K: 1 – electrons; 2 – heavy holes

Note that η_i at $T = 295$ K lies within the band gap, not far from the bottom of the conduction band, whereas at $T = 77$ K, the corresponding value is close to the middle of the band gap (η_{mid} –17.35). In other words, as the temperature decreases, the Fermi level shifts from above towards the middle of the band gap – a fact well-documented in the literature (see, for example, in [5]).

Is a common knowledge that relation

$$n \times p_L = n_i^2 \qquad (15)$$

shall be valid for nondegenerated semiconductors [5]. Let's verify whether this is true in the cases under consideration. Figures 4 and 5 show the curves of the product of electron and heavy hole concentrations vs. reduced Fermi level for $T = 295$ K and $T = 77$ K, respectively; the horizontal line indicates the value n_i^2.

As can be seen in Figures 4 and 5, relation (15) is only approximately satisfied, with maximum deviation of $n \times p_H$ values from n_i^2 being +5.7 % at $T = 295$ K and +6.9 % at $T = 77$ K. It should be noted that at $T = 77$ K, the $n \times p_H$ curve has a segment parallel to the horizontal line n_i^2 (see Fig. 5), whereas the $n \times p_H$ curve at $T = 295$ K has a distinctly bell-shaped form (see Fig. 4).

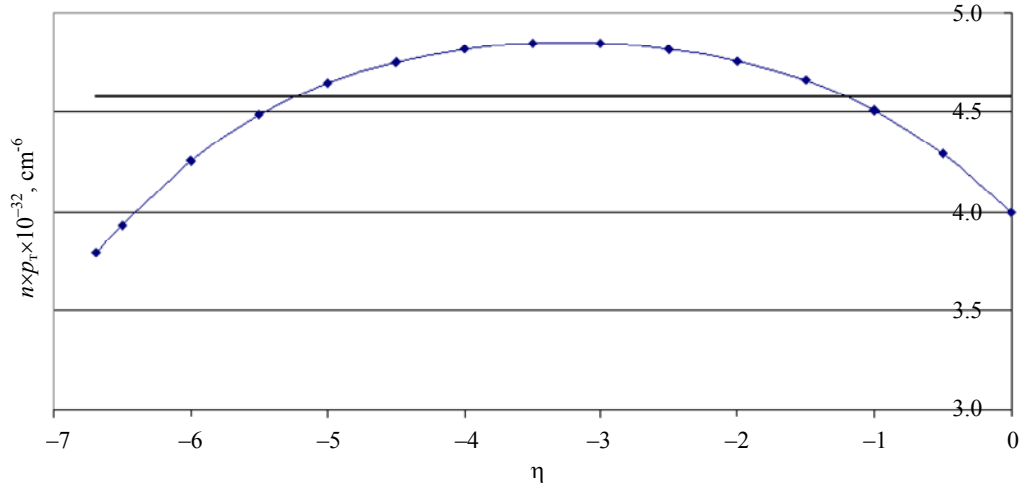

Fig. 4. Product $n \times p_H$ vs. reduced Fermi level for $T = 295$ K. Horizontal line corresponds to value $n_i^2 = 4.58 \times 10^{32}$ cm^{-6}

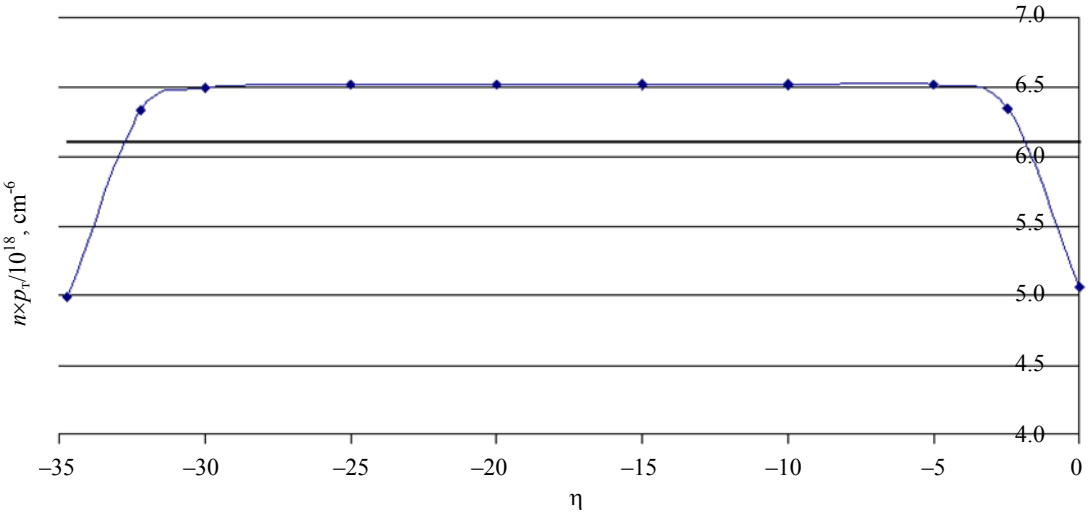

Fig. 5. Product $n \times p_H$ vs. reduced Fermi level for $T = 77$ K. Horizontal line corresponds to value $n_i^2 = 6.10 \times 10^{18}$ cm^{-6}

We attribute these differences to the nonparabolicity of the conduction band, which is significantly greater at the room temperature: $\beta_{295} = 0.149$; $\beta_{77} = 0.0288$.

Discussion of experimental results

Let's now proceed to discussing the literature data concerning the experimental determination of IFCCC values. IFCCC values are usually derived from the curve of the Hall coefficient, R (on the logarithmic scale), vs. the inverse temperature, $10^3/T$ (temperature factor $\sim T^{\frac{3}{2}}$ is also taken into account). One shall find a linear segment on this curve and attribute it to the intrinsic concentration region [6, 7]. However, the method for determining the free charge carrier concentration using the Hall coefficient invites some questions.

To begin with, when determining the IFCCC value, the authors of papers [6, 7] do not account for the influence of light holes. It is assumed that they can be neglected in an intrinsic semiconductor, and that relation (11) is valid.

In the most general case (charge carriers of three types: electrons, light holes, and heavy holes), the expression for the Hall coefficient in weak magnetic fields ($\mu^2 B^2 << 1$) can be written as:

$$R = \frac{1}{e} \times \frac{\left(p_{\rm H} \mu_{p_{\rm H}}^2 + p_{\rm L} \mu_{p_{\rm L}}^2 - n \mu_n^2 \right)}{\left(p_{\rm H} \mu_{p_{\rm H}} + p_{\rm L} \mu_{p_{\rm L}} + n \mu_n \right)^2}, \qquad (16)$$

where $\mu_{p_{\rm H}}$, $\mu_{p_{\rm L}}$, μ_n are mobilities of heavy holes, light holes and electrons, respectively. Formula (16) can be transformed as follows:

$$R = \frac{1}{e p_{\rm H}} \times \frac{\left(1 + \frac{p_{\rm L}}{p_{\rm H}} \times \frac{\mu_{p_{\rm L}}^2}{\mu_{p_{\rm H}}^2} - \frac{n}{p_{\rm H}} \times \frac{\mu_n^2}{\mu_{p_{\rm H}}^2} \right)}{\left(1 + \frac{p_{\rm L}}{p_{\rm H}} \times \frac{\mu_{p_{\rm L}}}{\mu_{p_{\rm H}}} + \frac{n}{p_{\rm H}} \times \frac{\mu_n}{\mu_{p_{\rm H}}} \right)^2} \qquad (17)$$

Now let's estimate contributions of free charge carriers of various types into the Hall coefficient for intrinsic concentration $n = p_{\rm H} = n_i$. Let's choose the values of parameters from formula (17) for the purpose of estimation:

$T = 295$ K: $\frac{p_{\rm L}}{p_{\rm H}} = \frac{1}{190}$ (see above); $\mu_{p_{\rm H}} = 850$ cm^2/(V×s) [1]; $\mu_{p_{\rm L}} =$ = 17,000 cm^2/(V×s) (let's consider relation $\frac{\mu_{p_{\rm L}}}{\mu_{p_{\rm H}}}$ not to depend on the temperature and equal to 20 [8]); $\mu_n =$ = 25,000 cm^2/(V·s). Then, we will get the following from formula (17):

$$R = \frac{1}{e n_i} \times \frac{(1 + 2.1 - 865)}{(1 + 0.105 + 29.4)^2} \qquad (18)$$

Similarly, for $T = 77$ K we have: $\frac{p_{\rm L}}{p_{\rm H}} = \frac{1}{120}$ (see above); $\mu_{p_{\rm H}} = 5{,}000$ cm^2/(V·s) [1];

μ_{p_L} = 100,000 cm^2/(V·s); μ_n = 200,000 cm^2/(V·s). We will get the following from formula (17):

$$R = \frac{1}{en_i} \times \frac{\left(1 + 3.33 - 1600\right)}{\left(1 + 0.167 + 40\right)^2} \qquad (19)$$

As can be seen from formulas (18) and (19), contributions by light and heavy holes are of the same order of magnitude, but when put together they are much lower than the contribution of electrons. In other words, the simple formula used by the authors of papers [6, 7]

$$R = -\frac{1}{n_i e} \qquad (20)$$

can be considered to be quite justified in the above context.

It should be noted that formula (20) is only valid for the weak magnetic fields when the below condition is satisfied for all types of free charge carriers:

$$(\mu B)^2 << 1 \qquad (21)$$

where B is the magnetic field induction (taken in terms of T, while μ – in terms of m^2/(V·s)).

It can be seen that this condition is not satisfied for electrons even at T = 295 K; for B = 0.4 T [7], we have $(\mu B)^2 = 1$, and even more this condition is not satisfied at T = 77 K: $(\mu_n B)^2 = 64$. Consequently, when calculating n_i values using the Hall coefficient, it is necessary to use more complex relations that account for the influence of the magnetic field (see, for example, [2]).) instead of formula (20). Formula (20) can lead to significant errors in determining n_i values, which cannot be estimated in advance.

The literature provides for various formulas for calculating IFCCC values over a wide temperature range. All of them are derived from the curves of the Hall coefficient vs. temperature. Without giving these relations here, we will only provide n_i values calculated with the use thereof for T = 295 K: 2×10^{16} cm^{-3} [1]; 1.63×10^{16} cm^{-3} [4]; 1.81×10^{16} cm^{-3} [6]; 1.75×10^{16} cm^{-3} [7]. To these, we add the value $n_i \approx 1.9\times10^{16}$ cm^{-3} obtained by the helicon wave interference method [9].

It can be seen that all these values are lower than our calculated value of $(2.14\pm0.01)\times10^{16}$ cm^{-3}. This slight discrepancy with the experimental data may be due to the incorrect interpretation of the curve of the Hall coefficient vs. temperature (see above).

Regarding the temperature T = 77 K, data on IFCCC values here are very scarce and contradictory. As an example, the data obtained in [8] can be given: extrapolation of the straight line for n_i to the low-temperature region (Fig. 3) gives an approximate value of 2×10^9 cm^{-3}, which is consistent with the results of our calculations: $(2.47\pm0.01)\times10^9$ cm^{-3}.

Conclusion

1. Calculations of the free charge carrier intrinsic concentration in InSb have been made for temperatures T = 295 K and T = 77 K. It was shown that:

$$n_{i_{295}} = (2.14\pm0.01)\times10^{16} \text{ cm}^{-3}$$
$$\text{and } n_{i_{77}} = (2.47\pm0.01)\times10^9 \text{ cm}^{-3}.$$

2. Values of $n\times p_H$ product and n_i^2 have been compared. The maximum difference between these curves has been shown to be 5.7 % for T = 295 K and 6.9 % for T = 77 K.

3. Values $n_{i_{295}}$ and $n_{i_{77}}$ have been compared to the literature data obtained experimentally. The calculated data have been shown to be consistent with the experimental findings.

4. The results obtained are expected to be used to optimize processes for growing and doping InSb single crystals.

REFERENCES

1. New semiconductor materials. Biology systems. Characteristic and properties. Band structure and carrier concentration of indium antimonide (InSb). URL https://www.ioffe.ru/SVA/NSM/Semicond/InSb/bandstr.html
2. Askerov B. M. Kineticheskie effekty v poluprovodnikah. Moscow, Nauka, 1970 [in Russian].
3. Kane E. O., Journal of Physics and Chemistry of Solids **1** (4), 249–261 (1957). https://doi.org/10.1016/0022-3697(57)90013-6.

4. Madelung O. Fizika poluprovodnikovyh soedinenij elementov III-V grupp; per. s angl. Moscow, Mir, 1967 [in Russian].
5. Bonch-Bruevich V. L. and Kalashnikov S. G. Fizika poluprovodnikov. Moscow, Nauka, 1977 [in Russian].
6. Cunningham R. W. and Gruber J. B., J. of Appl. Phys. **41** (4), 1804–1809 (1970).
7. Oszwaldowski M. and Zimpel M., J. Phys. Chem. Solids. **49** (10), 1179–1185 (1988).
8. Ugrin Yu. O. and Sheregij E. M., Fizika i tekhnika poluprovodnikov **22** (8), 1375–1380 (1988) [in Russian].
9. Chen K. K. and Furdyna J. K., J. of Appl. Phys. **43** (4), 1825–1829 (1972).

About authors

Belov Alexander Georgievich, Cand. Sci. (Phys.-Math.), Leading Research Scientist, Giredmet, JSC (111524, Russia, Moscow, Elektrodnaya Ulitsa, 2, bld. 1). E-mail: IADenisov@rosatom.ru SPIN code: 9546-0477, AuthorID: 38536

Kozlov Roman Yurievich, Giredmet, JSC (111524, Russia, Moscow, Elektrodnaya Ulitsa, 2, bld 1), National University of Science and Technology MISiS (119049, Russia, Moscow, Leninsky Prospekt, 4, bld. 1). E-mail: RYKozlov@rosatom.ru SPIN code: 7324-5403, AuthorID: 1302882

Zhuravlev Evgeny Olegovich, Research Assistant, Giredmet, JSC (111524, Russia, Moscow, Elektrodnaya Ulitsa, 2, bld 1), National University of Science and Technology MISiS (119049, Russia, Moscow, Leninsky Prospekt, 4, bld. 1). E-mail: EOZhuravlev@yandex.ru SPIN code: 5492-0419, AuthorID: 1297975

Molodtsova Elena Vladimirovna, Candidate of Technical Sciences, Leading Research Scientist, Giredmet, JSC

Khikheev Nikolay Germanovich, Engineer, Giredmet, JSC (111524, Russia, Moscow, Elektrodnaya Ulitsa, 2, bld 1), National University of Science and Technology MISiS (119049, Russia, Moscow, Leninsky Prospekt, 4, bld. 1).

Sarkisov Nikita Andreyevich, Engineer of 2nd Category, RD&P Center ORION, JSC (111538, Russia, Moscow, Kosinskaya, 9). E-mail: nsarkisov@mail.ru

Pankov Mikhail Aleksandrovich, Cand. Sci. (Phys.-Math.), Head of Laboratory, RD&P Center ORION, JSC (111538, Russia, Moscow, Kosinskaya, 9). E-mail: mpa.off@gmail.com. SPIN code: 7160-9289, AuthorID: 145651

Kulikov Vladimir Borisovich, Dr. Sci. (Eng.), Head of Department, Joint Stock Company “Central Scientific-Research Institute “Cyclone” (107497, Russia, Moscow, Shchelkovskoe Shosse, 77). E-mail: v.kulikov@cyclone-jsc.ru SPIN code: 2840-0055, AuthorID: 1017695

PLASMA PHYSICS AND PLASMA METHODS

UDC 53, 63 PACS: 52.80.Hc
EDN: SCDBMH

Effect of corona discharge plasma on redox processes in soil

V. L. Bychkov*, A. P. Shvarov, A. A. Logunov, D. V. Bychkov and D. N. Vaulin

Faculty of Physics, M. V. Lomonosov Moscow State University, Moscow, 119991 Russia
** E-mail: bychvl@gmail.com*

Received 12.05.2025; revised 6.06.2025; accepted 20.10.2025

Studies have been conducted on the effect of corona discharge plasma on redox reactions of the soil, namely on samples of lowland peat (capillarily saturated with water) and pure quartz sand (air-dry) in pure form and in mixtures with different ratios of peat and sand. Discharge parameters: duration up to 60 minutes, discharge voltage U = 10–20 kV, discharge current I = 20–100 microA. A maximum effect of the corona discharge treatment of the samples has been obtained in relation to the redox potential. The process of oxidation of organic matter is under the influence of ozone and negative ions in the plasma of the corona discharge. The effectiveness of the negative corona is 2–5 times higher than of the positive one and is connected with more effective production of negative ions.

Keywords: corona discharge; redox reactions of soil; lowland peat; pure quartz sand.

DOI: 10.51368/2949-561X-2025-5-43-47

Introduction

The oxidation-reduction potential (redox, ORP) is widely used in scientific research for characterizing soil conditions (moisture, pH, soluble compounds, etc.) [1–6]. Soil ORP is extremely responsive to changes in soil formation conditions, melioration measures, and agricultural practices. For example, liming of acidic soils, plowing, and construction of open drain ditches cause a significant increase in ORP in soils. Conversely, soil compaction, grass sowing, and organic manuring reduce ORP. A pair of electrodes buried in the soil mass or in an extracted soil solution generates a potential difference due to the presence of various redox systems in soil layers, which magnitude depends on the concentration and ratio of oxidizing and reducing agents formed during the soil formation process. This potential difference is convenient as a consolidated figure for the redox potential of a given layer or solution in terms of millivolts. ORP describes the level of activity of reactions involving the transfer or attachment of electrons [1, 6]. In general terms, a redox reaction can be represented as follows [1]: $Ox + ne \rightarrow Red$, where Ox is an oxidizing agent; n is a number of electrons involved in a reaction; e^- are electrons; Red is a reducing agent. Some substances lose electrons and get oxidized (oxidation reaction), while others attach electrons and get reduced (reduction reaction). Most oxidation reactions of organic substances are irreversible.

A subject of scientific interest is the use of cold corona discharge plasma to stimulate ORP as a factor in soil development over time under artificial conditions. This research continues our series of studies regarding the impact of corona discharge plasma on biological objects [8, 9]. The synergistic effects of cold plasma on plants and soil are of significant interest. These issues become particularly relevant when studying the possibility of establishing human habitats in extreme conditions. For this reason, one of the objectives of this paper was to conduct experiments evaluating the impact of corona discharge on ORP in soil.

Objects of the Study

The objects to be studied were samples of lowland peat (capillary-saturated with water) and pure quartz sand (air-dried), both alone and as mixtures with varying peat-to-sand ratios.

Characteristics of the objects of the study:

1. Peat. Peat type: lowland. Peat variety: reed. Degree of peat decomposition: 45.0 %. Botanical composition of the peat sample: reed – 50–55 %, deciduous wood – 15 %, pine bark – 5 %, birch bark – 5 %, bogbean (Menyanthes) – 5 %, horsetail – 5 %, unknown herbaceous remains – 10 %.

2. Peat + medium-grained quartz sand mixtures:

2.1. Pure peat, 100 % wt. of sample, ash content: 10.5 % (89.5 % organic matter, 10.5 % mineral part).

2.2. Peat + sand (78.6 + 21.4) % wt. of sample (70.3 % organic matter, 29.7 % mineral part).

2.3. Peat + sand (50 + 50) % wt. of sample (44.25 % organic matter, 55.75 % mineral part).

2.4 Peat + sand (21.4 + 78.6) % wt. of sample (19.2 % organic matter, 80.8 % mineral part).

2.5. Pure medium-grained quartz sand, 100 % (100 % mineral part).

Methods of study and Experimental Setup

Samples weighing 70 grams were treated both with negative and positive corona discharge plasma (U = 10–20 kV, I = 20–100 μA) for 60 minutes. The corona discharge was selected based on data indicating its air plasma is rich with ions and its known properties, commonly utilized in practice for ozone generation [10]. After treatment, one portion of the samples was brought to a paste-like consistency for measuring the specific electrical conductivity parameter. Another portion of the samples was placed in flasks where distilled water at a soil-to-water ratio of 1:5 was added. The flask was shaken for 10 minutes and filtered through a paper filter. The filtered samples of the water extract from the soil were analyzed for specific electrical conductivity and ORP value. The ORP value was measured in the water extract (1:5) from the samples using an ORP analyzer during the experiment. The electrical conductivity of the soil pastes was determined using Land Mapper instrument [7].

A schematic of the experimental setup for treating soil samples with corona discharge is detailed in papers [8, 9]. The setup consists of a cell filled with soil samples and an electrical circuit. The upper electrode was a multi-needle system (29 needles) with a needle tip radius of 0.4 mm. The needles were positioned 5–15 mm above the sample surface. The cells were made of either metal or dielectric material. The discharge current was measured with a milliammeter, and the voltage was measured using a circuit comprising resistor R_1 and a milliammeter. The current-voltage characteristics of the discharge above the soil surface were measured.

The drift time t of the generated ions in the corona discharge electric field is approximately [11] $t = x/v = 5\times10^{-7} – 5\times10^{-6}$ s, where x is the distance from the needle electrode to the soil surface (5–7 mm), and $v = 10^5–10^6$ cm/s is the ion drift velocity. This time is significantly shorter than the typical soil treatment duration. The active particles generated in the air plasma rapidly move towards the soil surface due to diffusion. The characteristic diffusion time t_D is equal to [12], $t_D = x^2/D$, where D is the ion diffusion coefficient (typical diffusion coefficients are: O_2^- in oxygen - 0.83 cm²/s, O_3^- in oxygen – 0.056 cm²/s, N_2-O_2 atoms – 0.182 cm²/s). The characteristic diffusion time for particles generated in the plasma to reach the soil surface ranges from 0.3 to 1 s, which is also much shorter than the plasma treatment time. Therefore, the generation of active particles in the air by the corona discharge, which influence ORP of soil can be considered a significant factor of the plasma impact.

Results of Experiments Using Negative Corona

Table 1 presents the parameters of the negative corona discharge.

Table 2 provides specific electrical conductivities of the soil paste.

The organogenic sample exhibits the maximum specific electrical conductivity equaling to 1174 μS/cm. As the mineral component of the samples increases, the electrical conductivity decreases. It is minimal in pure sand and equals 68 μS/cm.

Treatment of the samples with corona discharge leads to an increase in the specific electrical conductivity (Table 2). As the organic component fraction in the samples decreases, the influence of treatment on the electrical conductivity weakens. The influence of the sample treatment on the electrical conductivity growth was also observed in pure sand.

Table 3 presents the results of measuring the redox potential and specific electrical conductivity of the water extract.

The same pattern of the influence of sample treatment with corona discharge was observed during measurement of the water extract's electrical conductivity (Table 3).

Table 1

Negative corona discharge parameters

Sample	Average current, μA	Average voltage, kV	Average energy, J
Peat 100 %	39	7.5	108
Peat + sand 78.6 + 21.4	107	8.6	331
Peat + sand 50 + 50	160	7.7	444
Peat + sand 21.6 + 78.6	146	10.4	547
Sand 100 %	210	7.3	551

Table 2

Specific electrical conductivity of the soil paste

Sample	EC check (without treatment), μS/cm	EC treatment, μS/cm	ΔEC, μS/cm (as compared to the check)
Peat 100 %	1174	1300	126
Peat + sand 78.6 + 21.4	972	1055	83
Peat + sand 50 + 50	605	750	55
Peat + sand 21.6 + 78.6	450	485	35
Sand 100 %	68	120	52

Table 3

ORP and specific electrical conductivity of the water extract

Sample	Electrical conductivity, μS/cm		ORP, mV	
	Check	Treatment	Check	Treatment
Peat 100 %	465	544	+38	+815
Peat + sand 78.6 + 21.4	360	390	+65	+665
Peat + sand 50 + 50	270	340	+72	+ 94
Peat + sand 21.6 + 78.4	95	166	+81	+98
Sand 100 %	27	44	+94	+105

The strongest influence of the corona discharge treatment was exercised on the indicator of redox conditions. In all samples under check this indicator ranged from +38 mV for pure peat to +94 mV for pure sand. These ORP values means that reducing conditions prevail, which is characteristic from a perspective of the objects' genesis. Peat is a hydromorphic structure, with reduction processes prevailing in its genesis.

The influence of treating the samples with the negative corona discharge on the ORP indicator was very substantial. The oxidation process of organic matter is accelerated due to several factors. The main oxidizing factor is the action of ozone and negative ions, which are formed in the gas phase of air when the corona discharge acts upon the air, thus generating negative ions and ozone in the air.

Experiment Using Positive Corona

Table 4 shows the parameters of the positive corona discharge.

As can be seen from Table 4 the exposure conditions varied significantly. Probably, the measurement results were strongly influenced by the humidity level in the laboratory, or the homogenization (mixing) of the peat and sand mixture was incomplete.

Table 5 provides the results derived from the specific electrical conductivity of the soil paste and ORP of samples treated with the positive corona.

The ORP value for the "peat + sand 21.4 + 78.6 %" variant is higher than that for the "peat + sand 50 + 50 %" variant. However, this is not a measurement error but rather an indicator of incomplete homogenization (mixing) of the peat and sand mixture.

In the case of the positive corona ORP turns out to be significantly lower than in the case of the negative corona. This demonstrates the greater potential of using specifically the negative corona for soil activation.

Table 4

Positive corona discharge parameters

Sample	Average current, μA	Average voltage, kV	Average energy, J
Peat 100%	6.3	4.0	9.1
Peat + sand 78.6 + 21.4 %	3.1	13.0	14.5
Peat + sand 50 + 50 %	76	2.5	68
Peat + sand 21.4 + 78.6 %	216	3.9	303
Sand 100%	12.8	10.4	48

Table 5

ORP of the soil paste and specific electrical conductivity of samples treated with the positive corona

Sample	ORP, mVolt	EC of water extract, μS/cm	EC of paste, μS/cm
Peat 100%	+156	1195	1698
Peat + sand 78.6 + 21.4 %	+110	893	1336
Peat + sand 50 + 50 %	+70	574	923
Peat + sand 21.4 + 78.6 %	+105	282	622
Sand 100%	+45	75	136

Conclusion

Treatment of soil with the corona discharge resulted in a significant influence on the redox potential indicator, which is a positive factor in analyzing the discharge's impact on soil. In all samples under check this indicator ranged from +38 mV for pure peat to +94 mV for pure sand. These ORP values mean that reduction conditions prevail. Peat is a hydromorphic structure, with reduction processes prevailing in its genesis. The nfluence on the ORP indicator proved to be very substantial because the oxidation process of organic matter is accelerated by several factors implemented in the corona discharge plasma.

A comparison of the effectiveness of positive and negative coronas shows the higher efficiency of the negative corona. This may be due to the generation of negative ions [10] of O^- and O_2^-, which cause generation of additional atomic oxygen followed by ozone formation. Such a channel is absent when a positive corona acts on air.

REFERENCES

1. Orlov D. S., Sadovnikova L. K. and Sukhanova N. I. Chemistry of soils. Moscow, Vysshaya shkola, 2005 [in Russian].
2. Tsapko Y. L., Zubkovskaya V. V. and Ogorodnaya A. I., Pochvovedenie – agrokhimiya, No. 1, 78 (2017) [in Russian].
3. McKenzie L. J., Whiteside E. P. and Erickson A. E., Soil Sci. Soc. Am. J **24**, 300 (1960).
4. Yu K. and Patrick W. H., Soil Sci. Soc. Am. J **67**, 1952 (2003). doi: 10.2136/sssaj2003.1952.
5. Bohn H. L., Soil Sci. **112**, 1 (1971).
6. Hunting E. R., Harrison R. G., Bruder A., van Bodegom P. M. et al., Front. Physiol**. 10**, 1, D (2019).
7. Pozdnyakov A. I., Pochvovedeniye, No. 10, 1188 (2008).
8. Bychkov V. L., Goryachkin P. A., Chernikov V. A., Shvarov A. P., Izotov A. M., Tarasenko B. A. and Dudarev D. P., Applied Physics, No. 2, 15 (2023) [in Russian].
9. Bychkov V. L., Goryachkin P. A., Vaulin D. N., Shvarov A. P., Izotov A. M., Tarasenko B. A. and Dudarev D. P., Applied Physics, No. 1, 13 (2024) [in Russian].
10. Lunin V. V., Samoilovich V. G., Tkachenko S. N. and Tkachenko I. S. Theory and practice of ozone obtaining and application. Moscow, Moscow university publishers, 2023 [in Russian].
11. Smirnov B. M. Physics of low ionized gas. Moscow, Nauka publishers, 1985 [in Russian].
12. McDaniel R. W. and Mason E. A. The mobility and diffusion of ions in gases. New-York–London–Sydney–Toronto, John Wiley and Sons, 1973.

About authors

Bychkov Vladimir Lvovich, Dr. Sci. (Phys.-Math.), Senior Research Scientist M. V. Lomonosov Moscow State University (119991, Russia, Moscow, 1-2 Leninskie Gory). E-mail: bychvl@gmail.com SPIN code: 2936-1116, AuthorID: 18266

Shvarov Alexander Petrovich, Cand. Sci. (Biol.), Associate Professor, M. V. Lomonosov Moscow State University (119991, Russia, Moscow, 1-2 Leninskie Gory). E-mail: ashvarov@mail.ru SPIN code: 5431-8919, AuthorID: 91766

Logunov Alexander Aleksandrovich, Cand. Sci. (Phys.-Math.), Research Scientist, M. V. Lomonosov Moscow State University (119991, Russia, Moscow, 1-2 Leninskie Gory). SPIN code: 8069-9474, AuthorID: 244088

Bychkov Dmitry Vladimirovich, Cand. Sci. (Phys.-Math.), Research Scientist, M. V. Lomonosov Moscow State University (119991, Russia, Moscow, 1-2 Leninskie Gory). AuthorID: 611220

Vaulin Dmitry Nikolayevich, Cand. Sci. (Phys.-Math.), Research Scientist M. V. Lomonosov Moscow State University (119991, Russia, Moscow, 1-2 Leninskie Gory).

PLASMA PHYSICS AND PLASMA METHODS

UDC 537.52 PACS: 52.80.Wq
EDN: STOBBL

The influence of local conductivity inhomogeneities on the shape of a discharge channel in water

V. A. Panov*, A. S. Saveliev and Yu. M. Kulikov

Joint Institute for High Temperatures of Russian Academy of Sciences, Moscow 125412 Russia
** E-mail: panovvladislav@gmail.com*

Received 23.04.2025; revised 12.05.2025; accepted 20.10.2025

The paper experimentally demonstrates the effect of formation of counter discharge channels during breakdown initiation in weakly conducting water along a trace with increased conductivity from a moving crystal of table salt. The first channel is initiated in the gap between the high-voltage electrode and the salt crystal, due to which the current begins to flow mainly along the trace with increased conductivity as a result of the crystal dissolution. The second channel is initiated inside the trace at some distance from the crystal and has no direct contact with the grounded electrode, which is located at a distance of 8 mm. The counter motion of the discharge channels leads to their unification and final formation of a single channel. This effect is explained based on numerical modeling, which consists in the presence of vortex structures in the trace directly behind the moving crystal, which form a wider, compared to the main part of the trace, region with lower salt concentration and conductivity. As a result, the current density in this region is lower than in the main part of the trace, which leads to later boiling of the liquid and the appearance of a plasma channel.

Keywords: guided discharge; breakdown; water; electrolyte; salt; NaCl; crystal; non-uniform conductivity field.

DOI: 10.51368/2949-561X-2025-5-48-53

Introduction

The electrical discharge direction can be controlled by various methods depending on the medium where it is to propagate. In a gas, this can be achieved either through common thermal effects (heating in the radiation propagation region [1]) or via optical breakdown, which results in a long laser spark [2].

One of the methods to control the discharge direction is breakdown along the media interface [3–5].

As for discharges propagating freely under water, the interelectrode gap is filled with water. Consequently, pre-breakdown phenomena depend on the water conductivity [6], electrode topology, and parameters of high-voltage pulses, which are determined by the pulse excitation circuit. The initial phase of a free underwater discharge may involve the formation of a gas cavity due to Joule heating which is followed by development of a gas discharge within this cavity (the gas bubble theory [7]).

The discharge direction in liquids can be also controlled using laser radiation. Specifically, the paper [8] studies the ability of laser pulses to control water switches designed for powerful accelerators. The authors used three harmonics of pulsed Nd:YAG laser (1064, 532, and 355 nm). Threshold radiation density values were established – 110 J/cm² (14 GW/cm²) for 532 nm.

However, the discharge direction in a liquid can be controlled by a simpler and more economical method. In particular, in the paper [9] a thin metal wire was used to stabilize the breakdown process and to create longer spark plasma channels between electrodes. In such cases, pre-breakdown processes involve rapid

pulsed heating and melting of the wire, followed by breakdown of the channel filled with gas (vapor) and liquid metal droplets. Such breakdowns initiated by the wire typically result in significantly shorter initiation times and lower energy losses as compared to discharges freely propagating in water. This approach has been extensively studied in the paper [10].

The experimental part of study [9] focused on studying pressure pulses generated by freely propagating discharges and discharges initiated with wire in terms of the energy available in the discharge, its losses prior to breakdown, and the energy delivered to the spark channel.

The paper [11] studies the influence of solution conductivity on the pulsed electrical discharge in liquid by means of optical emission spectroscopy in the reactor with electrodes of pin-plane geometry. The emission intensity of hydroxyl radicals (OH-), hydrogen radicals (H+), and oxygen radicals (O-) was measured using the intensity calibration method.

The paper [12] studies the parameters of the pulsed plasma discharge in water for the pin-to-pin electrode configuration. The influence of two parameters was examined: water conductivity (from 50 to 500 μS/cm) and applied voltage (from 6 to 16 kV). Two additional diagnostic procedures based on the refractive index (with time resolution) were used, along with electrical measurements, to study discharge propagation and breakdown in water. For low conductivity (from 50 to 100 μS/cm), the results confirmed the existence of two discharge modes (cathodic and anodic), while an increase of the applied voltage at first promotes the development of the anodic mode. For the conductivity of 500 μS/cm, the cathodic mode primarily develops at a low voltage applied, while a mixed mode (anodic and cathodic) develops at a high voltage applied.

The papers [13, 14] study the phenomenon of discharge on the water surface and under water when lightning strikes a liquid surface. Laboratory experiments were conducted using a point-plane electrode system in a medium simulating seawater. Tap water and salt solutions with varying conductivity were used, and a lightning strike was simulated by a pulsed discharge on the water surface. The curves of the average current value and the electric current density at the anode and cathode vs. the interelectrode distance and electrical conductivity of a medium were derived.

Analysis of the literature references shows that researchers focus on gas-liquid discharges (discharge with a liquid electrode) propagating along and perpendicular to the interface, as well as on discharge development in media with varying electrical conductivity but which is homogeneous over the volume. Thus, currently there are no results on the study of discharge in liquids with conductivity stratification due to spatial inhomogeneity of the equilibrium charge carrier (impurity ion) density.

It was shown earlier [15] that the trace left by a salt crystal moving in weakly conductive water has a guiding effect on discharge development in the water, and the voltage was applied at the moment when the crystal had moved away from the high-voltage electrode, and the discharge propagated along the homogeneous trace as a single (unbroken) plasma channel.

The aim of this paper is the experimental and numerical study of the effect of two separate discharge channels forming at the electrode and in the trace and separated by the crystal.

Experimental Setup and Methods

The experimental part of the work consists of two stages. The first stage involves recording the electrical discharge guided along the trace left by a moving salt crystal. The second stage consists in determining the conductivity of the liquid inside the trace.

The first stage was conducted using the setup described in detail earlier in [15] where the method of uncontrolled seeding of a group of crystals into the discharge gap was replaced by a method of introducing a single crystal into a controlled point within the discharge gap. This was achieved using a thin glass tube with a diameter of 3 mm and a length of about 10 cm. Its tapered end (∅1 mm) touched the water surface at a point above the tip of the high-voltage electrode. When a crystal was introduced into the open end of the tube, the vector of the decreasing velocity was nearly vertical, which improved positioning accuracy and experimental repeatability. The salt crystals were pre-screened by size using vibrational sieves.

At the second stage, the liquid conductivity inside the trace was measured. For this purpose, the setup was modified by changing its optical

and electrical parts. The method for measuring the conductivity in the trace involves measuring the resistance between two electrodes, separated by a known distance and contacting the trace of the identical length and of diameter measured optically.

An optical (shadow) visualization method was used to measure the trace diameter as it allows detecting liquid regions with non-zero salt concentration. Since the accuracy of the trace diameter measurement has the greatest impact on measuring accuracy, a high-speed camera was equipped with a microscope, which allowed to increase the spatial resolution by more than 40 times (to 2 μm/pixel). The remaining parts of the optical system remained unchanged. The optical system was also used to monitor the trace length. For this purpose, the high-speed video camera operated in the mode of start in response to image. The partially sharpened electrode could be seen in the lower part of the field of view, and the video camera was configured to start recording when the salt crystal approached its surface. This same starting method was used at the first (discharge) stage of the experiments. Since camera's output signals were fed to an oscilloscope, it was started at the same moment, which ensured monitoring the length of the trace through which the current flowed. To generate the current, a potential difference was applied to both sides of the trace by supplying a voltage (5 V) to the sharpened electrode and to a 0.2 mm diameter nickel alloy wire, which was positioned inside the glass tube so that its end was flush with the glass tube's opening.

The oscillograms show that when the crystal touches the electrode, its noticeable and relatively rapid increase occurs, and the resistance between the electrodes decreases significantly. The trace resistance between the electrodes was calculated as the ratio of the applied voltage to the difference in current magnitudes measured before and after the salt crystal touched the electrode. Due to the significant difference between the conductivity of the brine in the trace and that of its surrounding water, current flow through the lateral boundaries of the trace can be neglected. Subsequently, the conductivity in the trace was calculated for the DC current conductor of circular cross-section with its known length and diameter. This was possible due to the significant difference between the characteristic time of salt diffusion in water and trace formation time (crystal fall time).

Findings and Discussion

Experimental Results. Figure 1 shows the record depicting the discharge development near the anode tip. The crystal moves along the gravity vector $\vec{g}$ at a speed of approximately 5 cm/s. The automatic voltage pulse is triggered when the distance between the electrode and the crystal is about 50 μm. Within the first 15 μs, the first plasma channel is initiated in the gap between the high-voltage electrode and salt crystal as well as heating and vaporization in the trace behind the crystal which are expressed in the form of darkening of its central part and three separate spots of more intense boiling. These are marked by a dashed line and are likely caused by detachment of macroscopic particles from the crystal. The total resistance of the gap (Fig. 2) between the anode and cathode at first decreases due to occurrence of the first plasma channel, then briefly increases for about 20 μs, which is most likely due to the liquid in the trace changing into the gaseous phase. Ionization then occurs within it, leading to the formation of a second plasma channel, while the gap resistance drops rapidly. A significant non-ionized gap of approximately ~0.5 mm remains between the first and second plasma channels (frame at 31 μs). During the next 30 μs they move towards each other: the first channel goes around the crystal along its surface, while the second advances along the conductive trace towards the first. The channels close up at 55 μs. After this the gap resistance, voltage, and current reach steady-state values.

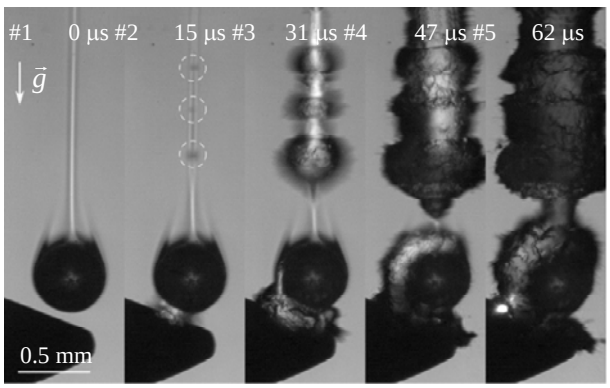

Fig. 1. Photos of the discharge gap during development of electric discharge in water guided by the trace from the sinking sodium chloride crystal. Exposure time 10 μs, 64,000 frames per second

The formation of two counter-propagating channels may be caused by the specific distribution of salt concentration (and conductivity) in the area behind the crystal. The trace contours that can be seen near the crystal surface are an indirect sign thereof – besides the cylindrical vertical part of the trace, which starts at the crystal's upper pole and extends upwards beyond the visible area, lateral traces can also be seen, and these lateral traces originate closer to the equator and are directed towards the cylindrical part at a certain angle.

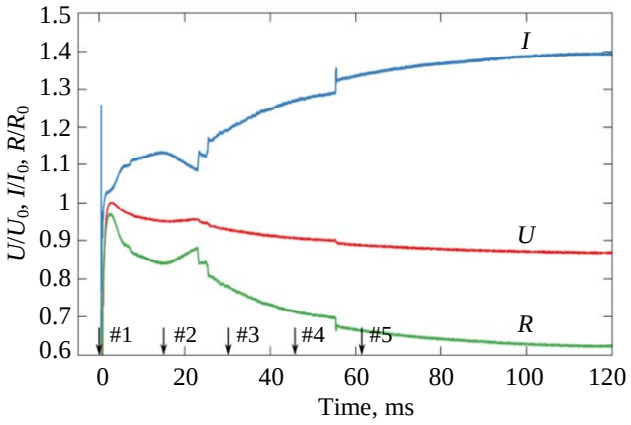

Fig. 2. Oscillograms of voltage (U), current (I), and resistance (R) across the discharge gap that corresponding to the record in Fig. 1. Frame numbers are shown above

Mathematic Simulation. To verify this assumption, two-dimensional (planar) numerical simulation was conducted. It concluded two parts: 1) simulation of the crystal flow-around regime with sodium chloride diffusing from the crystal surface to obtain the salt concentration distribution in the trace; 2) simulation of current flow in water, considering the conductivity heterogeneity.

The results of the flow simulation are presented in Figure 3 for the velocity field (left) and conductivity (right). The crystal flow-around regime is laminar, with a pair of vortices formed on the trace side. Their shape and position determine the distribution of the medium's conductivity (and salt concentration). Its structure matches the one observed during the experiment: the presence of a central part and lateral envelopes originating near the crystal's equator and terminating on the central part of the trace at a distance of about 0.5 mm from the crystal surface. The more elongated shape of the wide part of the simulated trace may be due to the influence of gravity, which is not accounted for in the present calculation but can shorten the length of the wide part of the trace, and also due to the limited sensitivity of the shadow method to density gradients.

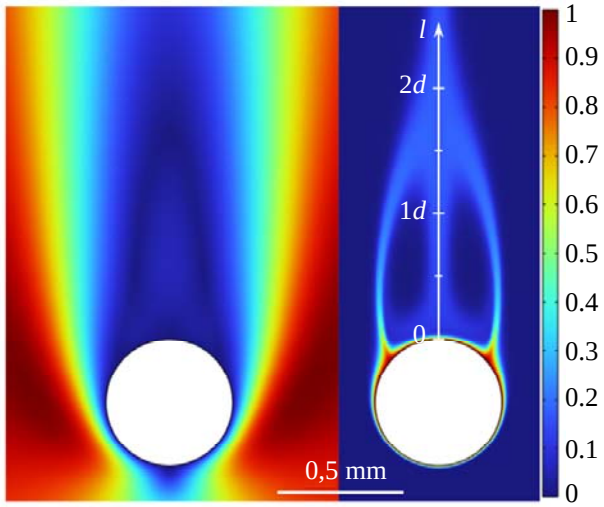

Fig. 3. Simulation results of the crystal flow-around for velocity (left, m/s) and medium conductivity (right, mS/cm)

The results of simulating the electric current flow are shown in Figure 4.

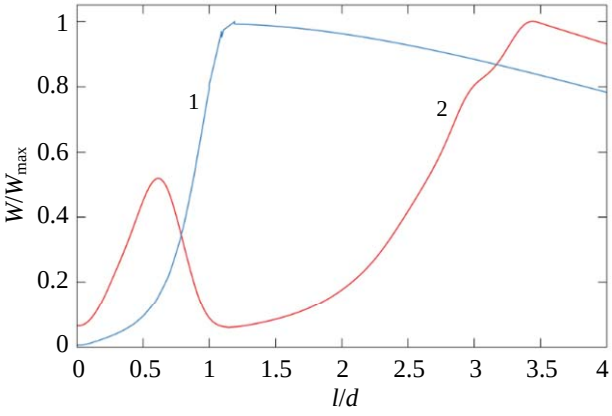

Fig. 4. Simulation results of the heat generation distribution W [W/m^3]/W_{max}[W/m^3] along the trace axis. Distance l is measured from the crystal surface (see Figure 3, right). Curve 1 – the calculation variant with constant conductivity in the trace; curve 2 – the calculation with variable conductivity accounting for vortices

The volumetric heat generation distribution (W/cm^3) is given along the trace axis, with the origin at the crystal surface, in normalized form for two cases: 1) The medium is divided into two regions: the surrounding fluid with a conductivity

of 50 μS/cm, and the trace contour (matching the experimental one) with a constant internal conductivity calculated from the experiment and equal to 50 mS/cm. 2) Differs from the first case by the trace contour and conductivity distribution, which are taken from the calculation. Despite the simplifications assumed in the first case, the heat generation plot (curve 1) agrees well with the boiling pattern observed – the maximum value is reached at a distance of 0.5 mm, where darkening of the trace and subsequent boiling are experimentally observed. In the second case (curve 2), the formation of vortices with reduced conductivity inside them leads to current flowing predominantly in the near-axis zone, thus explaining the local maximum developing near coordinate $x = 0.3$ mm. The amplitude of this maximum is significantly influenced by the calculation time because of the low diffusion of NaCl ions. The graph shown has been selected for the time moment approaching the time of crystal's moving from the water surface to the high-voltage electrode surface. While moving away from the crystal, both graphs show a decrease in heat generation which is caused by the reduced electric field strength due to the increasing distance from both electrodes (high-voltage and grounded). This is consistent with the limited propagation of the discharge channel in the trace previously documented in [15].

Conclusions

The development of the electric discharge in water, which direction is controlled by the conductive trace from the moving NaCl salt crystal, exhibits several features related to the distribution of dissolved salt concentration in the trace, these features having an ultimate influence on the structure of the discharge channel formed. Laminar flow-around of the crystal results in formation of vortices adjoining the crystal on the trace side and contributing to the trace expansion in this part and non-uniform distribution of the dissolved salt. Experimental results and simulation the indicate non-uniform heat generation within the trace, which leads to the initiation of two separate discharge channels separated by a volume of non-ionized liquid. The first channel originates at the electrode surface and terminates at the crystal surface, while the second channel both originates and terminates within the trace, that is it has only indirect contact with electrodes via the surrounding low-conductivity liquid and the trace segment near the crystal (and does not have direct "plasma-metal" contact).

This feature was not observed previously, when the high-voltage electrode remained behind the crystal by the voltage transfer, and the discharge initiated within the homogeneous cylindrical part of the trace. The crystal and the adjacent wide part of the trace found in the path of the discharge channel add a delay of tens of microseconds (under the conditions of this experiment) in the formation of a unified plasma channel. This delay shall be considered for the purpose of any potential practical application of this method for guided breakdown initiation.

REFERENCES

1. Apollonov V. V., Vasilyak L. M., Kazantsev S. Y., Kononov I. G., Polyakov D. N., Saifulin A. V. and Firsov K. N., Quantum Electronics **32** (2), 115–120 (2002).
2. Vasilyak L. M. and Unkovski S. Yu., Teplofizika vysokikh temperature **28** (3), 590–593 (1990) [in Russian].
3. Vaulin D. N., Yershov A. P., Kamenschikov S. A. and Chernikov V. A., High Temperature **49** (3), 356–362 (2011).
4. Shmelev V. M. and Margolin A. D., High Temperature **41** (6), 735–741 (2003).
5. Stephan K. D. and Sheleg G., IEEE Transactions on Plasma Science **43** (2), 501–505 (2015).
6. Hogg M., Timoshkin I., Given M., Wilson M., Macgregor S., Wang T., Fouracre R. and Lehr J., IEEE Transactions on Dielectrics and Electrical Insulation **19** (5), 1559–1568 (2012).
7. Li X., Xiao T., Lan M., He H., Li R., Xiong D. and Li J., IEEE Transactions on Dielectrics and Electrical Insulation **29** (6), 2236–2242 (2022).
8. Woodworth J. R., Zameroski N. D., Johnson D. L., Sarkisov G. S., Blickem J. R., Valde D. M. V. D., Starbird R. L. and Wilkins F. L. Sandia National Laboratories, 2005.
9. Chai Y., Timoshkin I. V., Wilson M. P., Given M. J. and MacGregor S. J., Energies **16** (13), 4932 (2023).

10. Yutkin L. A. Elektrogidravlicheskij effekt i ego primenenie v promyshlennosti. L., Mashinostroenie, 1986 [in Russian].
11. Shih K.-Y. and Locke B. R., IEEE Transactions on Plasma Science **39** (3), 883–892 (2011).
12. Rond C., Desse J. M., Fagnon N., Aubert X., Vega A. and Duten X., Journal of Physics D: Applied Physics **52** (2), 025202 (2018).
13. Midi N. S. and Ohyama R.-I. Proc. 2010 Annual Report Conference on Electrical Insulation and Dielectic Phenomena. West Lafayette, IN, USA, 2010. P. 1–4.
14. Midi N. S. and Ohyama R.-I. Proc. 2011 Annual Report Conference on Electrical Insulation and Dielectric Phenomena. Cancun, Mexico, 2011. P. 223–226.
15. Panov V. A., Saveliev A. S. and Kulikov Yu. M., Applied Physics, No. 6 (in print) (2025) [in Russian].

About authors

Panov Vladislav Aleksandrovich, Candidate of Physical and Mathematical Sciences, senior research scientist, Joint Institute for High Temperatures of Russian Academy of Sciences (125412, Russia, Moscow, 13, Izhorskaya st., bldg. 2). E-mail: panovvladislav@gmail.com SPIN code: 5821-2776, AuthorID: 755538

Saveliev Andrey Sergeevich, Candidate of Physical and Mathematical Sciences, senior research scientist, Joint Institute for High Temperatures of Russian Academy of Sciences (125412, Russia, Moscow, 13, Izhorskaya st., bldg. 2). E-mail: fisteh@mail.ru SPIN code: 6888-7369, AuthorID: 866343

Kulikov Yuri Matveevich, Candidate of Physical and Mathematical Sciences, senior research scientist Joint Institute for High Temperatures of Russian Academy of Sciences (125412, Russia, Moscow, 13, Izhorskaya st., bldg. 2). E-mail: kulikov-yurii@yandex.ru SPIN code: 7719-8459, AuthorID: 1130937

PLASMA PHYSICS AND PLASMA METHODS

UDC 537.527.9; 537.53 PACS: 52.50.Dg
EDN: TXRGLY

Streamer, plasma diffuse jet and glow discharge during breakdown in low-pressure air by a voltage pulse with a front of ~20 ms

V. F. Tarasenko*, N. P. Vinogradov and E. Kh. Baksht

Institute of High Current Electronics, SB RAS, Tomsk, 634055 Russia
** E-mail: VFT@loi.hcei.tsc.ru*

Received 27.05.2025; revised 20.06.2025; accepted 20.10.2025

Formation of diffuse plasma in tubes with inner diameters of 8.4 and 14.2 cm at voltage growth rate V ~ 35 kV/μs and ~ 100 V/ms is investigated. Photographs of discharge glow in different modes are presented. It is shown that at V ~ 100 V/ms and air pressures p 0.4 and 1 Torr, breakdown of the gap is initiated by streamer propagation from a flat electrode of positive polarity. It is established that after the streamer passes the gap plane – tip and forms a red diffuse plasma jet, a glow discharge is formed, which can be maintained both in pulsed and in stationary mode. It is shown that the greatest radiation power from the discharge plasma under these conditions is given by the streamer front, and the greatest radiation energies of the first and second positive nitrogen systems are achieved by increasing the excitation pulse duration during the transition to the glow discharge mode. It is confirmed that at p = 0.4 and 1 Torr the radiation spectrum of the positive column of the glow discharge corresponds to the radiation spectrum of red columnar sprites.

Keywords: plasma diffuse jet; low-pressure air; collision of two jets; capacitive discharge.

DOI: 10.51368/2949-561X-2025-5-54-58

Introduction

There are different shapes of high-altitude discharges (red sprites, blue jets, halo, elves and other, for example, see review [1]). The most of publications are devoted to red sprites, which study is conducted from ground-basea laboratories [2], planes [3], satellites [4] and International Space Station [5]. However, studying high-altitude discharges require large material costs and expensive equipment. Moreover, although the appearance of red sprites is observed above thunder clouds, they appear spontaneously, and their dimensions, shape and place of appearance always differ. Therefore, experimental and theoretical works where main properties of high-altitude atmospheric discharges, mainly red sprites are conducted. At the same time, the used various discharge modes can be conditionally divided into two groups. The first group includes the discharges between metal electrodes are used [6–9]. In the second group analogues of red sprites are formed without contact with metal electrodes [10–14].

One of the issues that requires study is the appearance of a bright luminous area (glow) in red columnar sprites [15]. This area appears in the "column" of sprite after a passage of positive streamer starting from "halo" formation in the mesosphere which has an increased concentration of discharges [1, 15]. As the glow area forms, the streamer's front continues to move down to the thunder clouds and radiation increases. At the same time, the location of glow area practically does not change.

The purpose of this work is to experimentally simulate a bright glow area similar to the one observed in red columnar sprites and analyze the conditions necessary for its appearance. Well-known works did not set

tasks on the experimental simulation of red sprites glow area.

Setup and measurement method

To study the shape and luminosity of the discharge at low air pressure, two setups were used the simplified diagrams of which together with discharge photos are shown in fig. 1 and fig. 2.

Fig. 1. Experimental setup diagram No. 1 with an inserted photo of the plasma diffusion jet (PDJ) glow obtained at an air pressure of 0.4 Torr and exposure of 0.25 s. 1 and 6 – caprolon flanges; 2 – tube made of ESALUX TX polycarbonate with an outer diameter of 15 cm and wall thickness of 4 mm; 3 – grounded electrode made of duraluminum with a hole for quartz tube 4 with an outer diameter of 21 mm and wall thickness 1.5 mm; 5 – external ring electrode made of steel foil with a width of 10 mm; U_1 – pulse generator with a voltage pulse amplitude at a load of U = +7 kV and frequency f = 21 kHz connected to electrodes 3 and 5

Installation No. 1 shown in fig. 1 used a tube made of ESALUX TX polycarbonate with an internal diameter of 14.2 cm which was transparent in the visible spectrum area. Axis tube was located at a distance of 24 cm from the metal plate of experimental bench. Large tube diameter allowed to create plasma diffusion jets (PDJ) far from its inner wall. The tube length was equal to 55 or 147 cm. Plasma diffusion jets were formed from plasma generated by a capacitive discharge limited by one barrier between electrodes *3–5* to which voltage pulses were fed from the U_1 generator. Voltage pulses came with a repetition frequency of 21 kHz with an amplitude of ≈ 7 kV in operational mode. Duration of pulses at half height was ≈ 1.3 μs and their edge and falling edges was ≈ 0.4 μs. Since the red columnar sprites are initiated by positive streamers [1, 15], voltage pulses of positive polarity were often used during the experiments with which PDJ was initiated by positive streamers [11, 12]. Installation No. 2 shown in fig. 2 used a CU quartz tube with an external diameter of 9 cm.

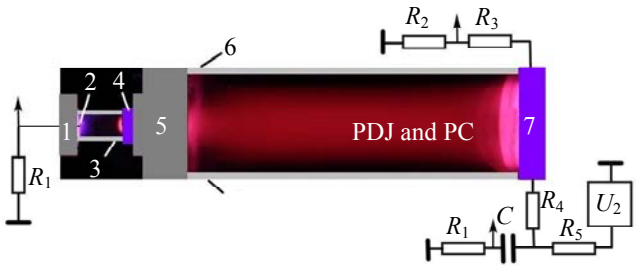

Fig. 2. The diagram of experimental setup No. 2 with an inserted photo of the plasma diffusion jet (PDJ) and positive column (PC) of a glow discharge at air pressure of 0.4 Torr. The photo was obtained at exposure of 3.2 s and the setup was turned on once. In the photo, caprolon flanges 1 and 5 cover electrode 2 and discharge glow respectively. 1 and 5 – caprolon flanges with holes; 2 – grounded electrode made of steel with curvature radius of 0.5 mm; 3 – quartz tube with external diameter of 21 mm and wall thickness of 1.5 mm inserted into the through hole of the flange 5; 4 – external ring electrode made of steel foil with a width of 10 mm which covers the discharge glow; 6 – quartz tube made of CU quartz with an external diameter of 9 cm and wall thickness of 3 mm; 7 – high-voltage plane electrode made of duraluminum. U_2 – DC voltage source. R_1 – shunts, R_2 and R_3 – voltage divider, R_4 – resistance to limit the discharge current, R_5 – charging resistor of capacitor C

Axis of tube 6 was located at a distance of 30 cm from the metal plate of experimental bench. Capacitor C = 10 nF which was connected to high-voltage electrode *7* was charged from the constant adjustable voltage source U_2 with positive polarity and amplitude up to 10 kV through resistance R_5 = 1 MΩ. The second output of capacitor C through metal plate of the experimental bench and shunts R_1 = 20 Ω were connected to additional electrode *2* installed in the center of flange *1* made of dielectric Electrode 4 was under floating potential. Break down voltage at its rate of increase of ~ 100 V/ms at electrode *7* was in kilovolt units. It should be noted that fig. 2 uses a photo of discharge in a dark room, so the flanges *1, 5* and electrodes *4* and *7* were originally black. These flanges and electrodes were colored in different colors for better focus. Moreover, it should be kept in mind that electrode *4* and flange *5* cover the discharge glow in holes.

The shape of the voltage pulses was measured using AKTAKOM ACA-6039 divider. The divider resistance was 900 kOhm (low-

voltage arm) and 900 MΩ (high-voltage arm). Discharge current was defined using shunts with a resistance of 20 Ω. Signals from the divider, shunts and PMT were fed to the MDO 3104 oscilloscope (1 Ghz, sampling frequency 5 samples/ns). Optical radiation from the discharge plasm was registered with Canon 2000D digital camera and through HR2000+ES spectrometer lightguide (range 200–1150 nm; optical resolution ≈0.9 nm). Spectrum sensitivity of HR2000+ES and lightguide were known. The radiation pulse shape was determined using a silicone PMT (Si-PM) as part of MicroFC-SMA-10035 module. Rise time of the PMT transfer characteristic was 0.3 ns, the recovery time of cells was 180 ns, The PMT has maximum sensitivity at a wavelength of 420 nm and it gradually decreases in both direction from the maximum, at the same time, at the edges of the range (320–800 nm) the sensitivity was equal to ≈ 15 % of the maximum value. 3–5 radiation pulses were recorded during measurement the shape and amplitude of which were repeated with a deviation from average pulse not exceeding 10 %. PMT registered radiation from discharge areas with a width of ≈ 1 cm. Center of such areas was in setup No. 2 on its central axis at distances of 2, 12.5 and 27 cm from the left surface of electrode *7*. The remaining part of the tube was covered with black screen. Radiation spectra at this setup were determined in the same areas were radiation pulses from PMT were registered. Photographing the discharge, recording radiation pulses using PMT and measuring of spectra was conducted without external lighting. Relative air humidity in the laboratory room was ≈ 24 % and the temperature was 23 ^{o}C.

Results and their discussion

Fig. 1 shows photo of the discharge obtained at atmospheric air pressure of 0.4 Torr and pulse repetition frequency of 21 kHz. It shows the integral glow of 5250 PDJ of red color with blue shade. When increasing the pressure up to 1 Torr, the PDJ glow intensity and its length decreased. PDJs under these conditions appear due to positive or negative streamers the initiation of which was studied in previous works [11, 12]. At low air pressures and voltage pulse from the first generator ≈ 0.4 μs (voltage growth rate of ≈ 35 kV/μs) streamers were formed due to the creation of dense plasma and quick increase in the reduced electric field strength at its boundary. However, specific density of the PDJ radiation energy to which the streamer front and its afterglow contribute was relatively small. Amplitude of the discharge current and its duration at setup No. 1 were limited due to the dielectric barrier formed by the wall of quartz tube *4*. Therefore, for photographing the discharge it was necessary to use the pulse-periodic mode for PDJ generation.

To increase radiation intensity of the discharge in the studied analogs of red columnar sprites, the following scheme was used, see fig. 2. In this scheme, capacitor C which was connected to electrodes *2* and *7* via resistance R_4 was used to increase the current pule duration. Moreover, DC voltage source U_2 was also connected to electrode 7 via resistance R_5. A current pulse with a greater amplitude and duration than when using U_1 generator was formed with the capacitor. Due to the use of *C*, two electrodes *2* and *7* without dielectric barriers, as well as source U_2, it was possible to ignite a glow discharge at setup No. 2 after formation of PDJ both in single pulse and continuous modes. Discharge at setup No. 2 turned into a flowing one with positive column in tube *6*. In this mode the discharge radiation energy increased significantly, see photo of the discharge per one pulse in fig. 2. In the area near electrode *2* which is a cathode, the radiation color changed as it should be in case of glowing discharge. Application of resistance R_4, as well as the optimization of the capacitor C capacity allowed to exclude the formation of strata in positive column of glowing discharge which was observed in work [13]. An important resulted obtained at this setup in the single pulse mode was initiation of discharge due to positive streamer at voltage rise rate of V~ 100 V/ms and its edge of ~20 μs and more. At voltage rise rate of 35 kV/μs, as was established before, see, for example, work [12], streamers are steadily formed and initiate plasma diffusion jet. Proofs of streamer formation from plane electrode at V ~ 100 V/ms are shown in fig. 3.

The glow of the streamer edge appeared at electrode *7* (oscillogram *2*), then was registered in the central part of tube *6* (oscillogram *3*) and then near flange 5 (oscillogram *4*). The pulse duration

at half height was ~100 ns which complies with measurements in work [12]. The propagation speed of streamer edge was 1.8 mm/ns in the first section from electrode *7* and 1.1 mm/ns in the section of passing the central part of tube *6*. Thus, it was established that at low air pressure and low voltage rise rate, ~20 ms for oscillogram *1* in fig, 3, discharge initiation occurs due to a positive streamer, which forms a PDJ, which switches to the glow discharge mode. Discharge duration, as well its mode, in this case depend on values C, R_4, R_5 and air pressure. Change of values C, R_4, R_5 and voltage of source U_2 allows to change excitation pulse duration and, respectively, radiation pulse duration. Increase of resistance R_5 to 18 MΩ for setup in fig. 2 resulted in limitation of current from source U_2 and the discharge stops in ~ 10 ms. With a tube with a diameter of 15 cm at setup No. 2 we also registered initiation of breakdown by positive streamer starting from electrode *7*.

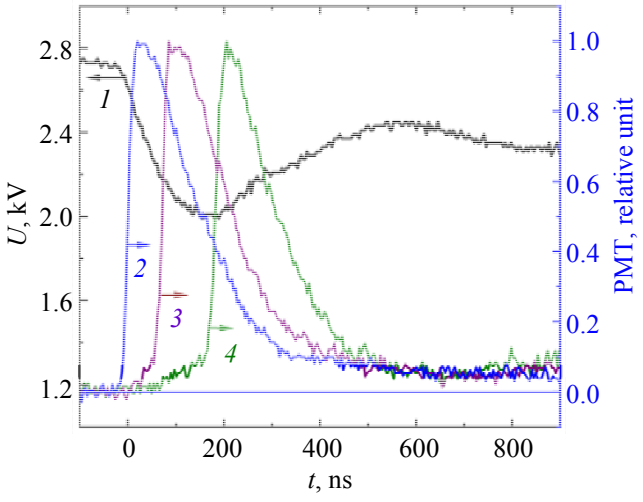

Fig. 3. Oscillograms of voltage pulses U (1) and streamer radiation from areas at distances 2 (2), 14,5 (3) and 27 cm (4) from the left surface of electrode 7 which had positive polarity. C = 10 nF, R_3 = 1 MΩ, R_4 = 10 kOhm, p = 0.4 Torr. Setup No. 2. The photo of discharge glow in this mode is given in fig. 2

From a comparison of discharge color in fig. 1 and fig. 2 it can be seen that at the same air pressure, the blue discharge shade disappeared and in the second case the discharge color began to match better the radiation of red columnar sprites, see, for example, photos in figures under No. 1 in works [13, 16]. Radiation spectrum obtained at setup No. 2 with the main contribution of glowing discharge column is shown in figure 4.

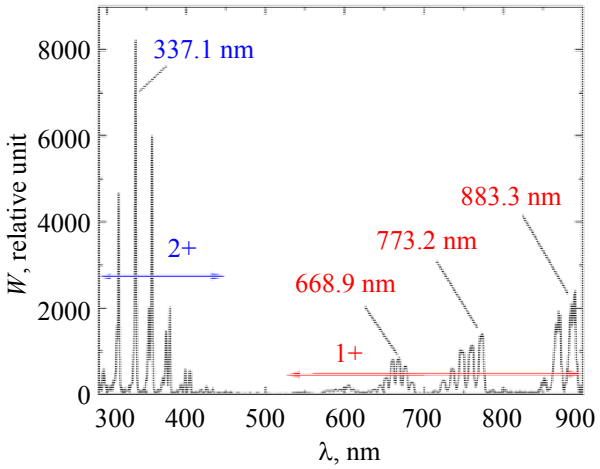

Fig. 4. Radiation spectrum for the conditions in fig. 3 from the area located at a distance of 14.5 cm from the left electrode 7 surface. Exposure time – 30 seconds

The bands of the second (2+) and first positive (1+) systems of molecular nitrogen provided the main contribution to the radiation spectrum. At the same time, the spectral density of radiation energy of three bands 2+ of nitrogen system was significantly higher than in bands of 1+ system that defined the red color of PDJ. A feature of the studied mode is the absence of bands of the first negative system (1-) of molecular nitrogen ion obtained for the glow area during measurement of red sprite radiation spectra [17]. Moreover, a high intensity of radiation from the 1+ bands of the nitrogen system was recorded in the bands with wavelengths of 869.5 and 888.3 nm in the nearest infrared area of the spectrum. In the modes implemented at setup No.1 with microsecond voltage pulses durations, as well as in works [11–13, 16], the spectral energy density of these bands is lower than of the bands with the maximum W at wavelengths of 668.9 and 773.2 nm. It should be noted that a powerful radiation in the infrared area of the spectra [18] was also recorded in the radiation of red sprites.

Conclusion

The conducted studies have shown that it is necessary to change the discharge mode by introducing an additional energy source to increase the intensity of radiation in the red sprite column. It was conducted in the laboratory experiments by to the connection of the capacitor and increasing the duration of excitation pulse. At the same time, the initial breakdown of low-

pressure air was carried out due to the positive streamer which formed the plasma diffusion jet transforming into the positive glowing jet column. According to our hypothesis, a bright luminous glow area is formed in red columnar sprites due to the negative discharges accumulated at altitudes of 60–70km above the sea level by the ice particles, see work [19]. These discharges provide an additional contribution of energy to the sprite column radiation after passing through the streamer and forming glow area. Moreover, the passage of current in this area can be affected by vapors of burnt meteorites from elements with low ionizing potential the impact of which was discussed in work [20].

The authors would like to thank V. A. Panarin and V. S. Skakun for their help in conducting experiments.

The work was carried out with the financial support of the Russian Science Foundation due to No. 24-29-00166.

REFERENCES

1. Surkov V. V. and Hayakawa M., Surveys in Geophysics **41** (5), 1101–1142 (2020).
2. Stenbaek-Nielsen H. C., Haaland R., McHarg M. G., Hensley B. A. and Kanmae T., J. of Geophys. Res. **115**, Art. No. A00E12 (2010).
3. Sentman D. D., Wescott E. M., Osborne D. L., Hampton D. L. and Heavner M. J., Geophys. Res. Letters **22**, 1205–1208 (1995).
4. Garipov G. K., Khrenov B. A., Klimov P. A., Klimenko V. V., Mareev E. A., Martines O., Mendoza E., Morozenko V. S. et al., J. of Geophys. Res.: Atmospheres **118**, 370–379 (2013).
5. Jehl A., Farges T. and Blanc E., J. of Geophys. Res.: Space Physics **118**, 454–461 (2013).
6. Williams E., Valente M., Gerken E. and Golka R. Sprites, Elves and Intense Lightning Discharges. Dordrecht, Springer, 2006.
7. Goto Y., Ohba Y. and Narita K., J. of Atmospheric Electricity **27** (2), 105–112 (2007).
8. Opaits D. F., Shneider M. N., Howard P. J., Miles R. B. and Milikh G. M., Geophys. Res. Letters **37**, Art. No. L14801 (2010).
9. Evtushenko A., Kuterin F. and Svechnikova E., J. of Atmospheric and Solar-Terrestrial Physics **221**, Art. No. 105670 (2021).
10. Robledo-Martinez A., Garcia-Villarreal A. and Sobral H. J., Geophys. Res.: Space Physics **122**, 948–962 (2017).
11. Tarasenko V. F., Vinogradov N. P and Baksht E. Kh., Applied Physics, No. 4, 11–17 (2022) [in Russian].
12. Tarasenko V. F., Baksht E. K., Panarin V. A. and Vinogradov N. P., Plasma Physics Reports **49** (6), 786–794 (2023).
13. Tarasenko V. F., Vinogradov N. P., Panarin V. A., Skakun V. S., Sorokin D. A. and Baksht E. Kh., Atmospheric and Oceanic Optics **37** (1), S183–S191 (2024).
14. Tarasenko V. F., Panarin V. A., Skakun V. S. and Vinogradov N. P., Applied Physics, No. 2, 31–37 (2024) [in Russian].
15. Marskar R., Plasma Sources Science and Technology **33** (2), Art. No. 25024 (2024).
16. Sorokin D. A., Tarasenko V. F., Baksht E. K., Vinogradov N. P., Physics of Plasmas **30**, Art. No. 083515 (2023).
17. Stenbaek-Nielsen H. C., McHarg M. G., Haaland R. and Luque A., J. of Geophys. Res.: Atmospheres **125**, Art. No. e2020JD033170 (2020).
18. Siefring C. L., Morrill J. S., Sentman D. D. and Heavner M. J., J. of Geophys. Res. **115**, Art. No. A00E57 (2010).
19. Hervig M., Thompson R. E., McHugh M., Gordley L. L., Russell III J. M. and Summers M. E., Geophys. Res. Letters **28**, 971–974 (2001).
20. Zabotin N. A. and Wright J. W., Geophys. Res. Letters **28**, 2593–2596 (2001).

About authors

Tarasenko Viktor Fedotovich, Doctor of Physical and Mathematical Sciences, Senior Research Assistant, Institute of High Current Electronics, SB RAS (634050, Russia, Moscow, Akademicheskiy Ave. 2/3). E-mail: VFT@loi.hcei.tsc.ru SPIN code: 2449-8880, AuthorID: 18759

Vinogradov Nikita Petrovich, post-graduate student Institute of High Current Electronics, SB RAS (634050, Russia, Tomsk, Akademicheskiy Ave. 2/3). E-mail: vinogradov@loi.hcei.tsc.ru SPIN code: 7766-5493, AuthorID: 1186281

Baksht Evgenii Khaimovich, Cand. Sci. (Phys.-Math.), Senior Research Scientist Institute of High Current Electronics, SB RAS (634050, Russia, Tomsk, Akademicheskiy Ave. 2/3). E-mail: BEH@loi.hcei.tsc.ru SPIN code: 3676-6490, AuthorID: 40278

PLASMA PHYSICS AND PLASMA METHODS

UDC 533.9.082.5 PACS: 47.80.Jk, 52.70.Kz, 52.80.-s
EDN: UTZOZE

Investigation of gas flows created by a discharge with a liquid electrolyte cathode

A. V. Chistolinov[1,*], P. N. Kazansky[1], R. V. Yakushin[2], V. M. Chepelev[1] and A. S. Tyuftyaev[1]

[1] *Joint Institute for High Temperatures of Russian Academy of Sciences, Moscow, 125412 Russia*
[*] *E-mail: a-chi@yandex.ru*
[2] *Dmitry Mendeleev University of Chemical Technology of Russia, Moscow, 125047 Russia*

Received 14.03.2025; revised 4.04.2025; accepted 20.10.2025

The discharge with a liquid electrolyte cathode at atmospheric pressure in the air was studied using PIV and high-speed photography methods. The velocity field of the gas flows created by the discharge was found. It was shown that the gas flow created by the discharge moves down along the discharge channel to the surface of the solution, reaching a maximum velocity near its surface. Meeting with the surface of the solution, the gas begins to spread along it in a thin layer about two millimeters thick. Thus, it was found that the components of the solution transferred from the solution to the gas phase under the action of a discharge with a liquid cathode are removed from the discharge zone in a horizontal direction, along the surface of the solution.

Keywords: Particle Image Velocimetry (PIV); gas flows; electric discharge; liquid cathode; atmospheric pressure; air; transfer of solution components to the gas phase.

DOI: 10.51368/2949-561X-2025-5-59-64

Introduction

The interaction of electrodischarge plasma with the surface of liquid and, in particular, surface of aqueous solutions is the matter of great interest to researchers in recent years [1]. If the liquid is electrically conductive, the simplest and the most effective way to organize interaction of electrodischarge plasma with its surface is to create electrical discharge in which this liquid will serve as one of electrodes. Such discharge with liquid electrode with a characteristic current from several milliamperes to several hundred milliamperes is a glow discharge at atmospheric pressure [2].

If the solution in this discharge is a cathode, bombardment of solution surface by positive ions results in intensive plasma-chemical reaction in liquid [2, 3]. Therefore, the study of discharge with liquid cathode is of great interest from the point of view of plasma-chemical applications. Liquid cathode discharges have prospects of practical application in new water purification methods, modification of high-molecular weight compounds, sterilization of aqueous solutions, metal content analysis of solutions, biomedical applications and other applications [3–15]. Prospects of practical application make the researches of liquid cathode discharges relevant [16–28].

The value of cathode potential drop in the liquid cathode discharge is quite large and ranges from 400 to 700 V [2, 3] depending on the liquid cathode composition. Therefore, ion bombardment of the liquid cathode surface results in intensive transfer of solution components to gas phase. Transfer of solution components to gas phase under the influence of liquid cathode solution is usually characterized by transfer ratio which is equal to number of substance molecules transferred to the gas phase per one ion bombarding the solution surface [2]. At the same time, not only volatile but also non-volatile solution components, such as metal ions, are

transferred to the gas phase which in particular, allows to detect them in discharge plasma with liquid cathode by emission spectra [8–10, 21, 24].

However, water is transferred most intensively from diluted solution to the gas phase in a discharge with liquid cathode. There are different data on the water transfer to the gas phase in a discharge with liquid cathode because this process apparently depends on may factors such as solution temperature, its mixing mode, etc. [25]. However, in the simplest case, when a discharge with liquid cathode occurs in a non-flowing discharge cell with natural mixing of solution and its natural cooling due to interaction with atmosphere, the transfer ratio of water to gas phase at discharge current of 50 mA is about 500 molecules/ion [29]. According to data [30], current density in cathode spot on the solution surface is 0.5 A/cm^2, and water vapor density at atmospheric pressure and temperature of 100 °C is 0.6 kg/m^3. Under these conditions, an estimate of 0.8 m/s is obtained for average flow rate of water vapor from the cathode spot. At higher vapor temperature the average flow rate from the cathode spot will obviously be even higher.

After flowing from the cathode spot, vapor start interacting with atmospheric pressure. Obviously, as a result of interaction with atmospheric air, temperature of water vapor will eventually become lower than 100 °C and then its partial pressure will become lower than the atmospheric one. Therefore, water vapor can only leave discharge area with air flow. Therefore, the movement of atmospheric air near liquid cathode should have an extremely strong effect on the measured water transfer ratio from aqueous solution.

In this paper we investigate the air movement near discharge channel of the discharge with liquid cathode by particle image velocimetry (PIV) method.

PIV method belongs to the class of non-contact measuring methods of flow velocity. It occupies a special place among other tools for studying the structure of flows due to the ability to record instant spatial distributions of velocity. Measurement of instantaneous field of flow velocity in given cross-section is based on measurement of impurity particles movement located in the cross-section plane over a fixed period of time.

Small particles (tracers) are added to the liquid or gas flow. Laser beam is formed into a light sheet illuminating seeded particles twice with a short time interval. The measuring area of the flow is considered to be a plane cut by “light sheet”. The light scattered by the particles is recorded on two consecutive frames of high-resolution digital camera. Subsequent image processing makes it possible to calculate particle displacements during time between flashes of light source and build two-component velocity field. Measured two-component values of vectors are projections of real (three-dimensional) vectors to the plane perpendicular to the optical axis registering particle images of the equipment [31].

Experimental unit and measurement method

To study the velocity field of gas flows near the discharge channel and solution surface, a liquid cathode discharge was used at atmospheric pressure. The discharge was created between a rod tungsten electrode with a diameter of 2 mm and solution surface. Distance between the rod electrode and solution surface was 4 mm, discharge current – 60 mA.

The solution was in non-flowing cylindrical discharge glass cell with a volume of 100 ml. The depth of discharge cell was 14 mm. The solution level coincided with the edge of discharge cell.

Sodium nitrate solution in distilled water with specific electrical conductivity of 300 μS/cm and pH level = 4.7 was used as solution.

Nikon D500 camera was used to obtained high-speed images of discharge channel with high space resolution. Exposure time of one frame during photo-shooting was 125 μs.

The LaVision FlouMaster Stereo PIV measuring system with resolution up to 50 μs was used to determine velocity of gas flows near the discharge channel and surface of liquid cathode.

Light sheet with a thickness of 0.5 mm formed by laser bean was created in vertical plane at a distance of 1 mm in front of electrode the role of which was performed by tungsten rod with a diameter of 2 mm. Therefore, the survey was conducted in vertical section located at a distance of about 2 mm from the discharge axis. The nearest 0.5 mm near the solution surface did

not fall into the survey area to avoid reflection of laser radiation from the solution surface.

Experimental results and their discussion

High-speed photography (fig. 1) is used to determine the general type of liquid cathode discharge with a discharge gap of 4 mm and discharge current 60 mA for sodium nitrate solution with electrical conductivity of 300 μS/cm and pH level = 4.7.

Fig. 1. Photo of discharge with liquid cathode. Discharge gap of 4 mm, discharge current 60 mA. Sodium nitrate solution with electrical conductivity of 300 μS/cm and pH level = 4.7

Data of high-speed photography showed that the discharge has a shape close to a cone. Cone apex rests again the point of discharge anchoring to the tungsten electrode surface. Solution surface is a cone base. Near the solution surface the discharge channel is divided into separate filaments and each of them ends with separate cathode spot. Study of high-speed photography data showed that the number of filaments and their location changes in time. The diameter of area occupied by cathode spots on the solution surface also changes. The diameter of area occupied by cathode spots does not exceed 4 mm which is in good agreement with data for medium density of cathode current from [8, 9].

Since the light sheet formed by laser beam is quite close to the metal electrode (approximate distance 1 mm), the electrode surface is sightly illuminated by it. A photograph of laser radiation scattering to metal electrode and suspended in air particles made it possible to link the position of electrode and surface solution to the grid (fig. 2). According to this link, the lower electrode limit was at a level of –4 mm and the solution surface was at a level of –8 mm.

Determination of gas flows velocity distribution in the discharge with liquid cathode by PIV method showed that the gas velocity in the area of discharge channel is directed vertically downward (fig. 3). At the same time, the gas flow velocity increases with movement from the tip of metal electrode to the solution surface. The gas flow velocity near the tip of metal electrode is approximately 0.3 m/s and near the solution surface is approximately 0.85 m/s. White vertical line in fig. 3 – result of illumination cause by laser radiation scattering on the electrode surface.

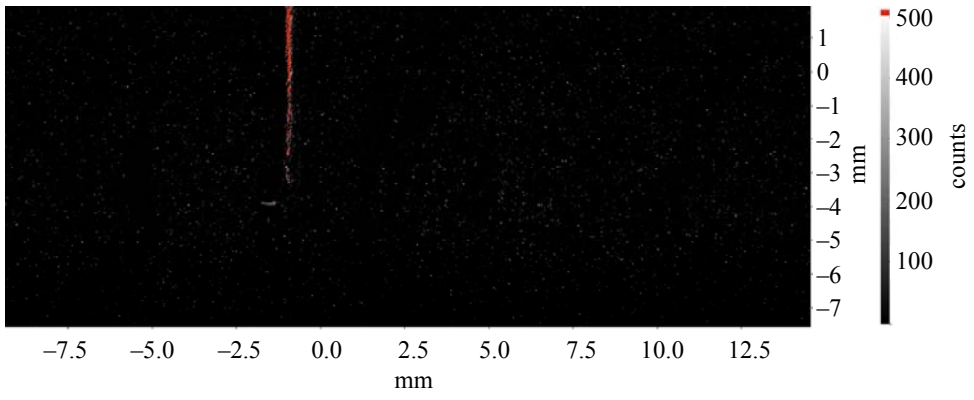

Fig. 2. A photograph of laser radiation scattering to metal electrode and suspended in air particles with linked grid

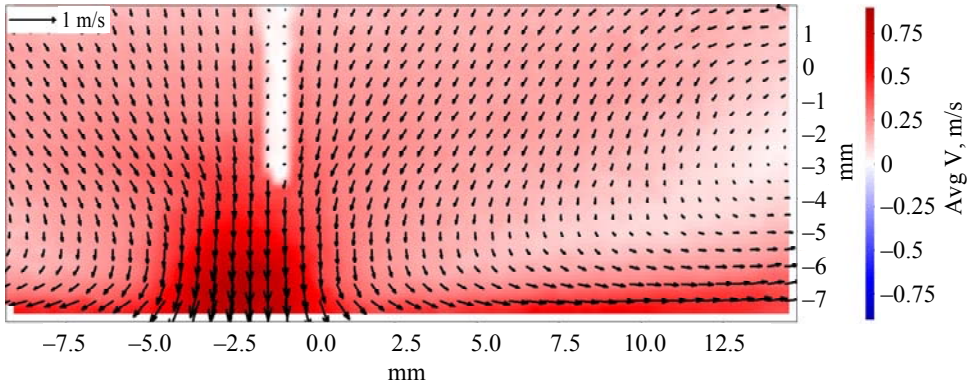

Fig. 3. Distribution of gas flow velocities near the discharge with liquid cathode. Module of gas flow velocity is shown with color

Near the solution surface the gas flow reverses and starts spreading from discharge axis in all directions along the solution surface. Maximum horizontal velocity of the gas flow velocity is achieved near the solution surface at a distance of 0.5 mm from the surface (the layers closer to the surface did not fall into the survey area). The maximum horizontal velocity of the gas flow velocity near the surface is 0.2 m/s (fig. 4).

There is downward vertical velocity of the gas flow velocity at a distance of at least 10 mm from the discharge axis near the solution surface. Gas flow moves almost horizontally along the solution surface at a distance of at least 10–15 mm. Horizontal velocity in this area reaches its maximum. Vertical velocity of the flow velocity directed from the solution surface appears at a distance exceeding 15 mm from the discharge axis.

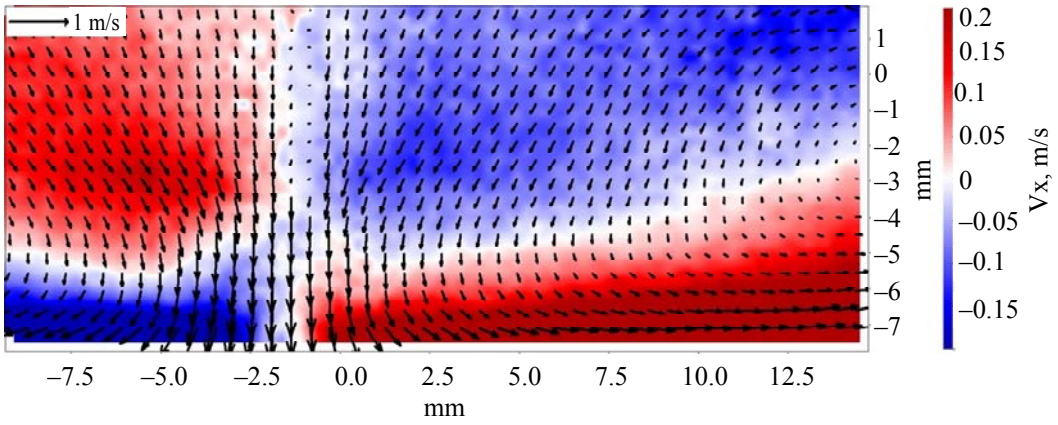

Fig. 4. Distribution of gas flow velocities near the discharge with liquid cathode. Velocity projection to the horizontal axis is shown with color

It can be assumed that in a discharge with a liquid electrolyte cathode the movement of positive ions (the concentration of which considering partial attachment of electrons is higher than the concentration of negative ions) drives the neutral component of the gas which leads to the suction of ambient air from the area near metal electrode and its movement downward to the solution surface. To confirm the mechanism of acceleration of neutral gas component it is planned to conduct further researches that will include analysis of all factors that can cause movement of neutral particles, as well as experiments with polarity change of electrodes.

This work shows that near discharge with a liquid electrolyte cathode gas moves along the discharge channel downward to the solution surface and spreads along the solution surface in a thin layer with a thickness of approximately 2 mm and maximum horizontal velocity of 0.2 m/s. The importance of this result is that in the same thin layer together with gas flows water in the form of vapor and solution microdrops

transferred to the gas phase under the impact of liquid cathode discharge will also be removed from the discharge area. However, due to the thinness of this layer and its proximity to the solution surface, diffusion transfer of solution components from gas phase back to the solution is possible. Vertical velocity of the flow velocity directed from the solution surface appears at a distance exceeding 15 mm from the discharge axis. In this area, the irreversible removal of solution component transferred to the gas phase from discharge cell begins.

Conclusion

The discharge with liquid cathode at discharge gap of 4 mm and discharge current of 60 mA at atmospheric air pressured was studied using high-speed photography and PIV methods. The velocity field of gas flows near the discharge channel and solution surface was measured using PIV method. It is shown that the gas flow created by electric discharge moves downward along the discharge channel to the solution surface. Maximum velocity of vertical gas movement is achieved near discharge channel near the solution surface and is equal to 0.85 m/s. Next, the gas spreads along the solution surface in thin layer about 2 mm thick with a thickness of maximum horizontal velocity of 0.2 m/s. Solution components transferred from the solution to gas phase under the impact of liquid cathode discharge are removed from the discharge area by this gas channel. Considering small thickness of this gas flow and large area of its contact with the solution surface, it can be assumed that some part of solution component transferred to the gas phase can return back to the solution.

The work was performed with the support of the Ministry of Science and Higher Education of the Russian Federation (state assignment No. 075-00269-25-00).

REFERENCES

1. Bruggeman P., Frontiera R., Kortshagen U., Kushner M., Linic S., Schatz G., Andaraarachchi H., Exarhos S., Jones L., Mueller C., Rich C., Xu C., Yue Y. and Zhang Y., J. Appl. Phys. **129**, 200902 (2021).
2. Maksimov A. I. Physicochemical properties of plasma-solution systems and the possibilities of their technological applications. Encyclopedia of low-temperature plasma. Vol. 11 chapter 5 / Ed. Lebedev Yu. A., Plate N. A., Fortov V. E. Moscow, Janus-K, 2006 [in Russian].
3. Kutepov A. M., Zakharov A. G. and Maksimov A. I. Vacuum-plasma and plasma-solution modification of polymeric materials. Moscow, Nauka, 2004 [in Russian].
4. Yang Y., Cho Y. I. and Fridman A. Plasma Discharge in Liquid: Water Treatment and Applications. CRC Press, 2012.
5. Ren J., Yao M., Yang W., Li Y. and Gao J., Centr. Eur. J. Chem. **12** (12), 1213 (2014).
6. Rezaei F., Vanraes P., Nikiforov A., Morent R. and De Geyter N., Materials **12** (17), 2751 (2019).
7. Malik M. A., Plasma Chem. Plasma Proc. **30**, 21 (2010).
8. Mezei P. and Cserfalvi T., Appl. Spectr. Rev. **42**, 573 (2007).
9. Webb M. R., Andrade F. J., Gamez G., McCrindle R. and Hieftje G. M., J. Anal. At. Spectrom. **20**, 1218 (2005).
10. Bencs L., Laczai N., Mezei P. and Cserfalvi T., Spectrochim. Acta, Part B. **107**, 139 (2015).
11. Choi H. S., Shikova T. G., Titov V. A. and Rybkin V. V., J. Coll. Interface Sci. **300**, 640 (2006).
12. Joshi R., Schulze R.-D., Meyer-Plath A. and Friedrich J., Plasma Proc. Polym. **5**, 695 (2008).
13. Saito G. and Akiyama T., J. Nanomat. **2015**, 123696 (2015).
14. Mariotti D. and Sankaran R. M., J. Phys. D: Appl. Phys. **43**, 323001 (2010).
15. Surov O. V., Voronova M. I., Titov V. A. and Zakharov A. G., Applied Physics, No. 1, 17 (2021) [in Russian].
16. Bruggeman P. and Leys C., J. Phys. D: Appl. Phys. **42** (5), 1 (2009).
17. Bruggeman P., Liu J., Degroote J., Kong M. G., Vierendeels J. and Leys C., J. Phys. D: Appl. Phys. **41**, 215201 (2008).
18. Vanraes P. and Bogaerts A., Applied Physics Reviews **5**, 031103 (2018).
19. Verreycken T., Schram D. C., Leys C. and Bruggeman P., Plasma Sources Sci. Tecnnol. **19**, 045004 (2010).
20. Gaisin A. F. and Son E. E., High Temperature **43** (1), 1 (2005).
21. Maximov A. I., Khlyustova A. V. and Khorev M. S., Applied Physics, No. 5, 40 (2008) [in Russian].
22. Tazmeev Kh. K., Timerkaev B. A., Tazmeev G. Kh., Sarvarov F. S. and Arslanov I. M., Applied Physics, No. 2, 58 (2015) [in Russian].
23. Chistolinov A. V., Yakushin R. V., Sargsyan M. A., Khromov M. A. and Perfilieva A. V., Journal of Physics: Conference Series **1556**, 012090 (2020).

24. Chistolinov A. V., Yakushin R. V., Perfilieva A. V., Sargsyan M. A., Gadzhiev M. Kh. and Tyuftyaev A. S., Journal of Physics: Conference Series **1698**, 012020 (2020).
25. Chistolinov A. V., Khromov M. A., Yakushin R. V., Gadzhiev M. Kh. and Tyuftyaev A. S., Journal of Physics: Conference Series **2100**, 012025 (2021).
26. Chistolinov A. V., Tyuftyaev A. S. and Gadzhiev M. Kh., Applied Physics, No. 5, 5 (2021) [in Russian].
27. Chistolinov A. V., Yakushin R. V. and Perfilieva A. V., Applied Physics, No. 1, 12 (2022) [in Russian].
28. Chistolinov A. V., Yakushin R. V., Lubin A. A. and Perfilieva A. V., Applied Physics, No. 4, 5 (2024) [in Russian].
29. Sirotkin N. A. and Titov V. A., Plasma Phys. Tech. **3** (3), 126 (2016).
30. Bruggeman P., Ribezl E., Maslani A., Degroote J., Malesevic A., Rego R., Vierrendeels J. and Leys C., Plasma Sources Sci. Tecnnol. **17** (2), 025012 (2008).
31. Raffel M., Willert C. E., Scarano F., Kähler C. J., Wereley S. T. and Kompenhans J. Particle Imaging Velocimetry A Practical Guide. Springer, 2018.

About authors

Chistolinov Andrei Vladimirovich, research scientist, Joint Institute for High Temperatures of Russian Academy of Sciences (125412, Russia, Moscow, 13, Izhorskaya st., bldg. 2). E-mail: a-chi@yandex.ru SPIN code: 5329-3703, AuthorID: 1192062

Kazanskii Pavel Nikolaevich, Candidate of Physical and Mathematical Sciences, senior research scientist, Joint Institute for High Temperatures of Russian Academy of Sciences (125412, Russia, Moscow, 13, Izhorskaya st., bldg. 2). E-mail: fokkoo@yandex.ru SPIN code: 7674-9889, AuthorID: 887141

Iakushin Roman Vladimirovich, Candidate of Technical Sciences, dean, Associate Professor, Dmitry Mendeleev University of Chemical Technology of Russia (125047, Russia, Moscow, Miusskaya 9). E-mail: yakushin@muctr.ru SPIN code: 7201-2016, AuthorID: 724318

Chepelev Vladimir Mikhailovich, Candidate of Physical and Mathematical Sciences, senior research scientist, Joint Institute for High Temperatures of Russian Academy of Sciences (125412, Russia, Moscow, 13, Izhorskaya st., bldg. 2). E-mail: chepelev@ihed.ras.ru SPIN code: 3535-9857, AuthorID: 1238512

Tyuftyaev Aleksandr Semenovich, Doctor of Technical Sciences, Senior Research Assistant, Joint Institute for High Temperatures of Russian Academy of Sciences (125412, Russia, Moscow, 13, Izhorskaya st., bldg. 2). E-mail: astpl@mail.ru SPIN code: 5341-2934, AuthorID: 40635

PLASMA PHYSICS AND PLASMA METHODS

UDC 537.523 PACS: 52.80.−s
EDN: UUNYOR

Charge estimation at the output of the micro-hollow cathode discharge

E. A. Shershunova*, S. V. Nebogatkin, A. V. Klubkov and K. I. Romanov

Institute for Electrophysics and Electric Power RAS, St.-Petersburg, 191181 Russia
** E-mail: eshershunova@ieeras.ru*

Received 30.04.2025; revised 29.05.2025; accepted 20.10.2025

In this work, an experimental assessment of the amount of charge carried out from a coaxial plasma reactor with a micro-hollow cathode is carried out depending on the supply voltage and the rate of gas pumping through the active zone of the reactor. It is shown that the amount of charge carried out of the reactor is determined not only by the pumping of the gas discharge gap and the distance to the target, but also by the discharge mode. A comparative analysis of different power supply modes revealed a significant difference in the efficiency of charge generation and transport: under DC high voltage, the extracted charge is five times higher than that obtained in pulsed mode. This difference is attributed to both a higher discharge ignition frequency and longer duration of ionization processes in the continuous regime. At the same time, it has been demonstrated that combining a controllable pulsed high-voltage power supply with adjustable gas flow enables flexible control over the charge extraction dynamics, thereby providing the capability for precise, localized, and dose-controlled plasma treatment.

Keywords: micro-hollow cathode discharge; pumping; charge; discharge mode.

DOI: 10.51368/2949-561X-2025-5-65-70

Introduction

Plasma technologies using cold plasma are applied in various fields, including: medicine, agriculture, industry, materials production technologies, energy, and others [1–6]. There are different methods of cold plasma generation. The installations using surface and volume barrier discharges [7–9], and corona discharges [10, 11] are most common. Due to advanced applications as part of devices of illumination [12], micro-propulsion, and precision surface processing, there is significant interest in micron-sized plasma [13, 14], which can be generated in a microhollow cathode discharge, where the cathode contains a cavity tens to hundreds of microns in diameter [15]. Such a micro-discharge can be generated at the very low power consumed: single watts, even at the atmospheric pressure. Furthermore, the microhollow cathode discharge can achieve power densities of up to 100 kW/cm³, making it a unique plasma source.

Typically, a process setup for cold plasma generation includes a plasma reactor with a system of electrodes with the electrical discharge burning between them, a high-voltage power source supplying this reactor, and a working medium flow system that transports the plasma from the reactor's active zone to the processing surface area. Air or inert gases (such as argon, neon, etc.) are often used as the working medium. The type of the high-voltage source is determined by the type of electrical discharge used in the in a diven technology. High-voltage sources of both direct and sinusoidal industrial frequency voltage, as well as sources of pulses with various waveforms, are employed [16, 17, 18].

Depending on the design of the plasma reactor, electrode system, and presence of gas

flow, plasma sources are categorized as direct and indirect. In the case of a direct source, the plasma is generated between the electrodes, one of which is the object. In the case of an indirect source, the plasma is first generated within the reactor and then delivered to the object, which can be either at the floating or ground potential [19]. Indirect plasma sources are sometimes also referred to as plasma jets. The parameters of plasma jets, the transferred charge, and their composition depend both on the discharge parameters, voltage on the reactor electrodes, working medium flow rate rate, and on the target onto which the jet is directed, its material, electrical potential, and distance from the source [18].

This paper evaluates the charge transported from a coaxial-design plasma reactor being pumped, where a microhollow cathode discharge is formed, when different voltage waveforms – direct current and rectangular nanosecond pulses – are applied to the reactor electrodes.

Experimental Setups

The diagram and photo of the experimental setup are shown in Fig. 1.

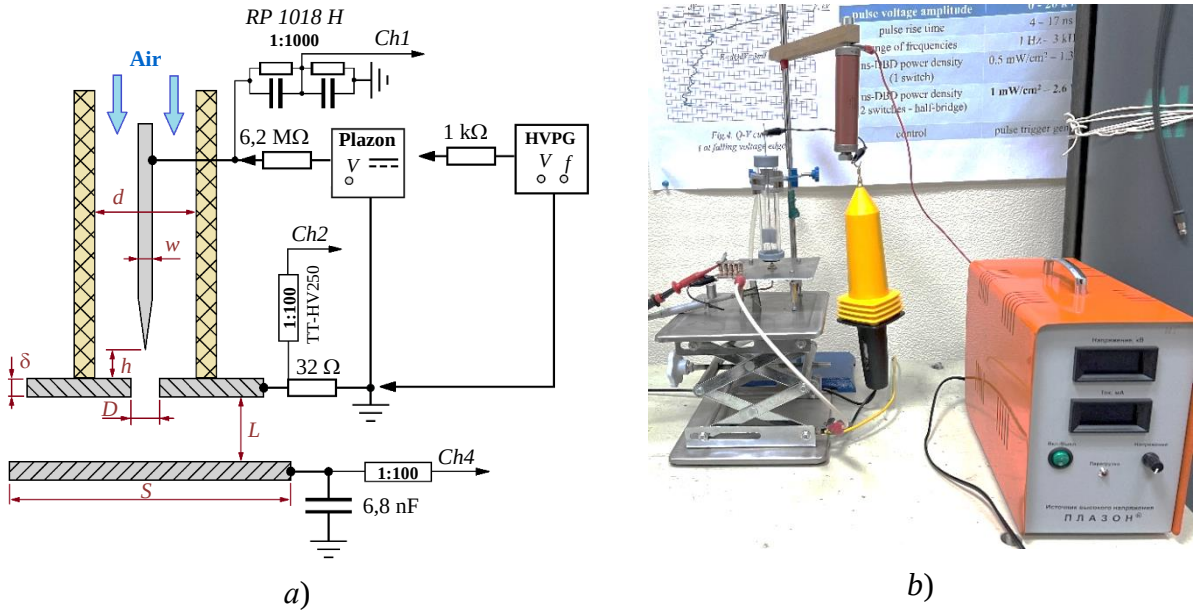

Fig. 1. Diagram (a) and photo (b) of the experimental setup

Two different high-voltage power sources were used in the experiments. Experiments of the first series used a high-voltage pulse generator (HVPG) capable of producing positive polarity pulses with the amplitude of up to 6 kV, duration of 600 ns, rise time of 25–30 ns, and repetition frequency from 100 Hz to 3 kHz [20]. Experiments of the second series used a DC high-voltage power source "Plazon" IVNR-30/10 with the maximum output voltage of up to 30 kV and load current of up to 10 mA. The discharge reactor consisted of a quartz glass tube with an internal diameter $d = 24$ mm, with a refractory tungsten needle with a diameter of $w = 1$ mm positioned in the center and sharpened on one end to a tip radius of $r \approx 0.2$ mm. The high voltage from the generator was applied to the needle via the current-limiting resistor with the resistance of 1 kΩ resistor when powered by the HVPG and with the resistance of 6.2 MΩ when powered by Plazon power source, respectively. Perpendicular to the needle, at the distance of $h = 1$ mm, a flat electrode made of nickel foil with the thickness of $\delta = 0.15$ mm and having a hole with the diameter of $D = 1$ mm was positioned. The discharge was ignited between the needle and the flat nickel electrode. With the air pumped through the reactor tube and out through the cathode hole, discharge products were carried out directionally. The cathode was grounded through the 32 Ω shunt resistor. The voltage across the shunt was measured using TT-HV250 probe with an attenuation factor of 100 and fed into channel 2 of Keysight four-channel digital storage

oscilloscope featuring the 500 MHz bandwidth. The discharge current in the reactor was determined from the voltage drop across this shunt. The voltage drop across the reactor was measured directly at the positive high-voltage electrode (the needle) using high-voltage probe RP 1018 H with the attenuation factor of 1000. The signal from this probe was sent into channel 1 of the oscilloscope. At distance L from the reactor nozzle, a conductive circular target with the diameter of S = 25 mm was placed. To measure the charge, the target was grounded through high-voltage capacitor KVI-3 with the capacitance of 6800 pF. The voltage from this measuring capacitor was fed via the probe with the attenuation factor of 10 into channel 4 of the oscilloscope. Distance L from the cathode to the target varied.

Experimental Results

Based on the oscillographic measurements of the voltage across the measuring capacitor, the curves of the charge transported to the target vs. the air flow rate, $Q_{trans} = f(V)$, were obtained for the reactor supplied with both DC and pulse voltage. The air flow rate through the reactor was changed using a compressor.

It should be noted that when the reactor was powered by the DC voltage depending on the average current, the discharge was generated in two modes: self-pulsing mode at currents up to 1 mA, and continuous burning mode at higher currents, which was also observed in the studies [21, 22].

The curves of the transported charge at the fixed distance to the target for the self-pulsing mode and for powering with rectangular pulses are shown in Figure 2. The curves derived show that at equal air flow rates, the magnitude of the charge transported when the reactor is powered by a DC source is 5 times as high as the charge generated when the reactor is powered by a pulse voltage source.

This difference is partly related to the different discharge pulse frequencies. When powered by the pulse voltage source, the discharge ignition frequency in the plasma reactor was determined by the source's operating frequency (3 kHz), which is more than two times as low as the self-pulsing frequency (when powered by the DC source) (Fig. 3*a*). The discharge current pulse duration at half maximum was approximately 30–40 ns when powered by the DC source, while it was about 250 ns when powered by the pulse voltage source. In self-pulsing mode, the frequency is determined by the gap capacitance [22], which is characteristic of the microhollow cathode discharge. Furthermore, in self-pulsing mode, the voltage waveform across the discharge gap has a sawtooth shape due to the charging process of the system's intrinsic capacitance. During the gradual voltage growth, ionization processes begin slightly before the ignition voltage is reached, thus extending the charge accumulation time respectively.

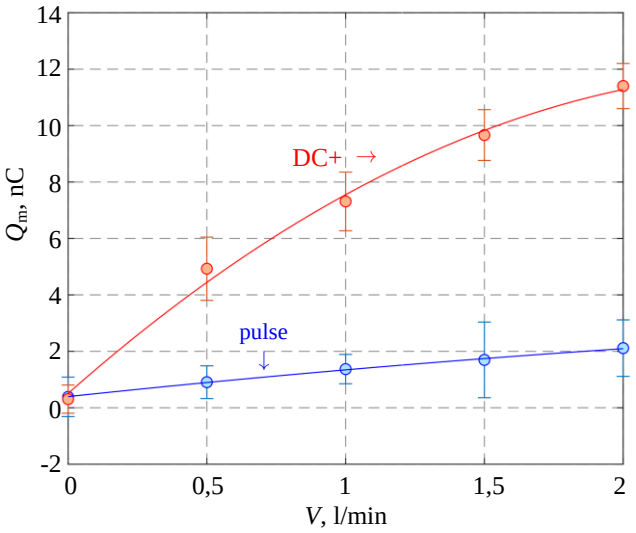

Fig. 2. The charge transported to the target vs. the flow rate through the reactor at the pulse (blue curve) and DC voltages of positive polarity (red curve) (distance to the target L = 3 mm)

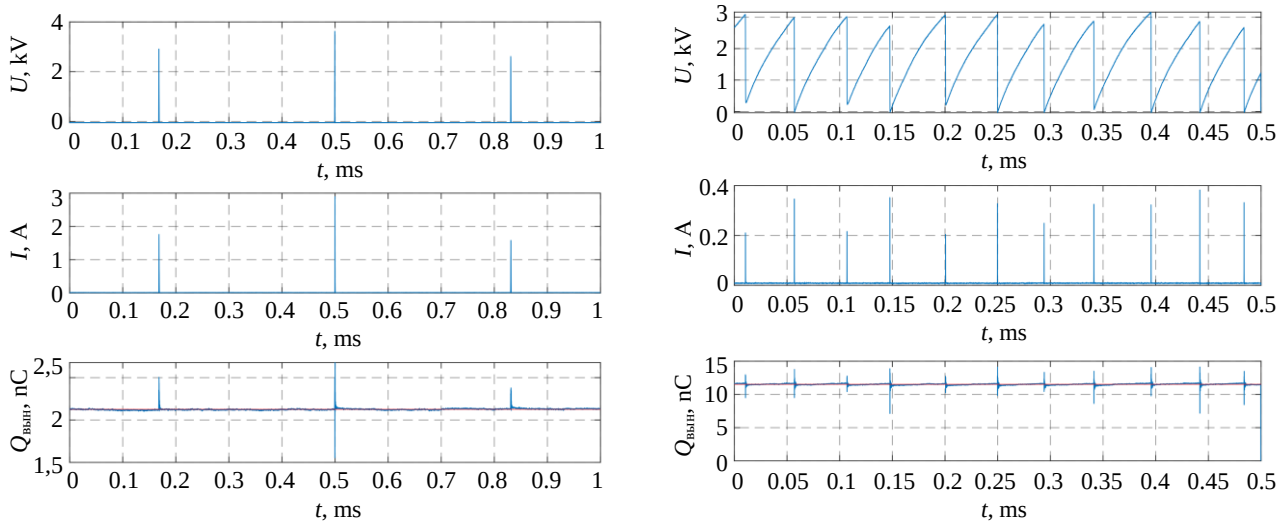

a) *b*)

Fig. 3. Oscillograms of the voltage across the discharge gap, discharge current, and charge transported to the target at the air flow rate of 2 l/min, with the reactor powered by: (a) – HVPG, (b) – Plazon source

Based on the electrostatic field pattern in the reactor's active zone near the cathode at the atmospheric pressure and 30 % humidity, drift velocity of positive nitrogen ions V^{u+} was estimated.

The field pattern, as well as the graph of the electric field strength along the shortest field line (line No. 5 from the bottom), are shown in Figs. 4*a* and 4*b*, respectively. The electric field calculation was performed using BETAFields software for finite-element modeling. The software uses high-order (second and third) triangular finite elements, and gradients are calculated by the SPR gradient recovery method [23]. The calculation model accounted for the geometry of the electrode system and electrical properties of the reactor's construction materials. The model did not account for the space charge.

Since the electric field strength near the cathode surface is relatively weak being less than 1 kV/mm, the mobility can be considered constant, and the ion drift velocity can be assumed to depend linearly on the field strength. According to data of paper [24], under the conditions corresponding to the experiment, the mobility of positive nitrogen ions in air is $k_p = 1.42\times10^{-4}$ m^2/(V·s).

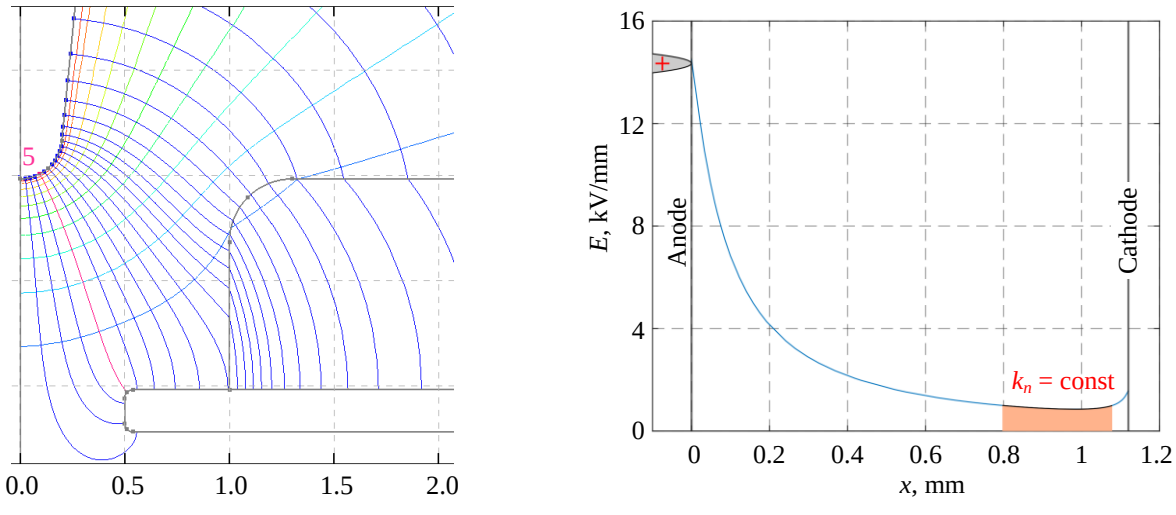

a) *b*)

Fig. 4. Estimation of positive ion drift velocity: (a) – electric field pattern in the reactor's active zone, (b) – curve of the electric field strength along the shortest field line (line No. 5).

When inserting the values of the electric field strength and ion mobility, the characteristic drift velocity of positive ions near the cathode surface is approximately 120 m/s, which is only an order higher than the characteristic flow velocities of the pumped gas (42 m/s at the flow rate of 2 l/min).

Conclusion

An experimental evaluation of the charge transported from the coaxial plasma reactor with the microhollow cathode was conducted. The amount of charge was established to be directly dependent on the velocity of gas flow through the discharge gap. The charge amount was found to be different for different voltage waveforms applied to the reactor electrodes. When the reactor was powered by the DC voltage source, the magnitude of the transported charge was 5 times higher than the charge obtained when powered by the pulse voltage source, which is explained by the larger number of discharge ignition events within a fixed time interval, as well as by the longer duration of ionization processes. However, despite the efficient charge generation using the high-voltage DC source, the use of the regulated high-voltage pulse source combined with the adjustment of the air flow rate through the reactor could allow controlling the dynamics of the transported charge accumulation process. This, in turn, can be useful, for example, for ensuring localized treatment of surfaces made from the most sensitive materials.

This paper was supported by the Ministry of Science and Higher Education of the Russian Federation (FFGR-2022-0007)

REFERENCES

1. Metelmann H. R., von Woedtke T. and Weltmann K. D., Comprehensive Clinical Plasma Medicine. Springer, 2018.
2. Lee T., Puligundla P. and Mok C., Journal of Food Engineering **223**, 168–174 (2018).
3. Baldanov B. B. and Ranzhurov Ts. V., High Energy Chemistry **57** (6), 527–531 (2023).
4. Anisovich A. G., Filatova I. I. et al., Lit'ye i metallurgiya, № 2, 85–91 (2019) [in Russian].
5. Kostov K. G. et al., Applied Surface Science **314**, 367–375 (2014).
6. Cheng C., Liye Z. and Zhan R. J., Surface and Coatings Technology **200** (24), 6659–6665 (2006).
7. Lu X., Laroussi M. and Puech V., Plasma Sources Science and Technology **21** (3), 034005 (2012).
8. Winter J., Brandenburg R. and Weltmann K. D., Plasma sources science and technology **24** (6) P. 064001 (2015).
9. Panousis E. et al., Plasma Sources Science and Technology **15** (4), 828 (2006).
10. Kuwahara T. et al., Thin Solid Films **523**, 2–5 (2012).
11. Schutze A. et al., IEEE transactions on plasma science **26** (6), 1685–1694 (1998).
12. Kogelschatz U., Plasma chemistry and plasma processing **23** (1), 1–46 (2003).
13. Takao Y. et al., Japanese journal of applied physics **45** (10S), 8235 (2006).
14. Shin J. and Tuyen P. D., IEEE Transactions on Plasma Science **39** (11), 2944–2945 (2011).
15. Schoenbach K. H. and Becker K., The European Physical Journal D **70**, 1–22 (2016).
16. Bárdos L. and Baránková H., Thin solid films **518** (23), 6705–6713 (2010).
17. Laroussi M. and Akan T., Plasma Processes and Polymers **4** (9), 777–788 (2007).
18. Shershunova E. A., Moshkunov S. I. and Khomich V. Y., IEEE Transactions on Plasma Science **47** (11), 4909–4914 (2019).
19. Weltmann K. D. et al., Pure and Applied Chemistry **82** (6), 1223–1237 (2010).
20. Moshkunov S. I., Khomich V. Yu. and Shershunova E. A., Letters to the Journal of Technical Physics **45** (3), 34–36 (2019) [in Russian].
21. Moshkunov S. I., Nebogatkin S. V., Romanov K. I. and Shershunova E. A. 15th International Conference "Gas Discharge Plasmas and Their Applications" GDP 2021, Ekaterinburg, 2021, p. 76.
22. Moshkunov S. I et al., Applied Physics, № 5, 11–15 (2021) [in Russian].
23. Lokhanin A. K., Larin V. S. and Matveev D. A., Elektrichestvo, № 7, 82–85 (2005) [in Russian].
24. Zhang B., He J. and Ji Y., IEEE Transactions on Dielectrics and Electrical Insulation **24** (2), 923–929 (2017).

About authors

Shershunova Ekaterina Aleksandrova, Cand. Sci. (Eng.), Head of the Laboratory of High-Power Pulse Technology Institute for Electrophysics and Electric Power RAS (191181, Russia, Saint Petersburg, 18A Dvortsovaya Naberezhnaya). E-mail: eshershunova@ieeras.ru SPIN code: 1314-5887, AuthorID: 630856

Nebogatkin Sergey Vyacheslavovich, Cand. Sci. (Eng.), Head of the Laboratory of Applied Electrophysics Institute for Electrophysics and Electric Power RAS (191181, Russia, Saint Petersburg, 18A Dvortsovaya Naberezhnaya). E-mail: snebogatkin@mail.ru SPIN code: 8374-9520, AuthorID: 172235

Klubkov Alexander Vladimirovich, Junior Research Scientist Institute for Electrophysics and Electric Power RAS (191181, Russia, Saint Petersburg, 18A Dvortsovaya Naberezhnaya). E-mail: a-klubkov@mail.ru SPIN code: 4567-5421, AuthorID: 1181434

Romanov Kirill Ilyich, Engineer Institute for Electrophysics and Electric Power RAS (191181, Russia, Saint Petersburg, 18A Dvortsovaya Naberezhnaya). E-mail: kiromanov@ieeras.ru SPIN code: 2258-4044, AuthorID: 1123274

PHYSICAL SCIENCE OF MATERIALS

UDC 621.315.592 PACS: 81.10-h
EDN: VKMCHY

Measurement of the scales of inhomogeneity in the placement of etch dislocation holes in digital images of GaAs single crystals

N. Y. Komarovskiy[1,2,*], S. N. Knyazev[1], E. A. Sokolovskaya[2], A. V. Kudrya[2], A. S. Sukhanova[2,3], V. E. Antonova[2,3] and E. V. Molodtsova[1]

[1] *Sazhin Giredmet JSC, Moscow, 111524 Russia*
[*] *E-mail: nickkomarovskiy@mail.ru*
[2] *University of Science and Technology MISIS, Moscow, 119049 Russia*
[3] *RD&P Center ORION, JSC, Moscow, 111538 Russia*

Received 2.06.2025; revised 1.07.2025; accepted 20.10.2025

The homogeneity of the properties of semiconductor single crystals has been a key trend in the industry's recent development. However, there is currently no consensus on the degree of property heterogeneity or methods for its assessment. A method for analyzing the heterogeneity of dislocation etch pit distributions is proposed. This method is based on solving the problem of the proximity of binary image objects by partitioning the space into Voronoi polyhedra. Object size filtering was performed taking into account the known nature of the measured objects. A statistical filtering threshold of 585 μm^2 was calculated using a histogram of the distribution of dark object areas. The nature of image noise was clarified through direct observation of etch pits using scanning electron microscopy, which allowed us to estimate the physical filtering threshold at 16 μm. It was found that groups of dark objects identified by "statistical" and "physical" filtering, in the "object area S – its perimeter P" coordinates, corresponded to different slope values of the approximating curves: 0.33 and 0.85, respectively. It was shown that, to obtain objective results in digital image processing, it is necessary to accumulate representative measurement statistics – the size of the measurement area when studying the dislocation structure of GaAs should be at least 0.42 mm^2.

Keywords: Czochralski method; GaAs; etching patterns; dislocations concentration; light microscopy; digital image processing; Voronoi polyhedral.

DOI: 10.51368/2949-561X-2025-5-71-78

1. Introduction

In the course of the last years, the main trend in development of the solid-state field is to achieve the required level of the single crystals structural uniformity that is determined by concentration of dislocation etching pits and their arrangement geometry [1]. In gallium arsenide single crystals grown by the liquid-encapsulated Czochralski method, the dislocation density (N_d) is $\sim 10^4$ cm^{-2}. Their impact of dislocations on electrophysical parameters of the final integrated circuit is ambivalent: on one hand, they create additional levels in the band gap; on the other hand, they are a sink of point defects [2]. Dislocations concentration level in case of growth according to the Czochralski method is foremost determined by the value of thermoplastic deformation relaxation, and lays within N_d: 10^2 (InSb) … 8×10^4 cm^{-2} (GaAs) interval for semiconducting compounds of $A^{III}B^{V}$ group [3, 4].

Non-uniformity of dislocations arrangement depends on the gradient of voltages occurred during growth and is primarily justified by non-uniform temperature field of a furnace [5]. In case

of high-temperature semiconducting compounds of $A^{III}B^{V}$ group (InAs, GaAs), the process is additionally complicated by the need of a molten mass liquid encapsulation which in turn may contribute into non-uniformity of temperature field in the crystal-melt interface. The non-uniformity of the thermal field can be mitigated by adjusting the temperature and dynamic parameters of the growth process – ξ. For instance, varying the temperature of the background heater (within the tolerance range) can reduce heat loss from the surface of the growing ingot [6]. However, it is difficult to assess the effectiveness of such adjustments in practice due to the lack of a measure for structural non-uniformity. Calculating this measure is even more complicated by the presence of objects (noise) on the thin-section surface, the formation of which is unrelated to the material's dislocation structure, as well as by the absence of unified guidelines regarding the required measurement scope.

The objective of this work is to study the nature of noise occurring during formation of etch pit images and to develop a methodology for calculating the non-uniformity of their distribution.

2. Object of the Study

GaAs single crystals alloyed with Te, 40 mm in diameter, were grown with the use of Czochralski method with liquid encapsulation of LEC molten mass in crystallographic direction [100]. The plates cut perpendicularly to the growth axis on the disk-cutting machine were used as the samples. The plates surfaces were ground, chemically polished in acid solution with the following ratio – H_2SO_4, H_2O_2, H_2O (3:1:1) – during 25 seconds at the room temperature, and preferentially etched in KOH alkali melt at 450 °C during 7 minutes [7, 8].

The pan views of dislocation structures on GaAs plates obtained using Axio Observer D1m Carl Zeiss microscope with 50-fold magnification by linking individual frames linking in Thixomet [9] software package were used as the study object.

3. Nature of Image Noises

To detect the nature of noises formation on 2D images obtained using the light microscope, morphology of the etching pits structure was studied by means of observation using the scanning electron microscopy (Fig. 1*a*). The structure of pits on their binary views (based on the approaches proposed in the paper) was similar to the morphology of the etching pits observed by means of the light microscopy (Fig. 1*b*).

For example, the pits with open contour were observed. The slope of dislocations towards the thin section plane could result in their formation on the image, the bottom of such pits was displaced relative to their geometrical center to distance *d* – Fig. 2*a*.

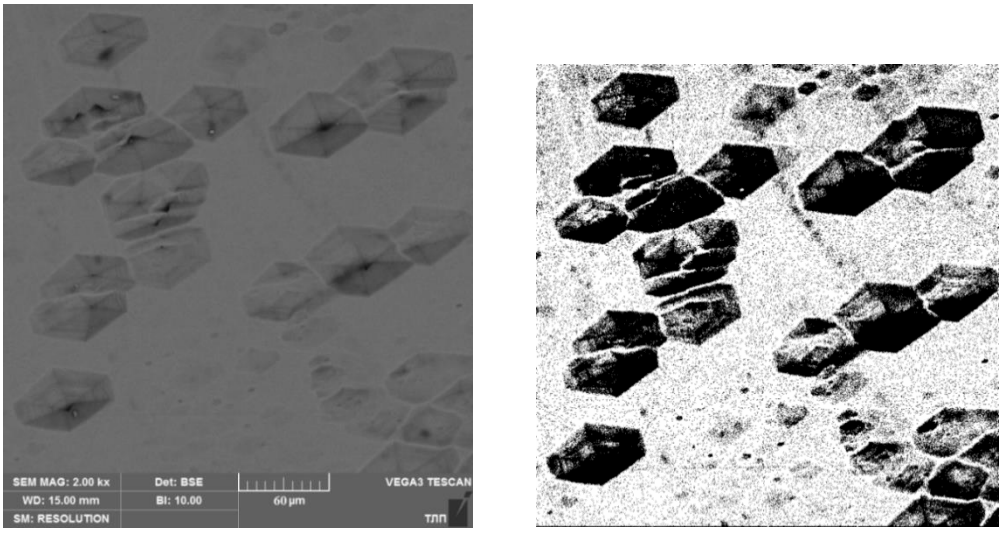

a) *b*)

Fig. 1. Initial image of etching pits in the scanning electron microscope (a) and after binarization (b)

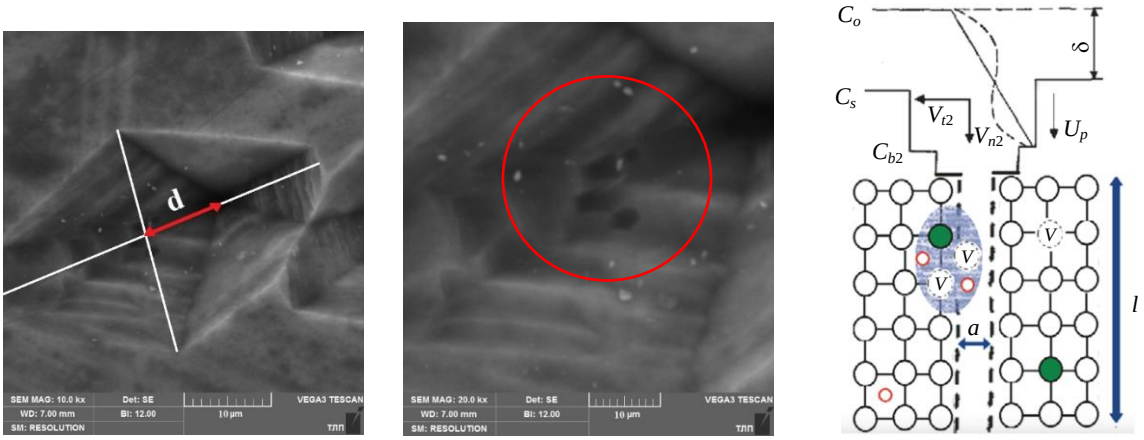

a) *b*) *c*)

Fig. 2. Displacement of the etching pit bottom a); b) – etching pits caused by point defects; c) – scheme of the etching pit formation at the point of dislocation exposure with the Cottrell atmosphere

The sets of point defects constituting the Cottrell atmosphere along the dislocation line (l) of width (a) [10] could create etching pits of regular shape (Fig. 2*c*). Their area generally did not exceed 16 μm^2, which determined the minimum ("physical") filtration limit. The size of dark objects outlined in such manner was significantly lower than the "statistical" filtration limit (585 μm^2) that may be outlined based on histograms of distribution of the dark objects area values. Significantly, three groups of objects on the image compliant with etching pits and background outlined based on physical and statistical filtration limits were consistent with different values of the approximating curves slope angle – 0.13, 0.85 and 0.33, respectively, within "object area *S* – perimeter *P*" coordinates (Fig. 3). Linearity of the approximating curves is a sign of a physical phenomenon self-similarity – its persistency under similar fold change of *S* and *P* coordinates, which may reflect significant difference in the nature of the objects described [11].

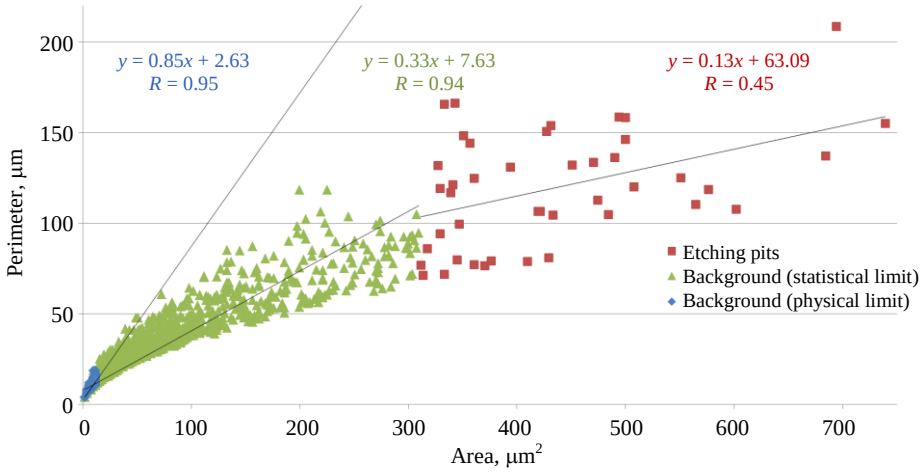

Fig. 3. Dark Objects Perimeter to Area Ratio

The difference in nature of the objects eliminated by physical and statistical filtration can be related to a specific feature of the contour formation process of pits which occur at the points of Cottrell atmosphere plate exposure – their size is determined by dissolution kinetics of dislocations, opposite to the pits formed in the point defects exposure areas [10].

4. Assessment of Non-Uniformity of Etching Pits Arrangement

Outlining the target objects on the binary view – etching pits related to the dislocation structure of a single crystal (using the statistical filtration – area less than 585 μm^2) detected not only their size difference, but also a difference in arrangement on the thin section surface: presence of the areas of accumulation and sparcification (Fig. 4).

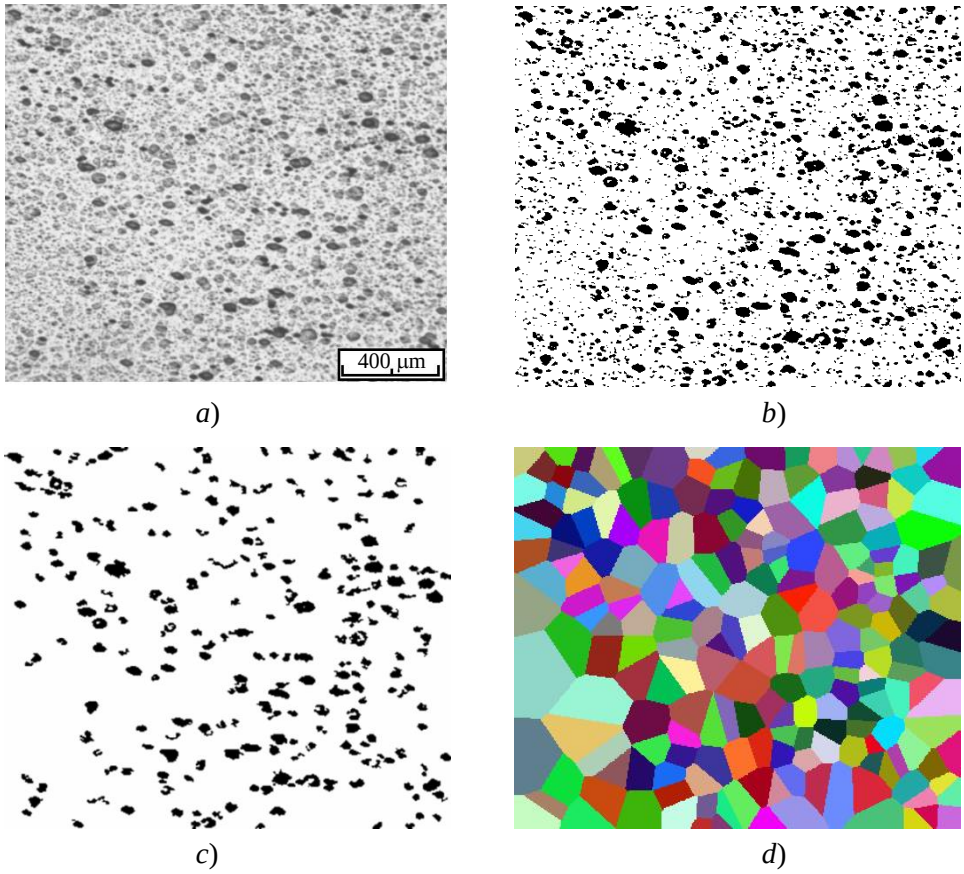

Fig. 4. Initial view (a), its binary representation (b), including the one after statistical filtration (c) and further image partitioning into Voronoi polyhedras (d)

To assess non-uniformity of etching pits arrangement, the space partitioning into Voronoi-Dirichel polyhedras, which are polygons inside which all points (pixel) are located closer to their center than to the centers of adjacent areas, was used (Fig. 4*d*) [17]. Such partitioning allows for intrinsic determination of a distance between the closest etching pits. Fig. 5 shows the histogram of distribution of distances between dark objects– polyhedras centers.

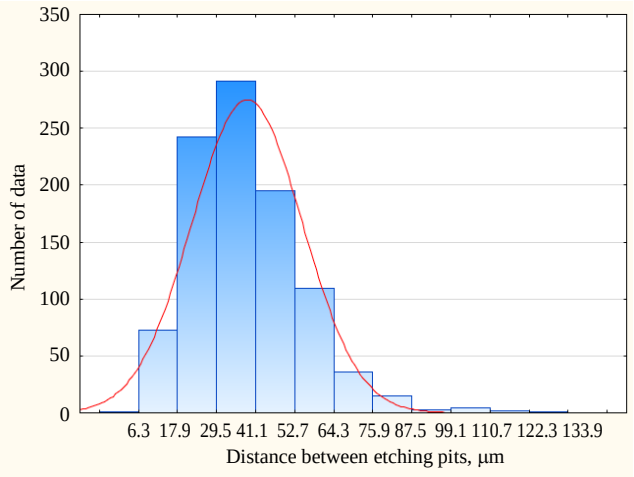

Fig. 5. Histogram of distribution of distances between Voronoi polyhedras centers (etching pits)

Distribution of the distances between the dark objects was different from regular distribution (asymmetry coefficient – 1.12; excess – 2.39), which confirms non-uniformity of etching

pits arrangement visible on the image (See Fig. 4). Hence, for example, the image partitioning into four fragments of equal area (Fig. 6) provides for not only its own average distance between Voronoi polyhedras centers for each of them, but also allows for assessing a statistical nature of their distribution – Table. The obtained results show the need for justification of the minimum scope of experimental data for obtaining repeatable results of measuring etching pits concentration and arrangement on a thin section is raised.

Fig. 7 shows the curves of average values of the dark object areas, the distance between them (polyhedras), numbers of their closest neighbors vs. the measurement scope varied within ~ 0.053 to 0.846 mm^2 (on the plate scale) for two independent parts of the panorama.

Following the obtained results, the measurement area increasing above 0.42 mm^2 provides for stabilization of the obtained characteristics values, regardless of the selected panorama section, thus ensuring their repeatability and compatibility. With the lower sample sizes, it is possible to obtain both identical and opposite results, meanwhile not consistent with the real values to be found. The obtained results confirm the need for obtaining a representative statistics of observations under digital measurements of the structures. It should be also noted that the areas different in terms of etching pits morphology can be observed in macroscale of a sample. Therefore, a comprehensive representation of the etching pits structure can be provided by measuring their geometry on the entire sample (product) scale.

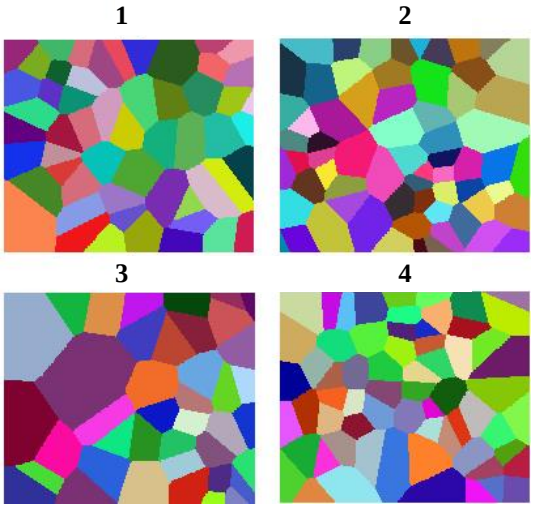

Fig. 6. Partitioning of four fragments of the initial image (Fig. 4) into Voronoi polyhedras

Table

Statistical characteristics of distribution of distances between etching pits for different image fragments shown in Fig. 6

Fragment No.		1	2	3	4
Average distance between polyhedras, μm		38.3 ± 1.1	35.7 ± 0.9	42.4 ± 1.7	36.2 ± 0.9
Coefficients of	asymmetry	1.12 ± 0.26	0.71 ± 0.24	2.13 ± 0.28	0.52 ± 0.24
	excess	1.85 ± 0.55	0.22 ± 0.48	7.54 ± 0.62	0.053 ± 0.49

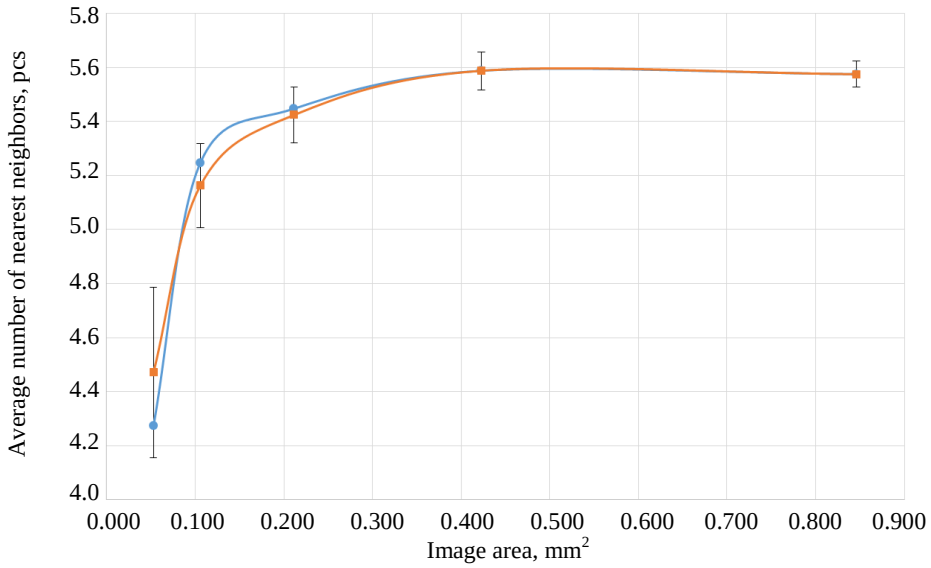

a)

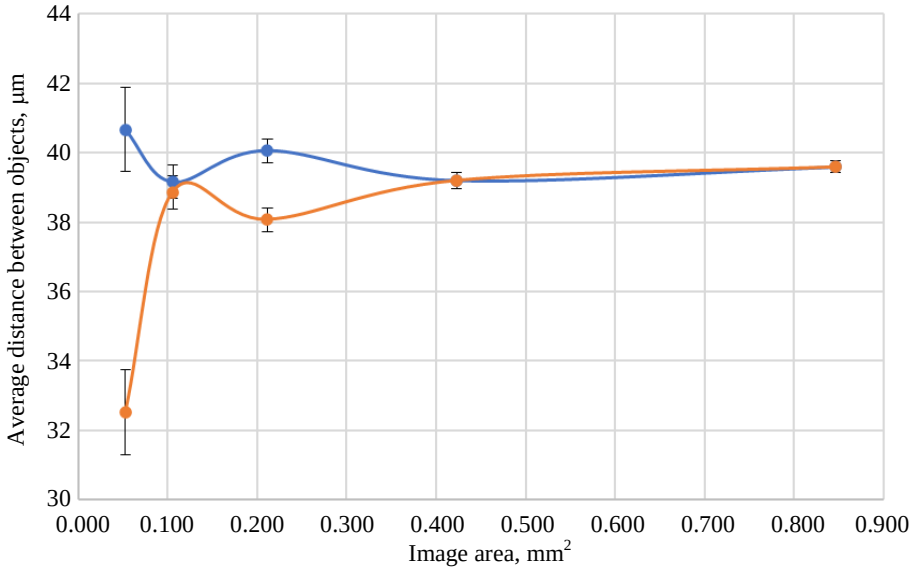

b)

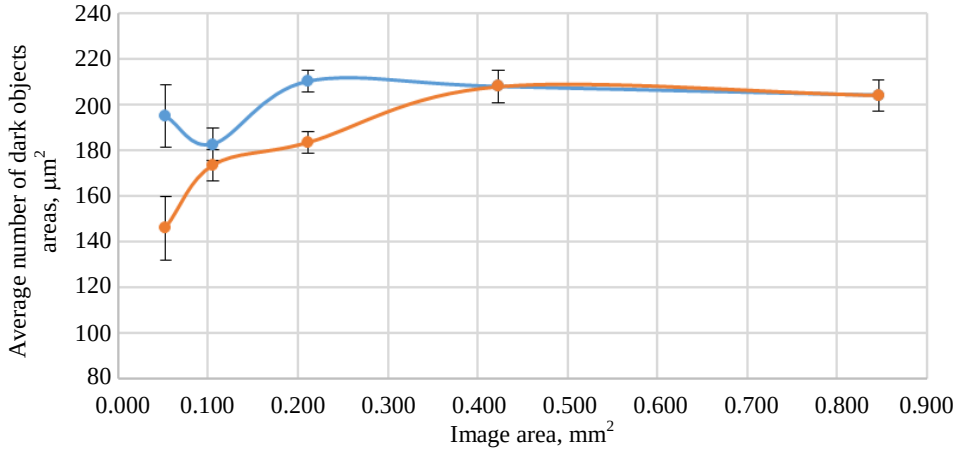

c)

Fig. 7. Variation of average values of the number of nearest neighbors (polyhedras – dark objects) – (a), distances between them (b) and areas of dark objects (c) depending on the measurement scopes for two independent panorama fragments (-●-; -●-)

Conclusion

1. Based on the statistics of distribution of the dark objects areas for the pan view studied in the paper, the noises filtration limit was determined to be 585 μm^2. It was demonstrated that the groups of dark objects outlined by "statistical" (based on areas distribution histograms) and "physical" (based on direct observations of etching pits morphology in the scanning electron microscope) filtration, within "object area *S* – perimeter *P*" coordinates, were consistent with different values of the approximating curves slope angle tangenses: 0.33 and 0.85, respectively. Linearity of the curves reflects the self-similarity of the observed physical phenomena, and the curves parameters reflect the difference in objects nature.

2. To assess non-uniformity of etching pits arrangement on the pan view, partitioning thereof according to Voronoi method was used, followed by assessment of statistics of the distances between dark objects (centers of Voronoi polyhedras) and the number of the nearest neighbors.

3. It was established that it is possible to obtain repeatable measurements results for etching pits morphology and regularity on GaAs Te (100) plates surface with the size of the studied area of 0.42 mm^2 and above (on the sample scale).

REFERENCES

1. Subramanyam N., Tsai C. T., Journal of materials processing technology **55** (3-4), 278–287 (1995). doi: 10.1016/0924-0136(95)02018-7
2. Frigeri C., Weyher J. L., Jimenez J. and Martin P., Journal de Physique III, No. 12, 2339–2360 (1997).
3. Elliot A. G., Wei C. L. and Vanderwater D. A., Journal of Crystal Growth. **85** (1-2), 59 (1987).
4. Yu H. Y., Zhao Y. W., Zhan R., Gao Y. L. and Hui F., J. Semicond. **29** (9), 1775 (2008).
5. Jin C. H., J. Semicond. **34** (6), 063005 (2013). doi: 10.1088/1674-4926/34/6/063005.
6. Oksanich A. P., Shevchenko I. V. and Krasnopol`skaya Yu. A., Avtomatizirovanny`e sistemy` upravleniya i pribory` avtomatiki, No. 156, 16–26 (2011).
7. SEMI M36-0699 Test Method for Measuring Etch Pit Density (EPD) in low dislocation density Gallium Arsenide wafers
8. Sangwal K. Etching of crystals: theory, experiment and application. Elsevier, 2012.
9. http://www.thixomet.com/
10. Komarovsky N. Yu., Zhuravlev E. O., Molodtsova E. V. and Kudrya A. V., Industrial laboratory Diagnostics of materials. **90** (7), 32–39 (2024).
11. Mandelbrot B. B. The fractal geometry of nature / Revised and enlarged edition. New York, 1983.
12. Ozer S. and Besikci C., Journal of Physics D: Applied Physics **36** (5), 559 (2003).
13. Huang M. L., Zheng Z. N., Dai Z. X., Guo X.J., Wang S. S., Jiang L. L., Wei J. C. and Chen S. Y., J. Semicond. **43** (4), 042101 (2022). https://doi.org/10.1088/1674-4926/43/4/042101
14. Belov A. G., Kanevskii V. E., Evgeniya I. K. et al., Modern Electronic Materials. **9** (2), 69–76 (2023).
15. Standard practice for assessing the degree of banding or orientation of microstructures ASTM E1268-01
16. Kudrya A. V., Sokolovskaya E. A., Nihn L. H., Trachenko V. A., Skorodumov S. C., Papina K. B. and Chuong T. H., Frontier Materials & Technologies, No. 4, 44–52 (2014).
17. Martínez J., Hornus S., Song H. and Lefebvre S, ACM Transactions on Graphics. **37** (4), 1–15 (2018). doi:10.1145/3197517.3201343

About authors

Komarovsky Nikita Yuryevich, Head of the research group of the laboratory of high-temperature semiconducting compounds of $A^{III}B^{V}$ group, Sazhin Giredmet JSC (111524, Russia, Moscow, Electronnaya st. 2, bldg. 1). University of Science and Technology MISIS (119049, Russia, Moscow, Leninsky Prospekt, 4, bld. 1). E-mail: nickkomarovskiy@mail.ru nykomarovsky@rosatom.ru https://orcid.org/0000-0002-7869-7886 Scopus Author ID 58510893300. Web of Science Researcher ID NRX-9045-2025. SPIN code: 9642-8920

Kniazev Stanislav Nikolaevich, Ph.D. of Technical Sciences, Head of Laboratory , Sazhin Giredmet JSC (111524, Russia, Moscow, Electronnaya st. 2, bldg. 1). E-mail: stnknyazev@rosatom.ru ORCID: 0000-0002-2580-1707

Sokolovskaia Elina Aleksandrovna, Candidate of Technical Sciences, Associate professor of the Department of the Metallurgical science and Physics of strength, University of Science and Technology MISIS (119049, Russia, Moscow, Leninsky Prospekt, 4, bld. 1). E-mail: sokolovskaya@misis.ru ORCID 0000-0001-9381-9223. Web of Science Researcher ID AAM-6419-2021. Scopus Author ID 15077468100. SPIN code: 2633-6344. AuthorID: 185426

Kudria Aleksandr Viktorovich, Candidate of Technical Sciences, Holder of chair ad interimr of the Department of the Metallurgical science and Physics of strength University of Science and Technology MISIS (119049, Russia, Moscow, Leninsky Prospekt, 4, bld. 1). E-mail: AVKudrya@misis.ru ORCID: 0000-0002-0339-2391. Web of Science ResearcherID GWZ-8579-2022. Scopus AuthorID 6603628218. SPIN code: 6497-2109. AuthorID: 11030

Sukhanova Anna Sergeevna, engineer University of Science and Technology MISIS (119049, Russia, Moscow, Leninsky Prospekt, 4, bld. 1). RD&P Center ORION, JSC (111538, Russia, Moscow, Kosinskaya st., 9). E-mail: sukhanova11@mail.ru SPIN code: 3007-4250. AuthorID: 1245396

Antonova Valeria Evgenievna, Engineer Cat. 2, University of Science and Technology MISIS (119049, Russia, Moscow, Leninsky Prospekt, 4, bld. 1). RD&P Center ORION, JSC (111538, Russia, Moscow, Kosinskaya st., 9). E-mail:avaleriya98@mail.ru

Molodtsova Elena Vladimirovna, Candidate of Technical Sciences, Leading Research Scientist of the laboratory of high-temperature semiconducting compounds of $A^{III}B^{V}V$ group, Sazhin Giredmet JSC (111524, Russia, Moscow, Electronnaya st. 2, bldg. 1). E-mail: evmol@bk.ru ORCID: 0000-0002-2699-9524

PHYSICAL EQUIPMENT AND ITS ELEMENTS

UDC 383 PACS: 42.79.Pw, 85.60.Gz, 07.57.Kp
EDN: VVRYXU

The stand for conducting resource tests in forced modes of a photosensitive element from a space-based photodetector device

D. G. Solovyov[1], V. V. Buravtsova[1], A. A. Krasavin[1], K. D. Kochnov[1,*] and V. B. Kulikov[2]

[1] *RD&P Center ORION, JSC, Moscow, 111538 Russia*
[*] *E-mail: kir.nekko@gmail.com*
[2] *Joint Stock Company "Central Scientific-Research Institute "Cyclone", Moscow, 107497 Russia*

Received 25.08.2025; revised 22.09.2025; accepted 20.10.2025

A stand has been designed for carrying out resource tests in forced modes of a photomodule (FM) of the infrared range (IR) with a temporary hold and accumulation mode (VZN) from a space-based photodetector. A feature of the development is the possibility of obtaining experimental data on failures that occur during prolonged operation of the FM, which affect the threshold characteristics of the device. The stand allows us to confirm the sufficiency of measures to ensure the durability and reliability of the photomodule, as well as to assess the reliability of all equipment used in the whole. The stand will be tested through scheduled tests.

Keywords: stand; photodetector device; photosensitive element.

DOI: 10.51368/2949-561X-2025-5-79-83

Introduction

During development of the Earth remote sensing (ERS) equipment intended for operation in space, the design phase includes reliability calculations and assessments, particularly for the cases involving the ultra-long-term operation during about 10–15 years under the constant influence of space ionizing radiation [1]. Based on these reliability calculations and assessments, as well as the requirements for the ERS equipment, schematic-design and structural design solutions for manufacturing are also determined.

A key component of the ERS equipment are photodetectors operating in the infrared (IR) spectral range. The most promising types of IR photodetectors in terms of reliability and radiation hardness are considered to be scanning-type IR photodetectors incorporating the charge time delay and accumulation (TDA) mode, which use digital-output photomodules (DPMs) as a photodetector. The reliability and radiation hardness of such IR photodetectors is based on the fact that analog-to-digital signal conversion is performed inside the readout large-scale integrated (LSI) circuit which is a part of DPM [2].

The most critical component was identified among the parts of the photodetector under consideration, that is DPM, whose photosensitive elements (PSE) array is composed of HgCdTe (mercury-cadmium-telluride) photodiodes [3]. This paper contains the reliability calculation for the photomodule.

Description of the Measurement Object

The photomodule consists of a Kovar base bearing a multiplexer with 1024 TDA channels. Each channel incorporates a built-in 14-bit analog-to-digital converter connected to a photosensitive element sized (1024×10), topologically organized into four sub-arrays [4, 5]. The photosensitive elements are made of

cadmium-mercury-telluride. Each photomodule generates digital sequences at its outputs, which represent the results of the analog-to-digital conversion of signals from 1024 TDA channels of the multiplexer.

Test Methods

Endurance tests are conducted to develop and verify the reliability of equipment, to identify and eliminate potential design and construction defects that are revealed during long-term operation of the equipment during the service life (assigned lifetime) as per the technical assignment, and to assess (predict) reliability characteristics based on the endurance test results. To shorten the endurance test period for equipment with long mission life of a spacecraft (3 years or more), testing in forced modes is permitted.

Forced endurance test consists of four procedures:

– Procedure 1 – thermal cycling: 1120 hours, consisting of 70 thermal cycles.

– Procedure 2 – low operating temperature exposure test: minus 110 °C, 150 hours, consisting of 3 cycles.

– Procedure 3 – long-term operation of the photomodule at the operating temperature of minus (103±2) °C in "On-Off" mode, 2676 hours, consisting of 2676 "photomodule on" – "photomodule off" cycles.

– Procedure 4 – high temperature exposure test: +35 °C, 604 hours, consisting of 2 cycles.

Test Bench

To perform endurance tests in forced modes of the photomodule being a part of the space-based photodetector, a test bench has been developed that allows evaluating the photomodule's endurance and operational reliability. The bench components (see the figure) include:

– cryostat with a liquid nitrogen cooling system that ensures cooling down the internals to which the photomodule's gauging is attached;

– control and power supply unit consisting of:

1) control unit providing the following:

– monitoring of set values for supply voltages;

– setting the photomodule's operation modes;

– outputting the analog form (for oscilloscope monitoring) of signals representing the sequences of samples of 512 even or 512 odd channels from photomodule's OUT1 and OUT2 outputs;

– outputting the analog form (for oscilloscope monitoring) of signals representing the sequences of samples from one of 512 even or 512 odd channels of the photomodule;

– setting the synchronization mode between the ambient illumination scanner and multiplexer;

– measuring the total current consumed by the photomodule;

– monitoring the photomodule control pulses;

– managing the communication with the host PC.

2) communication unit that ensures the connection between the photomodule equipped with the gauging and the control unit, and monitors its operability, thus enabling the following checks:

– checking the range of photomodule supply and control voltages;

– checking the channel for measuring the total current consumed by the photomodule;

– checking the time-base diagrams of photomodule control pulses;

– checking the channel for outputting the analog information for oscilloscope monitoring;

– checking the integrity of temperature sensor circuits;

– checking the functionality of the USB channel for transmitting the information from the control and power supply unit to PC.

3) cable connecting the control unit to the communication unit;

4) USB cable connecting the control unit to PC;

5) network cable.

– Thermodat-17E6 TD13303625 (designed for simultaneous temperature measurement and adjustment in several channels);

– MATRIX VPS-3005L-3 laboratory power source (used for heating elements (resistors) and maintaining the temperature in the gauging and communication unit);

– AKTAKOM ATH-3335 laboratory power source (used for heating elements

(resistors) and maintaining the temperature in the communication unit);

– MIT 8.03 multi-channel precision temperature meter (designed for precision temperature measurements and thermal field mapping);

– AKIP B7-78/1 multi-purpose voltmeter (allows highly accurate measurement of AC/DC current, resistance, voltage, frequency, and temperature with external sensors);

– Tektronix MDO4054B-3 oscilloscope (enables the time-correlated recording of analog, digital, and RF signals which allows examining the signal and making measurements in both frequency and time domains simultaneously);

– Agilent TPS-mini dry high vacuum turbo molecular pumping system (creates a vacuum inside the cryostat);

– TELEVAK CC-10 electronic vacuum gauge (designed for precise measurement of absolute pressure);

– M305 blackbody module (serves as a radiation source);

– New Focus modulator with control unit, model 3502 (modulates the radiation flux from the blackbody);

– PC;

– software designed to process information from the photomodule and display information frames along with calculated photomodule characteristics on the PC monitor.

DPM is installed in the gauging, which, together with the communication unit, is placed in the cooled zone of the cryostat. Then the pressure inside the cryostat is reduced to ultra-high vacuum (less than 10^{-5} Pa) using a high-vacuum pump, with the pressure level monitored with a corresponding sensor inside the cryostat. After that DPM is cooled with liquid nitrogen to the operating temperature, which is monitored with a corresponding sensor inside the cryostat. For example, the operating temperature is approximately 80 K for the photomodule whose photosensitive elements are photodiodes made of long-wave infrared CdHgTe. Then, power is applied, and initial configuration of DPM is performed via the control and power supply unit [6].

The communication unit is equipped with a temperature sensor and heating resistors (НГ2 and НГ3) designed to maintain the positive temperature on the communication unit.

The cryostat has two zones:

– a hermetically sealed, pumpable zone containing the gauging with the photomodule and communication unit (the cooled zone);

– a zone to be filled with liquid nitrogen (nitrogen chamber)

The gauging with the photomodule in the cooled zone is mounted on a copper plate, which is attached to a heat conductor leading to the nitrogen chamber. To adjust the photomodule temperature, a heating resistor (НГ1) and a temperature sensor (T1), using a platinum sensitive element, ChEPT-50P, are installed on the plate. By changing the current through the heating resistor (НГ1), the specified cooling or heating temperatures for the photomodule are set. The communication unit has no thermal contact with the copper plate. The heat flow from the communication unit to the photomodule travels along the cable that connects them. To maintain the positive temperature on the communication unit during all types of photomodule tests, the unit is equipped with two heating resistors (НГ2 and НГ3) and LN222Pt100 temperature sensor, which outputs the temperature from the communication unit (T4). Additionally, two LN222Pt100 temperature sensors are integrated into the gauging of the photomodule to provide temperatures T2 and T3. The heating resistor (НГ1) is heated by a laboratory source (И1). Control and supply voltages are applied to the photomodule, and its information signals are read off using the communication unit and control unit, which are part of the control and power supply unit. A voltmeter and an oscilloscope connected to the control unit are used to monitor the total consumption current and signals at the photomodule output. In the control unit, the information signals from the photomodule outputs are converted into a single digital stream, which is transmitted via the USB channel to the PC for processing and display. A reduced pressure shall be maintained inside the cryostat for the photomodule ($10^{-6} \div 10^{-4}$ mm Hg), which is created by "Agilent TPS-mini" dry high vacuum turbo molecular pumping system. The pressure inside the cryostat shall be monitored using TELEVAK CC-10 vacuum gauge. The temperature of the communication unit (T4) shall be maintained within the range of (10÷30) °C by

means of heating elements (resistors) НК3, НГ3 and two-channel АКТАКОМ АТН-3335 source. The operating temperature of the photomodule is monitored with three temperature sensors:

– sensor T1 mounted on the plate equipped with the gauging;

– sensors T2 and T3 of LN222Pt100 type mounted inside the gauging.

The temperature sensors providing data for temperatures T2, …, T4 are connected to the four-channel temperature controller (meter) Thermodat-17E6. The values of T2, …, T4 are displayed on the meter's indicator panel and are simultaneously transmitted to the PC via the interface channel created using RS-232/USB converter of MOXA type.

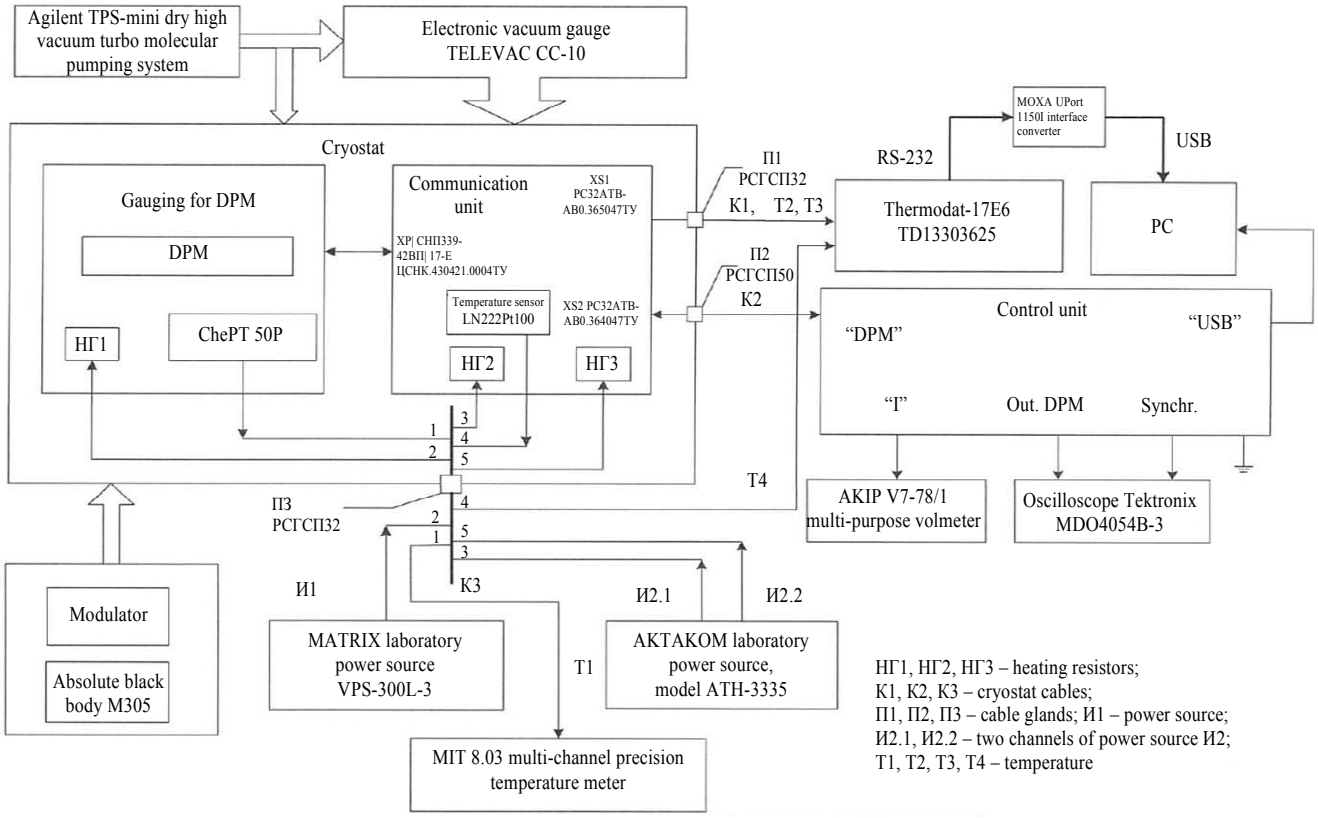

Figure Structural diagram of the test bench

Conclusion

The test bench for forced endurance tests of the photomodule, which is part of the space-based photodetector, enables the detection and elimination of defects and failures during long-term operation of the photomodule, monitoring and verification of sufficient measures to ensure the specified probability of failure-free operation and assigned service life, which is implemented in the forced mode under exposure factors, as well as confirmation of the non-destructive nature of the electrothermal conditioning of the photomodule To validate the reliability assessment conducted in paper [3], the forced endurance tests will be performed at this bench.

REFERENCES

1. Gaponov O. V., Sokolsky M. A. and Romanov E. K., Usp. Prikl. Fiz. (Advances in Applied Physics) **12** (6), 501–530 (2024) [in Russian].
2. Kozlov K. V., Patrashin A. I., Burlakov I. D., Bychkovsky Ya. S., Drazhnikov B. N. and Kuznetsov P. A. (Advances in Applied Physics) **5** (1), 63–78 (2017) [in Russian].

3. Romanov E. K., Burlakov V. I., Chebotarenko D. D. and Yudovskaya A. D. Applied Physics, No. 3, 25–33 (2025) [in Russian].
4. Larionov N. A., Yakimov Yu. A., Moshev I. S., Khrapunov M. L., Streltsov V. A. and Kuznetsov P. A. Abstracts of the XXVI international scientific and technical conference on Photoelectronics and night vision devices. Moscow, 2022, pp. 216–218 [in Russian].
5. Yakimov Yu. A., Larionov N. A. and Kuznetsov A. N. / Proc. X scientific and practical conference of young scientists and specialists "Fotosensorika: novye materialy, tekhnologii, pribory, proizvodstvo". Moscow, 2021, pp. 45–48 [in Russian].
6. Gaponov O. V., Burlakov V. I. and Vlasova O. I. Method for deselecting sequences of excessively noisy elements in the channels of an infrared photosensitive module with a time delay and accumulation mode. Patent for invention No. 2805779 (RF). 2023.

About authors

Soloviev Dmitry Georgievich, Head of Department, RD&P Center ORION, JSC (111538, Russia, Moscow, Kosinskaya st., 9). E-mail: sol.discavery@yandex.ru

Buravtsova Vera Valeryevna, Chief Specialist, RD&P Center ORION, JSC (111538, Russia, Moscow, Kosinskaya st., 9). E-mail: vera_bur@rambler.ru

Krasavin Alexander Aleksandrovich, Lead Engineer, RD&P Center ORION, *JSC* (111538, Russia, Moscow, Kosinskaya st., 9). E-mail: meeting62@inbox.ru

Kochnov Kirill Dmitrievich, engineer, RD&P Center ORION, JSC (111538, Russia, Moscow, Kosinskaya st., 9). E-mail: kir.nekko@gmail.com

Kulikov Vladimir Borisovich, Dr. Sci. (Eng.), Head of Department Joint Stock Company "Central Scientific-Research Institute "Cyclone" (107497, Russia, Moscow, Shchelkovskoe Shosse, 77). E-mail: v.kulikov@cyclone-jsc.ru SPIN code: 2840-0055, AuthorID: 1017695

PHYSICAL EQUIPMENT AND ITS ELEMENTS

UDC 620. 179. 152 PACS: 87.53.Bn
EDN: XMVLOV

Quantitative assessment of the quality of radiographic control, taking into account the specifics of generation and formation of working beams of penetrating radiation

A. S. Dekopov[1], A. A. Lukyanov[1,2,*], S. P. Maslennikov[2] and S. V. Mikhailov[1]

[1] *Joint Stock Company «Energomontazh International», Moscow, 107078 Russia*
[2] *National Research Nuclear University MEPhI, Moscow 115409 Russia*

Received 5.06.2025; revised 27.06.2025; accepted 20.10.2025

The paper presents a quantitative assessment of the quality of radiographic testing taking into account the features of formation of working beams of penetrating radiation by various design versions of deep collimation systems in portable radiographic testing devices of the shutter type equipped with sources based on the radionuclide ^{192}Ir, generating flows of ionizing radiation by focal spots of the emitting working surfaces "bottom" and "side" of the cylindrical capsule of the emitter. Mathematical modeling of the interaction of gamma radiation with elements of deep collimation systems of various geometries was carried out using the MCNP5 and Geant4 software packages. It was found that the use of a pyramidal deep collimation system allows improving the signal-to-noise ratio by approximately two times compared to a rectangular-pyramidal one, which helps to improve the quality of the recorded image and reduce the weight and size characteristics of the equipment. In addition, the orientation of the emitter capsule relative to the "zone of interest" by the focal spot of the emitting region "bottom" slightly increases the contribution of the noise effect and <1 % worsens the parameters of the "signal/noise" factor.

Keywords: deep collimated system; noise effect; signal-to-noise factor; gate-type gamma-ray flaw detector.

DOI: 10.51368/2949-561X-2025-5-84-89

The high quality of the radiographic inspection method, with a relative sensitivity of 1–2 % within a radiation thickness range of up to 70 mm as measured based on the steel, is reliably achieved by using commercial deeply collimated radiographic inspection equipment (RIE) of portable class. This equipment is typically fitted with standard radiation sources based on the radionuclide ^{192}Ir [1].

According to expert estimates, up to 10.000 commercial gamma-ray flaw detectors are in industrial operation in the Russian Federation at shipbuilding facilities, chemical, oil & gas, and petrochemical plants, as well as in the power generation sector.

The portable shutter-type gamma-ray flaw detector of "Stapel" series [2] developed by JSC "NIITFA" to adapt to confined installation and repair conditions and equipped with a deep collimation system has become widely used.

The experience of using this RIE at shipbuilding enterprises has resulted in a hypothetical that the best sensitivity of the inspection method under conditions of deep collimation of the frontal radiation beam is achieved with standard radiation sources oriented towards an object under inspection solely with the emitting area of the bottom working surface of the cylindrical source capsule.

This hypothesis was preliminarily studied and evaluated using hole-type image quality indicator No. 2 (according to GOST 7512-82) at a shipbuilding enterprise under standard conditions for recording the macrostructure of welded joints.

The actual results from the reference quality assessment of radiographic inspection on real objects did not allow for favoring either coordinate system for focal spots of emitting areas (capsule "side" or "bottom"), with the source capsule oriented with its bottom or side surface relative to the "region of interest".

In this regard, the practical experience of radiographic inspection using the mentioned RIE and analysis of the structural design of the collimated radiation beam shaper in shutter-type gamma-ray flaw detectors suggests that a different approach is needed to study this issue by accounting for the specifics of shaping deeply collimated working radiation beams, for example, through quantitative assessment of radiation conversion effects and generation of scattered radiation noise flux (Iф), which negatively affects the method's sensitivity, and the unscattered radiation flux (Iп) carrying the useful information, in a digital format.

In this context, considering the different physical capabilities for transforming the primary radiation flux by deep collimation systems of various structural designs, a quantitative assessment of the achievable inspection quality is advised by using digital technologies based on the "signal-to-noise" factor (Iп/Iф), which will allow for evaluating the degree of image blurring caused by imperfections in the collimator's design solutions, the use of filters, as well as of radiation sources with non-standard activated core dimensions, including the geometric orientation of the source capsule within the system.

Thus, this paper is focused on establishing the "signal-to-noise" factor in relation to different deep collimation systems (pyramidal-rectangular, Fig. 1 (A1-A1) and pyramidal, Fig. 1 (A2-A2)) under the above described conditions of exposure with focal spots of "side" and "bottom" emitting areas of the cylindrical source capsule.

The radiographic inspection system for this case is presented in detail in Figure 1.

The interaction of photons from the ^{192}Ir radionuclide source [4] with the system components and the quantitative determination of Iф and Iп fluxes registered by the film-emulsion detector [5] were implemented using the Monte Carlo mathematical modeling method with the MCNP5 software package according to the calculation model accounting for the coordination of focal spots in the "bottom" and "side" positions within the system as applied to the cases of using the Pb filter and radiation sources , including those with non-standard activated core dimensions. The materials specified in the calculation model are: protection unit based on uranium-238, source holder made of VNZh-95 alloy, source capsule and socket bushing of the protection unit made of stainless steel 12Kh18N10T, and the active part based on ^{192}Ir.

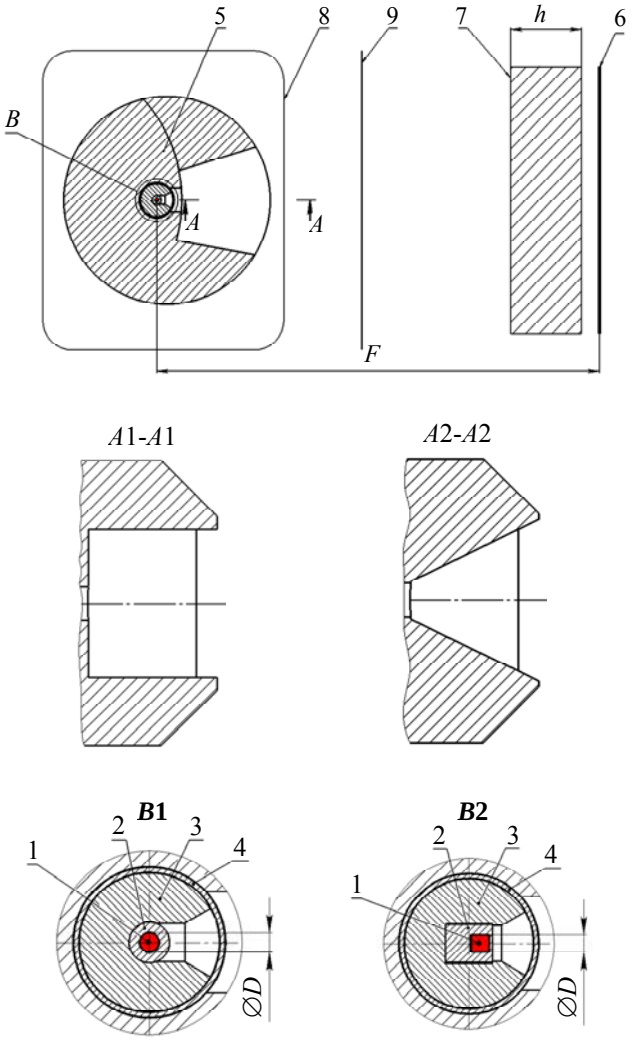

Fig. 1. Simplified radiographic inspection system: A1-A1 – cross-sectional view of the pyramidal-rectangular deep collimation system; A2-A2 – cross-sectional view of the pyramidal deep collimation system; B1 – focal spot of the "side" emitting area; B2 – focal spot of the "bottom" emitting area; 1 – active part of the radiation source; 2 – source capsule; 3 – source holder; 4 – sleeve; 5 – protective-collimation unit with a shutter; 6 – film detector; 7 – object under inspection; 8 – housing of the manual radiation beam coordination system; 9 – Pb filter

The modeling results accounting for the "signal-to-noise" using MCNP5 software package are presented in the table.

Visualized representations of the registered gamma-ray flux distributions for various structural designs of deep collimation systems were implemented by using Geant4 software package [6]. The modeling involved initiating 3.7×10^8 decay events applied to the radiation source based on the radionuclide ^{192}Ir, with an active part sized ∅1.5×1.5 mm and a focal length of 150 mm, followed by plotting flux distributions (Fig. 2) in the MATLAB environment and curves of flux intensity distribution along X and Y axes, without considering the contribution of scattered radiation (Fig. 3).

Figure 2 shows track maps of gamma-quantum distributions at the focal length of 150 mm, depending on the deep collimation system geometry.

The maximum size of the region of interest is 150×150 mm at the focal length of 150 mm, according to the Operation Manual for equipment of the "Stapel5 Se75 Ir192" type incorporating the deep collimation system.

The experiments in this paper used the portable shutter-type gamma-ray flaw detector "Stapel" equipped with the deep collimation system [2].

Table

Source of ionizing radiation Ir192 TU95.930-82	**Signal-to-Noise Factor**			
	Orientation of the emitting working surface: "side". Rectangular-pyramidal collimator	**Orientation of the emitting working surface: "bottom". Rectangular-pyramidal collimator**	**Orientation of the emitting working surface: "side". Pyramidal collimator**	**Orientation of the emitting working surface: "bottom". Pyramidal collimator**
Active part size of the source of ionizing radiation ∅1.5×1.5 mm	22.411 ± 0.0041	22.199 ± 0.0044	47.539 ± 0.0054	47.216 ± 0.0053
Active part size of the source of ionizing radiation ∅1.5×1.5 mm with 0.1 mm filter	21.619 ± 0.0054	21.411 ± 0.0053	46.964 ± 0.0073	46.463 ± 0.0073
Active part size of the source of ionizing radiation ∅1.5×1.7 mm	21.622 ± 0.0041	21.404 ± 0.0044	46.959 ± 0.0053	46.461 ± 0.0053
Active part size of the source of ionizing radiation ∅1.5×1.7 mm with 0.1 mm filter	21.431 ± 0.0053	21.167 ± 0.0053	46.714 ± 0.0074	45.963 ± 0.0073

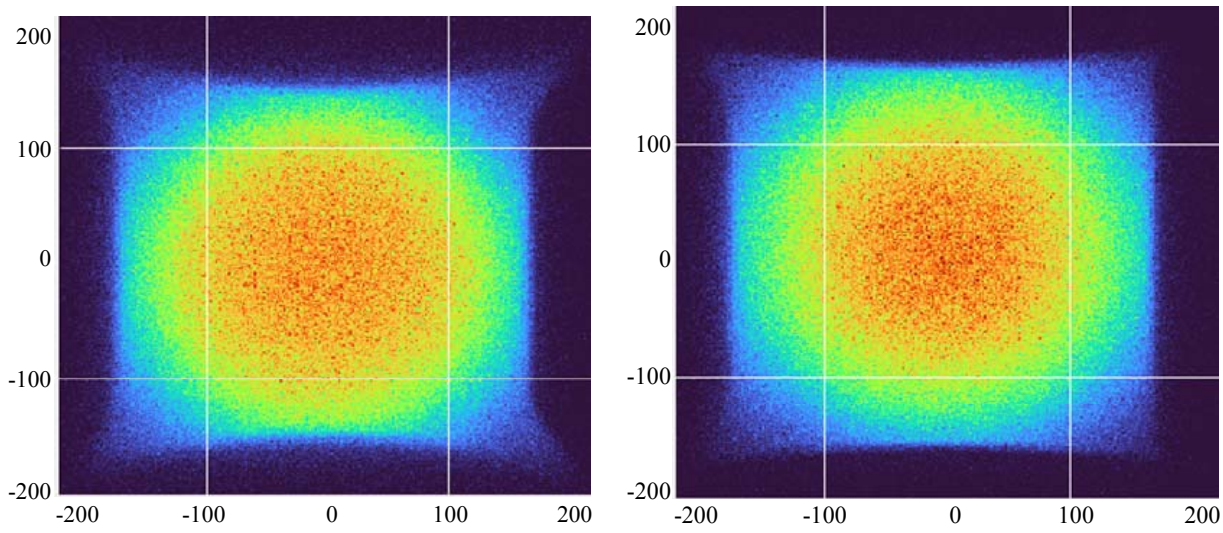

Fig. 2. Distributions of direct and scattered gamma-ray photon fluxes by deep collimation systems: a) – pyramidal-rectangular; b) – pyramidal.

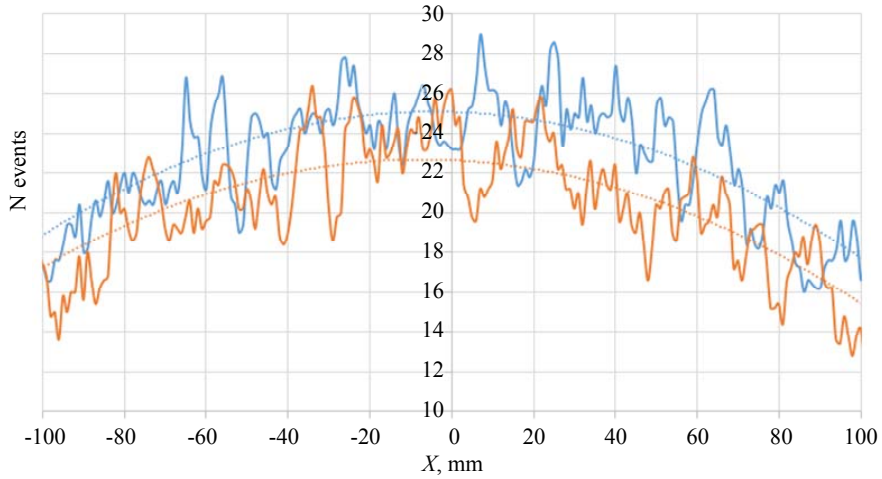

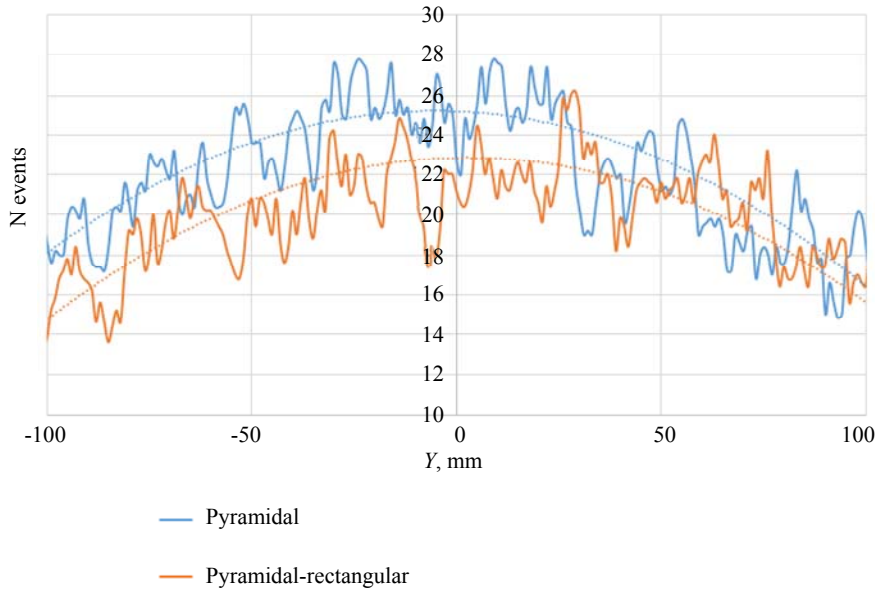

Fig. 3. Curves of flux intensity distribution along axes

The maximum size of the region of interest is 150×150 mm at the focal length of 150 mm, according to the Operation Manual for equipment of the "Stapel5 Se75 Ir192" type incorporating the deep collimation system.

The experiments in this paper used the portable shutter-type gamma-ray flaw detector "Stapel" equipped with the deep collimation system [2].

During testing of the specified commercial RIE in the confined conditions of the inspection zone, a key operational shortcoming was identified, which is the low precision in coordinating the conditional geometric axis of the collimated radiation beam with the center of the "region of interest" on the object under inspection. This negatively impacts the quality of recorded information due to the high probability of the irradiation zone shifting outside the "region of interest", registering effects of backscattered radiation from adjacent structures, and increasing radiological hazards associated with higher radiation exposure to personnel and environment.

For this reason, JSC "EMI" has developed a patented technical solution (Patent No. 2791427) [7] for the updated model of the shutter-type gamma-ray flaw detector, which provides visualized coordination of the aiming trajectory for the center of the working gamma-ray beam in manual mode relative to the center of the "region of interest" on the object under study, which is marked with a point. This technical solution is implemented by modifying the standard foldable carrying handle equipped with a sharp-focus laser generator for the operator to perform visualized guidance of the virtual geometric axis of the directional path the gamma-ray beam by aligning the point projection of the narrow-directional laser beam with the marked center of the "region of interest" on the object under study.

Conclusions

1. The calculated data for the "signal-to-noise" factor obtained using software packages indicate: the pyramidal deep collimation system improves the "signal-to-noise" ratio by ≈2 times (see the table) compared to the rectangular-pyramidal system, which should result in reduced image blurring.

2. According to the calculated data (table), the 0.1-mm thick Pb filter does not reduce the contribution of the noise effect.

3. Orienting the source capsule relative to the "region of interest" with the focal spot of the "bottom" emitting area slightly increases the noise contribution and degrades the "signal-to-noise" factor parameters by < 1% due to internal self-absorption. Therefore, orientation with the focal spot of the "side" or "bottom" emitting area is inconsequential.

4. The pyramidal deep collimation system allows reducing the weight of the shutter assembly by ≈1.4 times, thereby increasing its resistance to dynamic loads during emergency transportation.

5. The intensity of the direct unscattered radiation flux of the pyramidal deep collimation system is higher along *X* axis by 1.11 times and along *Y* axis by 1.1 times, as can be seen from the curves in Fig. *3*.

6. Original technical solution No. 2791427 has been developed to enable the coordination of the virtual geometric axis of the collimated radiation beam relative to the "region of interest" in order to increase the precision and reduce noise effects from backscattered radiation.

REFERENCES

1. TU95.930-82 Sealed emission sources based on iridium-192 radionuclide. Technical conditions.
2. Khoroshev V.N. et al., Gamma detector. Patent No. 2418290 (RF). 2011.
3. MCNP. Electronic resource: URL: https://mcnp.lanl.gov/manual.html
4. IAEA Nuclear Data Section. Electronic resource: https://www-nds.iaea.org/relnsd/vcharthtml/VChartHTML.html
5. Dekopov A. S. Research of methods of radiographic testing of ring welded joints of nuclear reactor units: diss. Candidate of Technical Sciences. M., 2012.
6. Agostinelli S., Allison J., Amako K. et al., Nucl. Instrum. Meth. A **506**, 250–303 (2003).
7. Decopov A. S. et al. Gamma-defectoscope of shutter type. Patent No. 2791427 (RF). 2023.

About authors

Dekopov Andrey Semyonovich, Cand. Sci. (Eng.), Honored Worker of the Nuclear Industry, Consultant Joint Stock Company «Energomontazh International» (107078, Russia, Moscow, 3 Krasnovorotsky Proezd, bld. 1). E-mail: 16deko29@mail.ru AuthorID: 647102

Lukyanov Alexander Andreyevich, Postgraduate Student Joint Stock Company «Energomontazh International» (107078, Russia, Moscow, 3 Krasnovorotsky Proezd, bld. 1). National Research Nuclear University MEPhI, (115409, Russia, Moscow, 31 Kashirskoe Shosse). E-mail: lukyanov_a_a@bk.ru SPIN code: 9321-1309, AuthorID: 1215288

Maslennikov Sergey Pavlovich, Dr. Sci. (Eng.), Associate Professor National Research Nuclear University MEPhI, (115409, Russia, Moscow, 31 Kashirskoe Shoss). E-mail: spmaslennikov@mephi.ru SPIN code: 8452-5020, AuthorID: 113692

Mikhailov Sergey Vladimirovich, Head of Special Design Bureau Joint Stock Company «Energomontazh International» (107078, Russia, Moscow, 3 Krasnovorotsky Proezd, bld. 1). E-mail: svm@jscemi.ru

PHYSICAL EQUIPMENT AND ITS ELEMENTS

UDC 533.9 PACS: 52.50.Dg
EDN: XYOEUW

Experimental setup for microwave plasma modification of dispersed materials at atmospheric pressure

V. N. Tikhonov[1], S. N. Antipov[2,*], I. A. Ivanov[1], A. V. Tikhonov[1], M. Kh. Gadzhiev[2], M. V. Il'ichev[2] and A. S. Tyuftyaev[2]

[1] *Institute of Radiology and Agroecology of National Research Centre «Kurchatov Institute», Kaluga Region, Obninsk, 249035 Russia*
[2] *Joint Institute for High Temperatures of Russian Academy of Sciences, Moscow, 125412 Russia*
[*] *E-mail: antipov@ihed.ras.ru*

Received 25.06.2025; revised 16.07.2025; accepted 20.10.2025

An experimental setup based on a waveguide-type microwave plasmatron has been developed to study plasma-assisted modification of dispersed materials (loose powders) in an electrodeless microwave discharge at atmospheric pressure in a gas flow. Devices (installation modules) have been developed for the formation of a vortex gas flow and controlled injection of dispersed particles into a microwave discharge. Preliminary experiments have been conducted on the treatment micron-sized SiO_2, MgO, and polytetrafluoroethylene (PTFE) particles in a microwave discharge in an argon flow. Particle analysis has been performed using scanning electron microscopy (SEM). In the case of oxide materials, it has been shown that microwave plasma treatment can lead to particle agglomeration and spheroidization. The experimental complex developed, combined with the use of various working gases, provides a versatile platform for plasma modification of dispersed particles across a wide range of sizes and material compositions.

Keywords: microwave plasmatron; atmospheric pressure microwave discharge; plasma modification; dispersed materials.

DOI: 10.51368/2949-561X-2025-5-90-95

1. Introduction

Modern technological advances in functional materials, nanotechnology, and powder metallurgy present researchers with the challenge of developing highly efficient and versatile methods for modifying the properties of dispersed materials. In this context, the use of plasma technologies is of particular interest, as they provide a wide range of thermodynamic and chemical conditions for influencing microparticles.

Plasma modification of loose powders enables changing their physicochemical properties, including the morphology, phase composition, crystalline lattice structure, as well as the formation of functional coatings on particle surfaces. This opens the way to creating new materials with specified properties in high demand across various scientific and technical fields – from catalysts to composites. For example, plasma modification of powders reveals new possibilities of using it to develop new dispersed composite materials (DCM), where solid microparticles are used as a filler that imparts new properties to the matrix material. Modifying filler properties by means of plasma allows adjusting the chemical resistance, thermal stability, thermal and electrical conductivity, and other characteristics of DCM. One of the most promising directions in this area is the application of the microwave (MW) plasma characterized by

high energy density, non-equilibrium nature, and the ability to effectively control discharge parameters [1–10]. In addition to the physical impact (heating, evaporation, etc.), the microwave plasma provides an active chemical environment due to the presence of excited atoms and radicals, thus enabling changes in the surface structure as well as the deposition of various (oxide or nitride) coatings. It should be noted that despite the diversity of active particles generated in the plasma, their impact on materials is confined to a very thin surface layer, typically less than 1 μm thick. Thus, all effects of plasma material treatment are determined by a set of physicochemical processes initiated by the plasma's active particles in this thin surface layer. However, when treating such materials as micropowders, the modified layer can constitute a significant portion of the entire microparticle's volume.

At the current stage of development of this field, one of the key challenges remaining is to design the experimental setups that ensure reliable and reproducible mode for plasma treatment of particles with various sizes and chemical compositions. Electrodeless microwave discharges operating at the atmospheric pressure offer several advantages: simple implementation, stability, and absence of electrodes, which eliminates a source of erosion and contamination. They allow localizing the plasma formation region and act on dispersed materials in a targeted manner. Furthermore, the ability to use various gases (inert gases, nitrogen, air, etc.) allows for flexible adjustment of the plasma medium's composition depending on the required technological outcome. Nevertheless, the practical implementation of effective treatment of dispersed particles by gas-discharge plasma requires solving a number of technical challenges, including gas flow formation and controlled particle injection. To enhance modification efficiency, it is crucial to ensure uniform particle distribution within the discharge volume and to minimize aggregation or settling. A vortex gas flow combined with injection systems can serve as a solution to this task, enabling simultaneous particle transport and dispersion in the zone of maximum concentration of active plasma components.

This paper presents the experimental setup that implements an approach for plasma modification of dispersed materials at the atmospheric pressure using a waveguide-type microwave plasmatron and devices for feeding the plasma-supporting gas mixed with the powder to be processed. Technical solutions are proposed for forming a stable vortex flow of the plasma-supporting gas and controlling particle dosing modes into the microwave discharge region to ensure effective plasma treatment. Particular attention is given to the versatility of the setup, enabling the treatment of a wide range of powder materials of diverse natures.

2. Microwave Plasmatron and Systems for Gas and Powder Delivery into the Microwave Discharge

The experimental setup was built based on the previously developed magnetron-based waveguide-type microwave plasmatron installed on the test bench for studying electrode-free atmospheric-pressure microwave discharge [11–14]. The microwave plasmatron consists of two units: the microwave generator and high-voltage power supply unit that permanently connected by a 2-m high-voltage cable bundle housed in a protective corrugated metallic conduit.

Technical specifications of the microwave plasmatron:

– power supply voltage of the magnetron – 4.45 kV,
– anode current – 0.4–0.9 A,
– filament voltage – 3.15 V,
– filament current – 11 A,
– output power adjustment – 1.5 to 2.5 kW, level 3,
– power supply unit cooling – air-cooled,
– microwave unit cooling – water-cooled, min. 0.9 l/min,
– transformer overheat protection – thermal relays on cores,
– power supply unit dimensions (L×W×H) – 500×220×400 mm,
– microwave unit dimensions (L×W×H) – 370×170×270 mm,
– power supply unit weight – max. 27 kg,
– microwave unit weight – max. 6 kg.

The experimental setup also includes:

– microwave circulator with the operational power up to 5 kW,
– matched waveguide water loads,

– wide range of waveguide transmission line components.

A device for injecting dispersed particles into the microwave discharge region was developed and manufactured for the purpose of plasma modification of loose powders in atmospheric-pressure microwave plasma in the gas flow. When introducing powders into the discharge, several characteristics of atmospheric-pressure microwave discharge shall be considered. To maintain discharge stability and isolate it from the discharge chamber walls, various schemes for "swirling" the gas jet are typically used. However, in this case, when solid particles are introduced into the gas flow, they are centrifugally thrown from the central region towards the chamber wall. The effectiveness of plasma impact on the particle surfaces is low. Figure 1 shows a scheme of the gas flow former, which allows constructing a microwave plasmatron where the tangential component of the gas flow velocity can be arbitrarily small. This is achieved by either rotating working gas supply tubes with a curved outlet or by using straight tubes. Discharge stability in this case is ensured due to the velocity jump and flow vorticity behind the cone's edge, which acts as a bluff body (poorly streamlined). Several versions of gas flow generators enabling the injection of dispersed powders into the plasma and featuring glass and ceramic hollow, as well as Teflon and combined designs, were manufactured and tested.

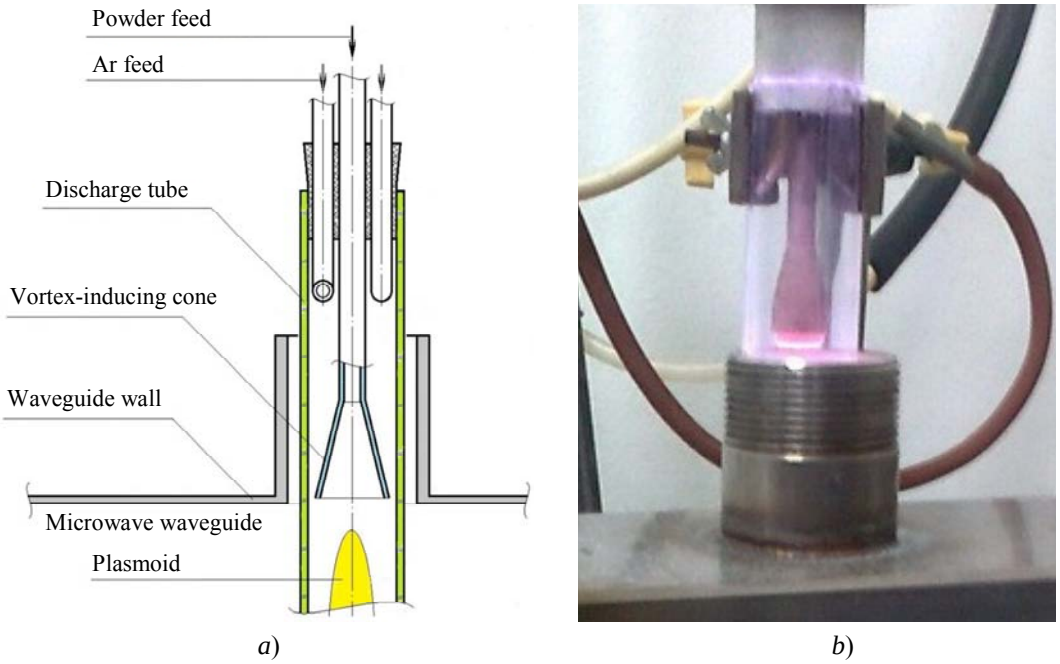

Fig. 1. Scheme of the gas flow former with a bluff body – a vortex-inducing cone (a) and its test prototype during a powder feeding experiment (b)

The next stage in developing the device for injecting micropowders into the plasma was to design a micro-dosing feeder. A pyramidal receiving storage hopper equipped with an adjustable pneumatic vibrator was designed and manufactured (Fig. 2*a*). The feeding single-flighted screw auger is driven by a motor, the speed of which can vary using a supply voltage frequency converter.

The undesirable escape of the feed gas through the screw auger was prevented by maintaining a sufficient powder layer thickness in the receiving hopper.

Three polydisperse powders were processed: SiO_2 and MgO oxides, and polytetrafluoroethylene (PTFE) particles. High-purity argon (99.998 %) was used as the plasma-forming gas. The gas flow rate during processing was 25 l/min for the oxides and 15 l/min for PTFE. The microwave power delivered to the discharge was approximately 1 kW.

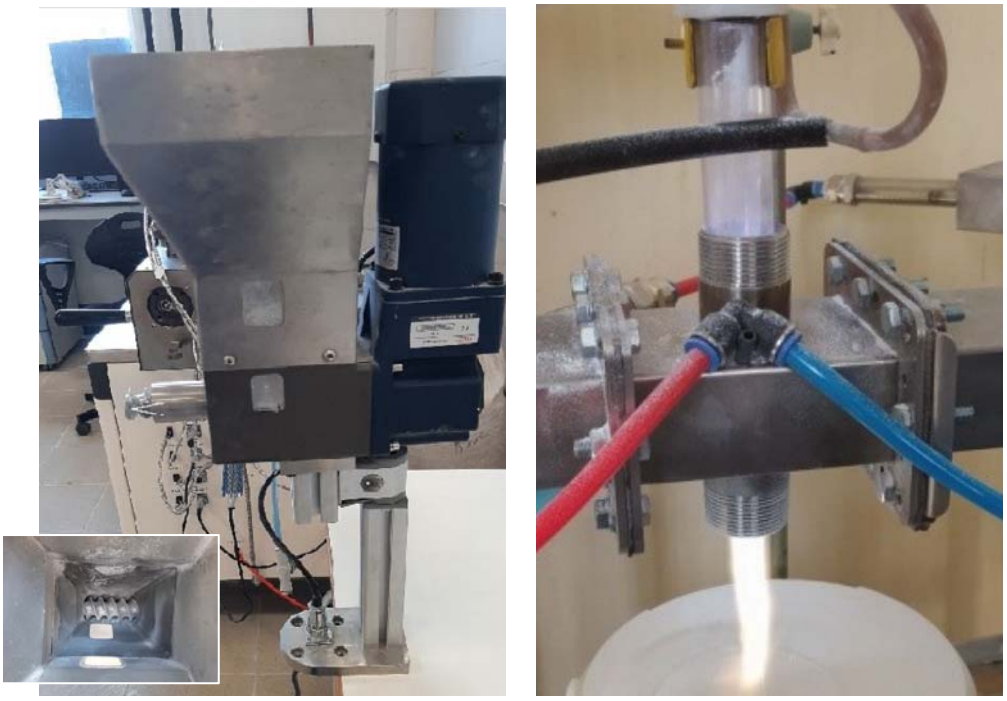

a) *b)*

Fig. 2. Micro-dosing feeder for loose materials (a) and a photograph of the experiment on plasma treatment of particles in a microwave discharge within in the gas flow (b). The insert shows the screw auger at the hopper bottom (top view)

3. SEM Analysis of Treated Powder Microparticles

The morphology and elemental composition of the treated powders were analyzed using the scanning electron microscopy (SEM) method. Our research was performed using JEOL scanning electron microscope with the accelerating voltage of 0.5 to 20 kV. The electron-optical system of the microscope allows imaging with maximum magnification of ×100.000. The spatial resolution with a 20 kV electron beam in high vacuum mode was 4 nm. The microscope is equipped with a highly efficient secondary electron detector and a compact, cost-effective energy-dispersion spectrometer enabling the spectral mapping and elemental analysis at individual points. Additionally, the microscope is fitted with a sputter coating device for pretreating of non-conductive samples prior to SEM scanning.

The results of electron microscopy for MgO powder particles at ×10.000 magnification are shown in Fig. 3. Before being treated with the plasma most particles are seen to have a "flake-like" appearance of a highly asymmetric, fragmented (scaly or needle-like) shape, less than 1 μm thick and several microns long. After treatment, the powder contains larger, symmetric, rounded particles approximately 10 μm and larger in size. Thus, it can be stated that the microwave plasma treatment results in agglomeration of MgO particles through sintering and subsequent spheroidization.

For the SiO_2 powder changed its particle size distribution after plasma treatment. The reference powder (before treatment) consisted of roughly spherical particles featuring a coarse fraction of 10–50 μm, "sprinkled" with smaller particles by an order of magnitude. As a result of plasma treatment, this smaller fraction became predominant. The particles were observed to acquire a more symmetric and smooth (rounded) shape, while the degree of “sprinkling” decreased. In this case, we can also speak of particle spheroidization in the microwave discharge plasma, which seems to be caused by melting of particle surfaces.

As for PTFE particles, the analysis conducted did not reveal significant changes in their morphology as a result of exposure to the microwave discharge under the applied treatment

modes. This is likely due to the high chemical inertness of PTFE, its low surface energy, and thermal stability, which hinder the effective interaction with plasma's active components at the given discharge parameters. This result emphasizes the need to optimize the treatment modes (for instance, by increasing microwave power, extending the treatment time, or using reactive gases) to achieve noticeable plasma effects on PTFE.

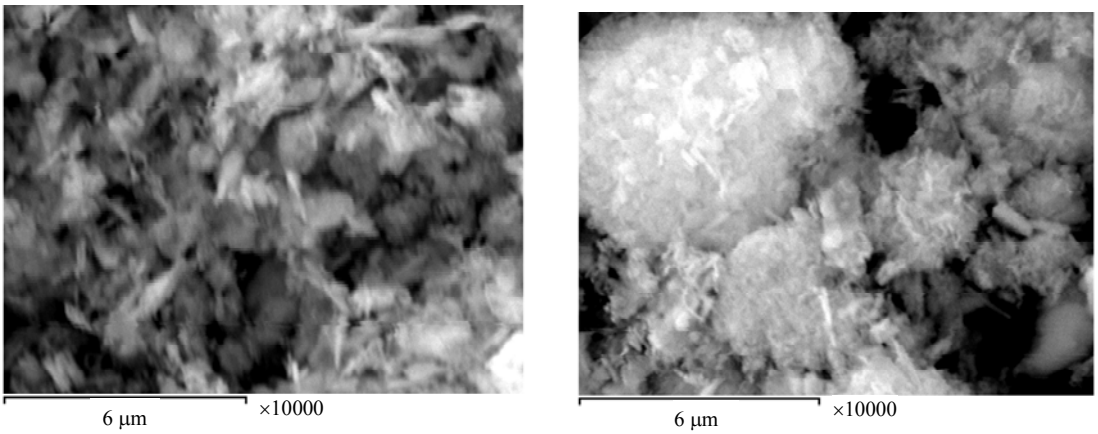

a) *b)*

Fig. 3. SEM photos of MgO particles at ×10,000 magnification before (a) and after (b) microwave plasma treatment

4. Conclusion

The experimental setup for studying the microwave plasma modification of dispersed materials, which is described in this paper, was designed on the basis of the existing test bench equipped with a previously developed waveguide-type microwave plasmatron that was supplemented with specially designed modules for feeding the working gas and dispersed particles into an electrode-free atmospheric-pressure microwave discharge – a vortex gas flow former, a micro-dosing feeder, a screw auger, and a mixer of powders with working gas.

Micron particles of three materials were treated with plasma: SiO_2 and MgO oxides, and PTFE particles. Analysis of particle morphology by the scanning electron microscopy for the oxides revealed that plasma treatment results in particle agglomeration (which is more pronounced for MgO) and spheroidization thereof due to melting. Although the treatment of PTFE particles did not yield a substantial effect, selecting optimal processing parameters (microwave power, treatment duration, etc.) and plasma-supporting gases to achieve this effect is the goal of further research.

The designed experimental setup is highly multi-purpose and represents the in-demand tool for developing microwave plasma methods for obtaining new dispersed, materials with special functional properties, including composites.

REFERENCES

1. Reza M., Setiawan K. M., Steky F. V., Nugroho F. G., Agusta M. K., Indarto A. and Suendo V., Colloids and Surfaces A: Physicochemical and Engineering Aspects **694**, 134134 (2024).
2. Ma Z., Ouyang B. and Zuo X., Journal of Adhesion Science and Technology **38** (24), 4507–4525 (2024).
3. Szabó D. V. and Schlabach S., Inorganics **2** (3), 468–507 (2014).
4. Szabo D. V., Vollath D. and Arnold W., Ceramic Transactions (USA) **111**, 217–224 (2000).
5. Wojnarowicz J., Chudoba T. and Lojkowski W., Nanomaterials **10** (6), 1086 (2020).
6. Hossain F. et al., Renewable and Sustainable Energy Reviews **202**, 114650 (2024).
7. Van Laar J. H. et al., Journal of the Southern African Institute of Mining and Metallurgy **116** (10), 941–946 (2016).
8. Didenko A. N., Prokopenko A. V. and Smirnov K. D., Izvestiya RAN. Energetika, No. 3, 144–150 (2012) [in Russian].

9. Kutepov A. M., Zakharov A. G. and Maksimov A. I. Vacuum-plasma and plasma-solution modification of polymer materials. Moscow, Nauka, 2004 [in Russian].
10. Hunke H., Soin N., Shah T. H. et al., Materials **8** (5), 2258 (2015).
11. Tikhonov V. N., Aleshin S. N., Ivanov I. A. et al., Journal of Physics: Conference Series **927** (1), 012067 (2017).
12. Tikhonov V. N., Ivanov I. A. and Tikhonov A. V., Applied Physics, No. 4, 123 (2018) [in Russian].
13. Ivanov I. A., Tikhonov V. N. and Tikhonov A. V., Journal of Physics: Conference Series **1393** (1), 012042 (2019).
14. Tikhonov V. N., Gorbatov S. A., Ivanov I. A. et al., Journal of Physics: Conference Series **2064** (1), 012131 (2021).

About authors

Tikhonov Viktor Nikolaevich, researcher Institute of Radiology and Agroecology of National Research Centre «Kurchatov Institute» (249035, Russia, Kaluga region, Obninsk, Kievskoye Highway, 1, bldg. 1). E-mail: v.n.tihonov@yandex.ru SPIN code: 2888-3451, AuthorID: 27078

Antipov Sergey Nikolayevich, Cand. Sci. (Phys.-Math.), Research Scientist Joint Institute for High Temperatures of Russian Academy of Sciences (125412, Russia, Moscow, Izhorskaya st., 13, bldg. 2). E-mail: antipov@ihed.ras.ru SPIN code: 6324-4441, AuthorID: 40329

Ivanov Igor Anatolyevich, researcher Institute of Radiology and Agroecology of National Research Centre «Kurchatov Institute» (249035, Russia, Kaluga region, Obninsk, Kievskoye Highway, 1, bldg. 1). SPIN code: 6969-7420, AuthorID: 783821

Tikhonov Aleksander Viktorovich, Junior Researcher Institute of Radiology and Agroecology of National Research Centre «Kurchatov Institute» (249035, Russia, Kaluga region, Obninsk, Kievskoye Highway, 1, bldg. 1). E-mail: ti_@list.ru SPIN code: 4479-1819, AuthorID: 989747

Gadzhiev Makhach Khairudinovich, Cand. Sci. (Phys.-Math.), Head of the Laboratory Joint Institute for High Temperatures of Russian Academy of Sciences (125412, Russia, Moscow, Izhorskaya st., 13, bldg. 2). E-mail: makhach@mail.ru SPIN code: 2169-8355, AuthorID: 605045

Ilyichev Maksim Valeryevich, Candidate of Technical Sciences, researcher Joint Institute for High Temperatures of Russian Academy of Sciences (125412, Russia, Moscow, Izhorskaya st., 13, bldg. 2). E-mail: imvpl@mail.ru AuthorID: 185149

Tyuftyaev Alexander Semyonovich, Doctor of Technical Sciences, Senior Researcher Joint Institute for High Temperatures of Russian Academy of Sciences (125412, Russia, Moscow, Izhorskaya st., 13, bldg. 2). E-mail: astpl@mail.ru SPIN code: 5341-2934, AuthorID: 40635

For the 80th anniversary of Iurii Anatolevich LEBEDEV

November 11, 2025, marks the 80th anniversary of the famous Russian scientist, Doctor of Physical and Mathematical Sciences, editorial board member of the “Applied Physics” journal **Iurii Anatolevich Lebedev**.

Iu. A. Lebedev was born on November 11, 1945, in 1968 he graduated from the Faculty of Electronics of the Moscow Institute of Petrochemical and Gas Industry, and in 1973 he graduated from the physics department of the Lomonosov Moscow State University, in 1997 he passed the Ph.D. Defense, and in 1993 he defended the doctoral thesis in the “Plasma physics” specialty. He worked his way up from an engineer in one of the design bureaus to the Head of the Laboratory and Chief Scientific Officer of the Topchiev Institute of Petrochemical Synthesis (RAS).

Iu. A. Lebedev is a well-known specialist in the field of physics of low-temperature plasma and gas discharges, plasma chemistry, plasma generation methods, plasma diagnostics and simulation. Iu. Lebedev published about 500 scientific publications, including monographs and textbooks. Iurii Anatolevich is a Deputy Chairman of the Scientific Council of RAS in the field of low-temperature plasma, board member of the Low-temperature Plasma Encyclopedia and several scientific journals, member of several Dissertation Councils, member of International Scientific Committee on the problem of “Microwave discharge: fundamentals and application”.

Over the years of work, Iurii Anatolevich has been awarded a number of national and international awards. He is an Honored Worker of Science and Technology of Moscow, honored employee of the Institute of Petrochemical Synthesis RAS, was awarded the 300th anniversary of the Russian Academy of Sciences medal, in 2018, was awarded the “Outstanding reviewer” diploma for the Journal of Physics D: Applied Physics (“IOP Publishing” publishing house).

Editors and editorial board of “Applied Physics” sincerely appreciate you, Iurii Anatolevich, for creative participation in the development of our publication as a valued member of its board. Together with your numerous colleagues, friends and students we congratulate you on your anniversary and wish you good health, fruitful scientific activity, success and good luck in achieving new results.

INFORMATION

Rules for submission, reviewing and publishing of scientific papers

(as revised in 2025)

1. The "Applied Physics" journal is mainly intended for urgent publication of short papers concerning recent achievements in physics that have a potential of applied (technical and scientific) use. The journal is included in the new List of the Higher Attestation Commission, which came into effect on December 1, 2015.

By sending the article manuscript to the journal's editorial board, the authors grant the editorial board, founder and publisher of the journal a free, non-exclusive right to publish it in Russian as an article in the printed version of the journal, in the electronic version of the journal in the Internet and on laser disks. At the same time the authors retain their intellectual rights to the article manuscript (including "copyright"). In this regard and considering Part Four (Section VII) of the Civil Code of the Russian Federation, the authors shall submit a letter to the editor in the following form:

License agreement for transfer of the publish right (publishing license agreement)

We, the undersigned, the manuscript authors _____,
grant the editorial board, founder and publisher of "Applied Physics" journal a free, simple (non-exclusive) license to publish the article manuscript in both printed and electronic journal versions.

We confirm that this publication does not violate the intellectual rights of other persons or organizations. Signatures of authors: _____ (full name, academic degree, date)

The article shall be signed by all authors. If there are several authors, the name of the author responsible for message exchange with the editorial board shall be indicated. The article manuscript shall be sent to the address of the journal's editorial board: 111538, Moscow, Kosinskaya st, 9, AO NPO Orion, editorial board of "Applied Physics" journal or by e-mail: advance@orion-ir.ru

2. The article manuscript shall be submitted to the editor only in Russian.

3. The article manuscript shall be accompanied by an expert opinion whether its publication in the open media is allowed, which shall be drawn up in accordance with the established procedure.

4. The article size (including figures, bibliography and the English-language part) shall not exceed **7 pages** of A4 format with single line spacing. (A larger article is proposed to be sent to the affiliated **"Applied Physics Advances"** journal intended for publication of detailed articles and reviews). The article material shall be submitted in printed form (on paper) and in electronic form on a CD/DVD disk with the text in Word format (font type – Times New Roman, font size – 12), and the text shall already include figures with captions under them in the proper places. However, overly detailed and cumbersome mathematical transformations and expressions should be avoided in the text. The article styling shall be as follows:

– title of the journal section;
– UDK index;
– PACS classification code (https://publishing.aip.org/wp-content/uploads/2019/01/PACS_2010_Alpha.pdf);
– article title;
– initials and surnames of authors;
– abstract of the article (10–15 lines describing the purpose of the paper and its main findings);
– keywords;
– scientific specialty code.

5. The main text of the article shall begin with the "Introduction" section clearly stating the purpose and objectives of the paper along with arguments in favor of its preparation against the background of the existing state of the problem addressed in the article. The further text of the article shall also have meaningful headings (sections and subsections) without being numbered. The article shall end with a separate section, "Conclusion," listing the main findings, conclusions that follow from them, and, if possible, proposals for the research advance and use of its findings.

The bottom of the first page of the text shall accommodate a separate paragraph (in bold) containing contact information about the author (or authors) **(mandatory section)**: surname, first name, patronymic (in full), **e-mail (of all authors),** profiles and registration numbers in scientometric databases (SPIN code, RINTS Author ID, ArXiv Author ID, Orcid ID, Scopus Author ID), academic degree, title, position, postal address of the enterprise).

Also a person responsible for message exchange with the editorial board shall be specified.

Authors can suggest potential reviewers (2–3 people by indicating their full name, place of work, and email address). The proposed candidates shall not work in the institutions where the authors do.

The main text shall be followed by the list of references called “Bibliography”.
Examples of designations of references used in the "Bibliography" section.

Articles shall be referred to as follows: Surname, initials, journal title, year, volume, issue, page numbers.
Ivanov I. I. / Applied Physics. 2022. No. 1. P. 12–18.
Lang D. V. / J. Appl. Phys. 1974. Vol. 45. No. 7. R. 3023–3034.
Reference to **books**: Surname, initials, book title, city, publisher, year. (When a specific chapter or page in a book is referred to, the page number is placed after the year.)
Korn G., Korn E. Mathematical Handbook. – Moscow: Nauka, 1974.
Biberman L. M., Vorobiev V. S., Yakubov I. T. Kinetics of non-equilibrium low-temperature plasma. – Moscow: Nauka, 1982. P. 371.
Ultraviolet technologies in the modern world / edited by Karmazinov F.V. Kostyuchenko S.V., Kudryavtsev N.N. – Dolgoprudny: Intellekt, 2012.

Reference to **conference proceedings:** Surname, initials, title of publication, place and date of publication, page numbers.
Romanov A. V., Stepovich M. A., Filippov M. N. / Proceedings of the XVII International Conference "Radiation Physics of Solids". – Sevastopol, 2007. P. 592–599.

Reference to **patents**: Surname, initials, title, type, number, year.
Davydov S. G., Dolgov A. N., Yakubov R. H. Vacuum spark gap. Patent of invention No. 2654494 (RF). 2018.

Reference to **dissertations and Abstracts**: Surname, initials, title of paper (abstract), diss. … Candidate (Doctor) of Physics and Mathematics, city, organization, year.
Grechikhin V. A. Development and analysis of computer algorithms for processing single-particle signals of laser Doppler anemometers: Abstract from diss. by Candidate of technical sciences. – Moscow: MPEI, 1996.

Further, detailed English-language information about the article required for indexing the entire journal, the given article and its authors in international scientometric databases shall follow, namely: PACS, article title, authors' surname and initials (English transliteration), enterprise, its postal address, author(s) e-mail, abstract, keywords, references; since the journal is also distributed abroad, the editorial board reserve the right to correct the English part of the text without changing its meaning.
Styling of the References in the English part of the article has its own peculiarities. In particular, if the cited book or monograph is a translation into Russian from a foreign publication, the original data of this publication (authors, book title, publisher, city or country, year of publication) shall be given, as well as the Russian publisher and the year of publication in Russian. Given below are the main examples of designation of used references in the References section:
Article from the journal:
Ivanov I. I., Applied Physics, No. 1, 12–18 (2022) [in Russian].
Lang D. V., J. Appl. Phys. **45** (7), 3023–3034 (1974).
Note: if a Russian journal has a printed English analogue, the English title of the analogue shall be used and page numbers shall be taken therefrom. If there is no English analogue, the English transliteration of the Russian name shall be used.

Book:
Korn G. and Korn E., Mathematical Handbook. New York-London, Mcgraw-Hill Book Company, 1968; Moscow, Nauka, 1974.
Ultraviolet technologies in the modern world / ed. Karmazinov F. V., Kostyuchenko S. V., Kudryavtsev N. N. Dolgoprudny, Intellect, 2012 [in Russian].

Conference proceedings:
Romanov A. V., Stepovich M. A., and Filippov M. N. Proc. XVII Intern. Meeting on Radiation Physics of Solid State. Sevastopol, 2007, pp. 592–599.

Patents:
Davydov S. G., Dolgov A. N., Yakubov R. H. Vacuum spark gap. Patent for invention No. 2654494 (RF). 2018.
Dissertations and Abstracts:
Grechikhin V. A. Development and analysis of computer algorithms for processing single-particle signals of laser Doppler anemometers: Abstract. Diss. Candidate of Technical Sciences. M., MEI, 1996.

6. The list of references (“References”) shall correspond to all references to external sources used in the text of the article. These references shall be enclosed in square brackets, for example, [1–3], [7, 8]. Internal references, i.e. references to formulas, figures and tables of the article shall be enclosed in round brackets, for example, formula (3), equation (1), (Fig. 2), (Table 3). Any references in figure captions or in the figures are not recommended.

7. The number of figures and photos for a typical article shall not exceed 4. If one figure contains two, three or more variants of graphic (or photo) images of the type “Fig. 2*a*”, “Fig. 2*b*”, etc., each individual variant is considered as a separate figure. If the above limit number of figures (photos) is exceeded, the article is sent back to the authors for revision. Graphics (black and white and color) shall be put directly in the proper place in the article and in the proper scale. Next to the graph axes, the displayed physical quantities shall be indicated only (**strictly!**) using symbols (letters), and after a comma - the quantity dimension in Russian (in direct font). It is recommended to number different curves on graphs, even if they are identified by a different color or line type. Graphs shall be submitted only (**strictly!**) against the white background. Auxiliary grids are not allowed in the graph area.

8. Captions under the corresponding figures shall be out in the proper places in the text. Each caption shall be as short as possible, but meaningful in terms of its content. Any physical (technical) symbol included in the caption shall have its verbal explanation there.

9. Simple formulas shall be included in the text in the format of the text editor used; more complex formulas shall included using MathType formula editor. Standard mathematical notations (e.g. max, log, sin, exp, etc.) shall be typed directly. The same is true about figures and numbers. Formula numbers shall written in parentheses on the right. To indicate non-vector physical (technical) quantities using symbols, use only the Latin and Greek alphabets, while using a straight font for Greek letters, and an oblique font (italics) for Latin letters in the text. Vectors and matrices shall be marked by a bold, upright font (preferred) or an arrow above the italic vector symbol (less preferred). For subscripts and superscripts, use Arabic numerals, Latin or Greek letters, but if the index, usually a subscript, is a short (abbreviated) form of the Russian characteristic word, it is allowed to use Russian letters in its designation (uppercase font), for example U_{in}, I_{out}, v_{gr}, etc. The dimension of physical quantities shall be always given only in Russian, using an uppercase font.

10. Tables shall be made in accordance with the following requirements: the top line contains the data name and dimensions; the following lines contain the data itself.

11. Formulas, tables and figures shall have their own separate continuous numbering system. If there are no additional (return) references to a specific formula in the text or it is used only once, it shall not be numbered. A table and/or a figure used only once do not require numbering either.

12. Manuscripts and CD/DVD will not be sent back by the editorial board.

13. Authors (or an author) of each article after it is published in a journal issue have a right to receive an electronic version of the article in PDF format (Adobe Acrobat editor) from the editorial board.

14. When published in the journal, each article is accompanied by a footnote with the copyright symbol © placed before the author's name (authors’ names). The article shall also specify the date the article was received by the editorial board.

Applied Physics: Scientific and Technical Journal / RD&P Center ORION, JSC, 2025. No. 5.

Signed to the press on October 20, 2025
A4 format. Offset paper.
Digital printing.
Printed in the printing house of LLC PKK "YOUR FORMAT".
Address: 15, Malaya Kaluzhskaya st., Moscow, 119071.
Tel. (495) 749-45-84